Fall 2003

Fabrication and characterization of microcrystalline silicon solar cells

Liwei Li
New Jersey Institute of Technology

ABSTRACT

FABRICATION AND CHARACTERIZATION OF MICROCRYSTALLINE SILICON SOLAR CELLS

by
Liwei Li

In this study, single junction *p-i-n* μc-Si:H solar cells were prepared using plasma of silane diluted by hydrogen in a low-cost, single chamber, non-load-locked RF-PECVD system. Direct structural characterization of μc-Si:H solar cells, rather than stand-alone films, was conducted using Raman Spectroscopy, XRD, and AFM. Strong correlations among device deposition, *i*-layer structural properties, and device performance have been established. With such correlations, critical issues in fabricating low-cost, large-scale, high performance μc-Si:H solar cells were identified.

The critical importance of seeding processes in determining the microstructure of μc-Si:H *i*-layers and performance of μc-Si:H solar cells has been demonstrated. Using *p*-layer seeding methods, stable conversion efficiencies of 5% have been achieved using very simple device configuration. Micro-crystallinity obtained from Raman scattering, presented as *Ic/Ia*, proved to be sensitive to the microstructure of μc-Si:H *i*-layers. Strong spatial non-uniformity of *i*-layer microstructure as well as variations in device performance were observed. A wide variety of *i*-layer microstructures, from mixed-phase Si:H to highly crystalline μc-Si:H, were revealed by Raman scattering. Generally, solar cells with mixed-phase Si:H *i*-layers exhibit high open circuit voltages, low fill factors, low efficiencies, and severe light-induced degradation. On the other hand, solar cells with truly μc-Si:H *i*-layers show low open circuit voltages, high fill factors, high efficiencies,

and excellent stability against light-induced degradation. It was shown by XRD experiments that high performance, optimum μc-Si:H solar cells exhibit smaller grain sizes compared to solar cells with *i*-layers showing higher micro-crystallinity. Correlations among non-uniformity pattern, *i*-layer micro-crystallinity, and AFM surface morphologies were also observed.

Solar cells with truly μc-Si:H *i*-layers exhibit excellent stability under both conventional and accelerated light soaking. Mixed-phase Si:H solar cells show much worse stability against light exposure. However, it has been demonstrated that stable, high performance μc-Si:H solar cells can only be obtained with *i*-layers being μc-Si:H, yet close to the μc-Si:H to mixed-phase Si:H transition edge where an optimum micro-crystallinity range (*Ic/Ia* at around 1.8) was identified. These optimum μc-Si:H solar cells exhibit moderate open circuit voltages at ~ 0.5 V, high fill factors, high efficiencies, and excellent stability against light-induced degradation. Such optimum μc-Si:H *i*-layers demand a very narrow optimum processing window.

FABRICATION AND CHARACTERIZATION OF MICROCRYSTALLINE SILICON SOLAR CELLS

by
Liwei Li

A Dissertation
Submitted to the Faculty of
New Jersey Institute of Technology
in Partial Fulfillment of the Requirements for the Degree of
Doctor of Philosophy in Materials Science and Engineering

Interdisciplinary Program in Materials Science and Engineering

January 2004

APPROVAL PAGE

FABRICATION AND CHARACTERIZATION OF MICROCRYSTALLINE SILICON SOLAR CELLS

Liwei Li

Dr. Roland A. Levy, Dissertation Advisor — Date
Distinguished Professor of Physics, NJIT

Dr. Nuggehalli M. Ravindra, Committee Member — Date
Professor of Physics, NJIT

Dr. Marek Sosnowski, Committee Member — Date
Professor of Electrical and Computer Engineering, NJIT

Dr. Trevor A. Tyson, Committee Member — Date
Professor of Physics, NJIT

Dr. Yuan-Min Li, Committee Member — Date
Director of Technology, Energy Photovoltaics, Inc., Lawrenceville, NJ

BIOGRAPHICAL SKETCH

Author: Liwei Li

Degree: Doctor of Philosophy

Date: January 2004

Undergraduate and Graduate Education:

- Doctor of Philosophy in Materials Science and Engineering
  New Jersey Institute of Technology, Newark, NJ, 2004

- Master of Science in Materials Science and Engineering
  Xi'an Jiaotong University, Xi'an, P. R. China, 1994

- Bachelor of Science in Materials Science and Engineering
  Xi'an Jiaotong University, Xi'an, P. R. China, 1991

Major: Materials Science and Engineering

Presentations and Publications:

Yuan-Min Li, J. A. Anna Selvan, Liwei Li, Roland A. Levy, and Alan E. Delahoy, "A Study of Single Chamber PECVD μc-Si Solar Cells", Proceedings of the 3rd World Conference on Photovoltaic Energy Conversion, Osaka, Japan, May 2003.

Liwei Li, Yuan-Min Li, J. A. Anna Selvan, Alan E. Delahoy, and Roland A. Levy, "Structural Characterization of Microcrystalline Silicon Solar Cells Fabricated by Conventional RF-PECVD", Materials Research Society Symposium Proceedings Vol. 762, A5.15.1, San Francisco, CA, April 2003.

R. J. Martin-Palma, J. M. Martinez-Duart, L. Li, and R. A. Levy, "Electrical Behavior of Double-Sided Metal/Porous Silicon Structures for Optoelectronic Devices", Materials Science and Engineering **C 19**, 359 (2002).

Liwei Li, Yuan-Min Li, J. A. Anna Selvan, and Roland A. Levy,
"Low Temperature Fabrication of Microcrystalline Silicon (μc-Si:H) Solar Cells Using RF-PECVD",
The 2nd AIMS Materials Research Symposium, Newark, NJ, May 2002.

R. J. Martin-Palma, J. M. Martinez-Duart, L. Li, and R. A. Levy,
"Double-Sided Metal/Porous Silicon Structures for Optoelectronic Devices",
E-MRS Spring Meeting 2001, Strasbourg, France, June 2001.

Liwei Li, Pingsheng Zhang, and Yaorong Feng,
"Failure Analysis of Petroleum Dredge Pump Head",
Proceedings of the 3rd National Conference on Failure Analysis, Prediction, and Prevention for Mechanical and Electrical Equipments, Beijing, China, 1998, p782.

Liwei Li, and Yonghong Zhang,
"Research on the Manufacture of Helical Submerged-Arc Welded Steel Pipes and Its Standard",
Technology Supervision in Petroleum Industry **14**, 8 (1998).

Liwei Li, and Yaorong Feng,
"Properties and Grayness Defects of TS 52K ERW Line Pipes",
Proceedings of 97 National Conference on Materials for Petroleum and Petrochemical Industry, Zhejiang, China, 1997, p141.

Liwei Li, Yonghong Zhang, and Qingren Xiong,
"Features of Factory Quality Supervision and Its Effect on Manufacturing Oil Line Pipes",
Technology Supervision in Petroleum Industry **12**, 22 (1996).

This dissertation is dedicated to my beloved wife, Xin Guan,
for her love, encouragement, and support

ACKNOWLEDGEMENT

I wish to express my deepest appreciation to my dissertation advisor, Dr. Roland A. Levy, who provided me with the opportunity to conduct research under his supervision. I am thankful for his guidance, encouragement and support, and for providing invaluable and countless resources, insight, and intuition during the course of this research.

I am also deeply grateful to Dr. Yuan-Min Li who not only served as a committee member and mentor, but also provided me with valuable guidance and suggestions throughout the work conducted at Energy Photovoltaics, Inc. Sincere gratitude also goes to Dr. Alan E. Delahoy for allowing me using the facilities at Energy Photovoltaics, Inc., without which it would not have been possible for me to complete my dissertation research.

Special thanks are given to Dr. Nuggehalli M. Ravindra, Dr. Marek Sosnowski, and Dr. Trevor A. Tyson for actively participating in my research efforts and serving as committee members.

I would like to extend my thanks to my fellow graduate students, Dianhong (Diane) Luo and Yong Seok Suh, of the Chemical Vapor Deposition Laboratory at NJIT for their encouragement and friendship throughout these years. Special thanks are also due towards the scientific and engineering staff at Energy Photovoltaics, Inc. for their kindly assistance, valuable suggestions, and sincere friendship.

This work was supported in part by the U.S. Department of Energy under contract No. DE-FG02-00ER45806.

TABLE OF CONTENTS

TABLE OF CONTENTS
(Continued)

TABLE OF CONTENTS
(Continued)

Chapter **Page**

LIST OF TABLES

LIST OF FIGURES

LIST OF FIGURES
(Continued)

LIST OF FIGURES
(Continued)

LIST OF FIGURES
(Continued)

CHARPTER 1

INTRODUCTION

1.1 Importance of This Research

As concerns about energy shortage and long-term global warming effect associated with the burning of fossil fuels keep growing, a quest for viable alternate energy sources is becoming imperative. Nuclear power plants, in turn, have no large environmental impacts in principle. However, expanded use of nuclear energy is unlikely due to a fear of radioactive waste and accidents. It is therefore clear that a transition to new sustainable energy sources is required.

The use of solar energy turns out to be one of the promising solutions, which is of high importance for both energy security and environment benignity. Solar radiation originates from the nuclear fusion in the sun which converts the net mass loss of the sun to energy through the Einstein relation $E = mc^2$ at a rate of 4×10^{26} J/s. The solar energy delivered over the whole earth's surface gives 10000 times the amount of the primary energy currently needed worldwide (i.e., one hour of sunlight $\approx$ total annual energy consumption of the entire world). It is, therefore, evident that efficiently converting even a small part of the solar energy to a useful energy form would largely solve the energy demands.

To be a substantial contributor to the general production of electricity, a massive increase in photovoltaic (PV) module production volume is needed. It will take, even at the present impressive growth rate of approximately 40%/year, approximately 2–3

decades more for PV technology to have a noticeable effect in the substitution of fossil fuels or in the replacement of nuclear power stations on a global level [1]. It is, therefore, necessary to choose a PV technology that can cater to such a massive production volume. On the other hand, cost reduction has been being the driving force in developing PV technologies for massive terrestrial applications. Wafer-based crystalline silicon PV technology, the workhorse of current PV market, has contributed to a substantial decrease in PV module prices in the past two decades, its further price reduction potential can be considered to be relatively modest. Therefore, thin film PV technologies are attracting growing interest due to their potentials of cost reduction and large-scale production. Among the thin film PV technologies, cadmium telluride (CdTe) and copper indium (gallium) diselenide (CIGS) constitute two options that have given rise to considerable interest and conversion efficiencies of 15–20% have been reached with laboratory scale solar cells [2]. However, mass production of such modules is only gradually taking off due to both technology reasons and long-term material availability [3]. One alternative way is the so-called thin film silicon solar cell, which improves on the drawbacks of crystalline silicon PV technology, e.g., high cost and limitation on large-scale manufacturing, as well as keeps its advantages such as well-established technology, abundant material supply, etc.

The first hydrogenated amorphous silicon (α-Si:H) thin film solar cell was reported in 1976 [4]. Contrary to the high expectations once given to this relatively new technology, however, the current PV market is still dominated by crystalline (single- and poly-crystalline) silicon with over 80% share of the total PV market. Thin film PV devices, mainly amorphous silicon based PV devices, contribute about 8% of the total PV

market. A vexing problem, light induced degradation, results in the relatively low efficiencies of the commercial single-junction α-Si:H solar cells and explains why α-Si:H solar cells have not attained the dominance once thought likely [3, 5].

Though extensive studies have been conducted since the Staebler-Wronski Effect (SWE) was first reported in 1977 [6], only limited success has been made over two decades in understanding of the nature of the light-induced metastable defects or the mechanism for their creation. During the course of attempts to improve the quality of α-Si:H, especially its resistance to light-induced degradation, μc-Si:H is emerging as a contender for PV applications. Deposition of μc-Si:H, typically using plasma enhanced chemical vapor deposition (PECVD), is almost fully compatible with the well-established low-temperature, low-cost α-Si:H deposition process. The much higher stability of μc-Si:H against light exposure, both as single junction cells as well as the narrower-bandgap component of α-Si:H/μc-Si:H tandem devices, has been demonstrated with laboratory scale solar cells. In addition, μc-Si:H based solar cells are also of significance due to more effective utilization of solar spectrum as well as cost reduction resulting from the replacement of α-SiGe:H by μc-Si:H. Over the past few years, a worldwide interest in μc-Si:H based PV technology has been sparked and considerable progress has been made.

1.2 Technology Challenges and Objectives of the Research

With respect to solar cell structure design, the biggest challenge in μc-Si:H PV technology comes from the low optical absorption of μc-Si:H. It is well known that one of the most important advantages of α-Si:H is that it no longer behaves like an indirect

bandgap semiconductor and has a very high optical absorption even though its bandgap increases to ~1.7 eV [7]. Thus, absorber layers in single junction α-Si:H solar cells can be as thin as ~5000 Å, leading to a strong internal electric field over the intrinsic layer that enhances the carrier collection. In view of the fact of the very low optical absorption of μc-Si:H, μc-Si:H absorber layers must be much thicker than their amorphous counterparts. Therefore, effective light trapping becomes a critical issue in designing μc-Si:H solar cells. Furthermore, when μc-Si:H *i*-layers are included in α-Si:H/μc-Si:H tandem structures, light trapping of the top amorphous cell is weakened and current match between the top and bottom cells may become the limiting factor of device performance [1].

Deposition of μc-Si:H also presents some challenges. Pioneering work in producing μc-Si:H solar cells was done initially by very high frequency (VHF) PECVD and some other novel approaches were also studied later on. However, conventional RF-PECVD with excitation at 13.56 MHz is still the most studied, preferred method due to its simplicity and compatibility with the well-established α-Si:H PV technology. For RF-PECVD deposition of μc-Si:H, first of all, thicker layer results in long deposition time (growth rate is significantly decreased due to high H_2 to SiH_4 dilution ratio), leading to higher energy consumption. Secondly, uniformity and reproducibility are questionable and large-scale deposition is an even more critical long-term, industrial-related issue. Changing of plasma conditions to those favoring formation of μc-Si:H, e.g., high plasma power, may damage the interface within solar cells and decrease the quality of μc-Si:H films, thus, leading to inferior device performance.

Though extensive efforts have been carried out and considerable progress has been made on μc-Si:H based materials and solar cells, most studies so far have been conducted in laboratory scale systems featuring small substrate area, ultra-high vacuum, and low contamination environment (sophisticated, multi-chamber, load-locked deposition systems). Most of the exciting results are obtained from solar cells with very small area and optimized light trapping schemes, including expensive, laboratory substrates (e.g., Asahi type 'U' SnO_2 or custom ZnO-coated glass of high texture and low absorption) and highly effective back reflector (e.g., ZnO/Ag). Cost reduction and other industrial-related issues are not the major concerns in such research. The major goal of this research, therefore, is to develop a μc-Si:H intrinsic layer deposition technology using RF-PECVD in a low-cost, high throughput basis to evaluate the potential of utilizing μc-Si:H intrinsic layers in cost-competitive manufacturing of large-scale PV devices.

Scientific insights are always needed to better understand the deposition process and its effects on device performance. Characterization of optical, structural, and electrical properties of α-Si:H, which can be grown readily on a large variation of substrates in a relatively broad deposition regime, is generally carried out with standalone films deposited on special substrates, e.g., Corning 7059 glass. Unlike α-Si:H, growth of μc-Si:H, especially the initial nucleation step, is highly dependent on reactor geometry, processing parameters, substrates, and underlying layers. Properties obtained from stand-alone films may not be necessarily translated into μc-Si:H *i*-layers incorporated within actual solar cells. Thus, direct characterization of μc-Si:H solar cells (rather than stand-alone films), which are relatively lacking, is one of the major concerns in this research.

1.3 Tasks of the Research and Outline of the Dissertation

As a joint program between New Jersey Institute of Technology (NJIT) and Energy Photovoltaics, Inc. (EPV), this study can be basically divided into two parts: 1) device fabrication and test which are performed at EPV; and 2) structural characterization of μc-Si:H solar cells which is conducted at NJIT. The tasks involved to achieve the aforementioned goals include:

1. Construction of a compact, single chamber, non-load-locked PECVD system with conventional RF power excitation at 13.56 MHz at EPV. This low-cost, batch-process type system, which is capable of simultaneously coating 4 plates equal in size of 15" × 12", has the advantages of large substrate area, easy operation, low maintenance, and high throughput.

2. Fabrication of μc-Si:H solar cells using the newly constructed RF-PECVD system. Installation and debugging of the RF-PECVD system, as well as the fabrication of μc-Si:H solar cells using this system and other necessary facilities, are primarily carried out by EPV personnel (Dr. Yuan-Min Li *et al*). Single junction *p-i-n* type solar cells with μc-Si:H *i*-layers, without any back reflectors or other light trapping enhancement schemes, are deposited on commercial grade SnO_2/Soda-lime glass superstrates using plasma of SiH_4 diluted in H_2. Stable conversion efficiencies of about 5% for solar cells with such simple configuration have been achieved in this study.

3. Performance test of μc-Si:H solar cells. The routine performance test includes device shunting test, I-V characteristics, and quantum efficiency (spectral response). Both conventional light soaking and accelerated light soaking are conducted on selected devices to verify the stability of μc-Si:H solar cells against light-induced degradation.

4. Structural characterization of μc-Si:H solar cells. This task is primarily carried out at NJIT using actual solar cells, rather than stand-alone films deposited on special substrates. The structural characterization techniques used include Raman Spectroscopy, X-Ray Diffraction (XRD), and Atomic Force Microscopy (AFM). Correlations among μc-Si:H *i*-layer deposition processes, structural properties, and PV device performance have been established and such relationships have become handy feedback tools in optimizing μc-Si:H solar cell deposition processes

The major work conducted by the author throughout this study includes:

- Involvement in the final stage of the construction and debugging of the RF-PECVD system.

- Participation in the fabrication of μc-Si:H solar cells.

- Routine device performance test in the early stage of the project.

- Various device performance tests on selected μc-Si:H solar cells.

- Structural characterization of μc-Si:H solar cells using Raman Spectroscopy, XRD, and AFM.

Throughout this study, it is recognized that seeding processes play crucial roles in determining the microstructure of μc-Si:H *i*-layers and the performance of resulting solar cells. Extensive efforts are taken to identify the critical issues in fabricating μc-Si:H solar cells in the low-cost, relatively large-scale RF-PECVD system, including the effect of seeding processes, optimum processing conditions for high performance μc-Si:H solar cells, as well as spatial non-uniformity of *i*-layer microstructure and device performance. It is also revealed that microstructures and properties of μc-Si:H *i*-layers are strongly

dependent on the deposition sequences and plasma conditions used in this study. Therefore, direct structural characterization of real μc-Si:H solar cells, which is probably the best approach capable of evaluating the structural properties of μc-Si:H *i*-layers deposited within *p-i-n* device configuration, is performed and major efforts of this study was focused on establishing correlations among μc-Si:H *i*-layer deposition processes, performance of μc-Si:H solar cells, and *i*-layer structural properties.

The dissertation is organized in the following manner:

Chapter 1: Introduction.

Chapter 2: Review of related literature which includes fundamentals of solar cells, development and current status of Si:H based thin film PV technology, and topics related to the structural evolution during deposition of μc-Si:H.

Chapter 3: Experimental methodology including the single chamber RF-PECVD system used in this study, design of μc-Si:H solar cells, device fabrication procedures, device performance test, and structural characterization methods.

Chapter 4: Experimental results and discussion which present the results obtained so far and focus on establishing correlations among μc-Si:H *i*-layer deposition processes, performance of μc-Si:H solar cells, and *i*-layer structural properties through device performance test and structural characterization of actual devices.

Chapter 5: Conclusions.

CHARPTER 2

REVIEW OF RELATED LITERATURE

2.1 Fundamentals of Photovoltaics

The discovery of the basic effects behind the operation of solar cells has taken a span of about 200 years, starting with the discovery of Selenium in 1817 by Berzelius and photovoltaic effect observed by Becquerel in 1839 [8]. Along with the progressing development of silicon processing technologies such as Czochralski method and the technique of solid diffusion in producing *p-n* junctions in silicon, a *p-n* junction solar cell with conversion efficiency of about 6% was first reported in 1954 at Bell Laboratories [9]. Since then, progress has been made steadily in all aspects of solar cell fabrication, design of device structure, and understanding of device operation.

2.1.1 Photovoltaic Effect

The photovoltaic effect is the basis of the conversion of light to electricity in solar cells. It can be simply defined as the generation of a potential (photovoltage) when radiation ionizes the region in or near the built-in potential barrier of a semiconductor. This self-generated potential can be used to deliver power to a load through a circuit. The formation of the built-in potential barrier can be explained by considering a junction of *n* and *p*-type semiconductor materials, as shown in Figure 2.1.

Before they are joined, the *n*-type semiconductor material has a large concentration of electrons and few holes, whereas the converse is true in the *p*-type material. Upon joining the two regions, diffusion of carriers takes place because of the large carrier concentration gradients at the junction. The holes diffuse from the *p* side to

the n side, the electrons diffuse from n to p, and they recombine with each other. However, the resulting diffusion current cannot build up indefinitely because an opposing electric field is created at the junction. If we consider that electrons diffusing from n to p leave behind uncompensated positive (donor) ions in the n region, and the holes leaving the p region leave behind uncompensated negative (acceptor) ions, it is easy to visualize the development of a region of positive space charge near the n side of the junction and negative charge near the p side. The resulting electric field is in the direction opposite to that of diffusion current. Therefore, this electric field creates a drift component of current from n to p, opposing the diffusion current. Since there is no net current flow across the junction at equilibrium, the drift current must exactly cancel the diffusion current. Therefore, the electric field builds up to the point where the net current is zero at equilibrium [10].

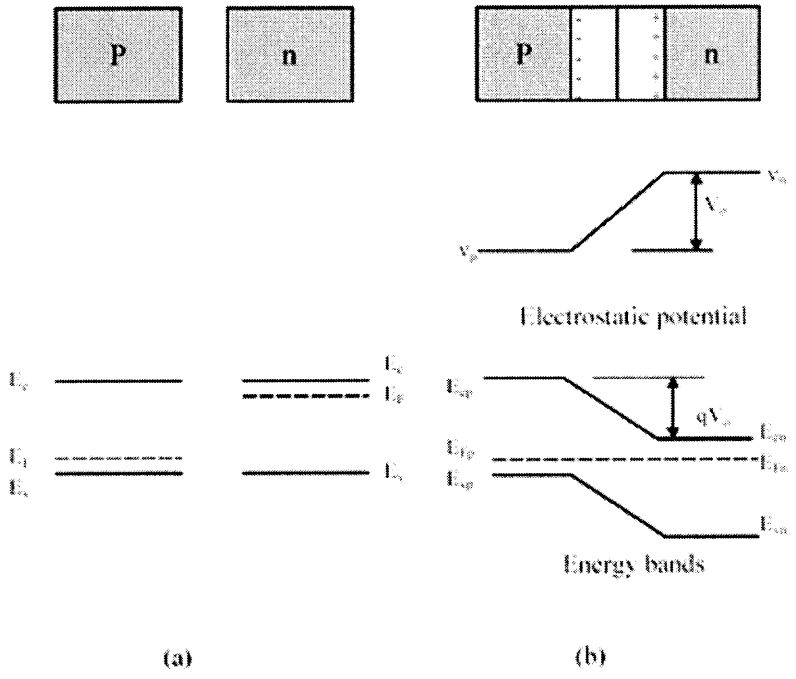

Figure 2.1 (a) Isolated, neutral regions of p- and n-type materials and their energy bands; (b) p-n junction, its energy bands and the built-in potential barrier.

As indicated in Figure 2.1, the electric field appears in the transition region between the *p* and *n* side of the junction, and there is an equilibrium potential difference V_0 across this region. To make the Fermi level constant throughout the device, the valence and conduction bands on *p* side are higher than that on the *n* side by the amount of qV_0. The transition region is also called depletion region, since it is almost depleted of carries compared with the rest of the crystal. The potential difference is a built-in potential barrier that is necessary to the maintenance of equilibrium at the junction.

When the light strikes the *p-n* junction, photons with energy higher than the energy bandgap (1.1 eV for silicon) can create electron-hole pairs throughout the device. Those electron-hole pairs generated within the depletion region are separated by the built-in electric field, electrons being collected in the *n* region and holes in *p* region. Also minority carriers generated thermally within a diffusion length of each side of the junction diffuse to the depletion region and are swept to the other side by the electric field. Those electron-hole pairs generated in *p* side or *n* side contribute little to the generated current because the minority carriers recombine with the majority carriers before they diffuse to the depletion region and the majority part are repelled by the built-in potential barrier. When suitable electrical connections are made, such a device converts light into electricity. The current generated is proportional to the number of photons absorbed, and the voltage depends on the height of the barrier, which is always less than the width of the energy bandgap in the semiconductor and depends on how heavily the *p* and *n* regions are doped.

2.1.2 Basic Operation of Solar Cells

Most of the *p-n* junction mono-crystalline and multi-crystalline silicon solar cells currently fabricated have a screen-printed structure shown schematically in Figure 2.2. The associated processing sequence was developed during the early 1970s and emerged as the commercial standard by the early 1980s [3].

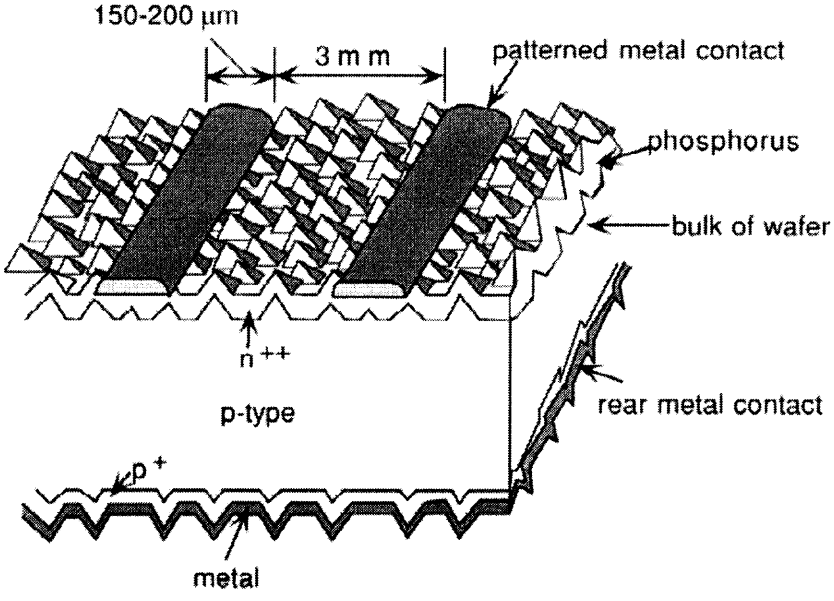

Figure 2.2 Typical screen-printed *p-n* junction solar cell [3].

The basic operation of solar cells can be modeled by considering the ideal equivalent circuit as shown in Figure 2.3 [11]. The simplified circuit consists of a constant current generator (light generated current), a nonlinear junction impedance (diode), and a load. The shunting capacitance and resistance as well as the series resistance are neglected. Light causes a current, J, to flow in the load, the magnitude of this current is the difference between the generated short circuit current, J_L, and the current flowing in the nonlinear junction, J_1.

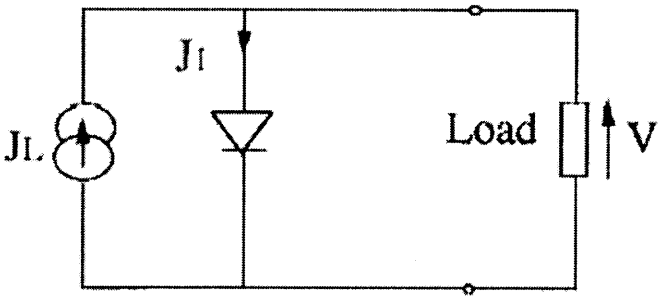

Figure 2.3 Simplified equivalent circuit of a *p-n* junction solar cell.

The current-voltage (I-V) characteristics are described by:

$$\begin{aligned} J &= J_L - J_1 \\ &= J_L - J_{01}\left[exp\left(\frac{qV}{kT}\right) - 1\right] \end{aligned} \tag{2.1}$$

where J_{01} is the dark or reverse saturation current.

When the circuit is short circuited (V = 0), the terms from the diode equation cancel in the above equation. There is a short circuit current equal to J_L. When there is an open circuit across the device, J = 0 and the voltage V = Voc is:

$$Voc = \frac{kT}{q} ln\left(\frac{J_L}{J_{01}} + 1\right) \tag{2.2}$$

When $J_L >> J_{01}$,

$$Voc = \frac{kT}{q} ln\left(\frac{J_L}{J_{01}}\right) \tag{2.3}$$

This model can be modified by considering two diodes in the circuit or further improved by considering a series resistance and a shunt conductance [11].

The typical I-V characteristics of solar cells are shown in Figure 2.4. The open circuit voltage Voc and short circuit current density Jsc are determined for a given light level by the cell properties. If there is no external circuit connected to the cell, the voltage

thus measured is referred to as open circuit voltage, Voc. The short circuit current density, Jsc, is defined as the current density flowing through the circuit when the external load is zero. When the cell is connected to a non-zero external load, the power delivered by the cell depends on the I-V characteristics. The maximum power delivered to a load occurs when the product JV is in a maximum. Calling these values of voltage and current Vm and Jm, we can see that the maximum delivered power illustrated by the shaded rectangle in Figure 2.4 is less than the JscVoc product. The ratio JmVm/JscVoc is called the fill factor, and is a figure of merit for solar cell design.

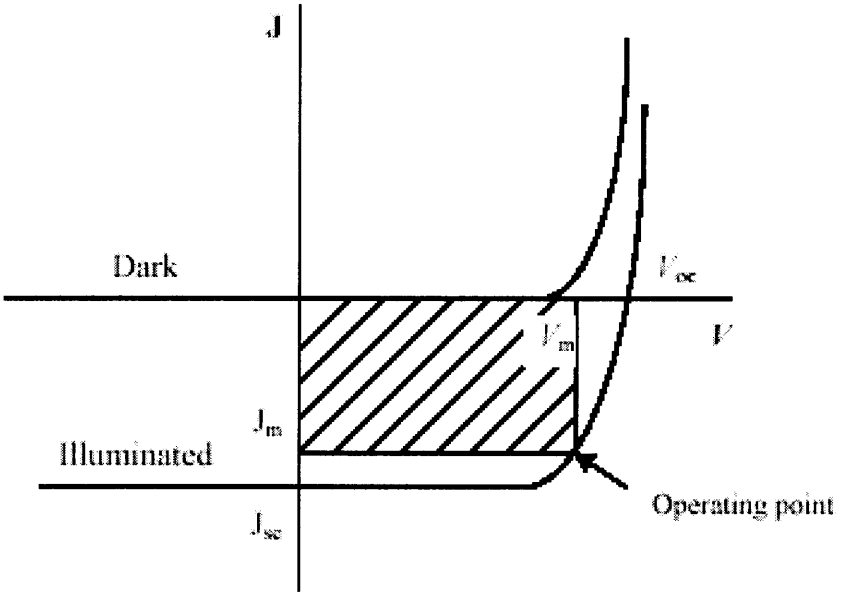

Figure 2.4 Current-voltage characteristics - illuminated and not illuminated.

In the ideal case, the conversion efficiency η is defined as a ratio of the maximum output power P_M to the power of the incident light P_L:

$$\eta = \frac{P_M}{P_L} \tag{2.4}$$

The maximum output power is:

$$P_M = Jsc \times Voc \times FF \tag{2.5}$$

where FF is the fill factor. Then η can be rewritten as:

$$\eta = \frac{J_{sc} V_{oc} FF}{\int_0^\infty p(\lambda) d\lambda} \tag{2.6}$$

where P(λ) is the solar power density at wavelength λ.

In the above, we considered an idealized solar cell. However, different loss factors must be taken into account in practice. Some of them have fundamental limits and are unavoidable which include loss by long wavelength photons of the solar spectrum, loss by excess energy of the photons, and lowering of voltage factor and fill factor, etc. The others come from technological limitations and can sometimes be avoided. The most common technological loss factors include loss by reflection, loss by metal coverage, and loss by incomplete absorption due to the limited cell thickness, etc. [11].

2.2 Hydrogenated Amorphous Silicon

2.2.1 Development of Hydrogenated Silicon

Hydrogenated amorphous silicon (α-Si:H) differs from crystalline silicon by the lack of long-range order (disorder) and the high content of bonded hydrogen, typically around 10 at.% in device quality α-Si:H. Before Sterling and Swann first deposited α-Si onto various substrates by RF glow discharge of pure SiH_4 in 1965 [12], it was prepared mainly by evaporation and sputtering, which required high vacuum facilities for making purified materials. As we know now, α-Si made by those methods contains too many localized states in the bandgap to be used in electronic devices. The history of the

development of α-Si:H is full of misinterpretation of experimental data, in particular the crucial role played by hydrogen in the amorphous network [13]. In 1975, Spear *et al* published their data that clearly demonstrated the structural sensitivity caused by substantial doping in α-Si film prepared by RF glow discharge as that in the crystalline silicon [14]. Following Spear's successful doping experiment, Brodsky *et al* showed the importance of hydrogen in α-Si prepared by glow discharge which confirmed the assumption that the key to the doping of α-Si is incorporation of hydrogen within the Si network so as to terminate the dangling bonds that seem to be inherent to materials made by other methods [15]. Thus, the material is designated as hydrogenated amorphous silicon (α-Si:H). Passivation of the dangling bonds by hydrogen reduces their electrically active density from approximately 10^{19} cm^{-3} present in unhydrogenated α-Si to as low as 10^{15} cm^{-3} in α-Si:H. With the disorder and incorporation of hydrogen, α-Si:H no longer behaves like an indirect bandgap semiconductors as does crystalline silicon so that even though its bandgap increases to ~1.7 eV it has a very high optical absorption typically over almost the whole visible sunlight spectrum [7].

From the application point of view, the effect that α-Si:H can be effectively doped is very important. This immediately led to the studies and accomplishments of applications such as thin film solar cells, thin film transistors, color sensors, image sensors, etc. For α-Si:H based PV devices, materials research has been focusing on both improving qualities of α-Si:H, especially its stability against light exposure, and developing deposition techniques capable of producing high quality α-Si:H materials at high growth rate.

2.2.2 Deposition of α-Si:H

Among the various methods of preparing α-Si:H, the most studied one is the glow discharge (PECVD) method, followed by reactive sputtering, thermal CVD, and photo CVD. Typical PECVD reactor design is usually one of two types, namely the capacitively coupled (diode) type and the inductively coupled (electrodeless) type. While radio frequency (RF) plasma of 13.56 MHz is normally used, direct current (DC) glow discharge can also be used for the former configuration [16].

Now, the capacitively coupled RF-PECVD has become the standard approach for manufacturing large-scale α-Si:H PV devices. The non-equilibrium plasma of PECVD, where the electron temperature (in the order of eV) is much higher than the gas temperature (~ room temperature), facilitates the synthesis of materials on low temperature substrates without thermal damage. Device quality α-Si:H is typically deposited at around 200 °C and such a low temperature process allows for a variety of low-cost materials as substrates. α-Si:H can be easily doped by adding phosphorus (P) or boron (B) containing gases during the deposition process (without requiring any P or B diffusion at higher temperature).

Figure 2.5 shows schematically the basic configuration of an RF-PECCD reactor and the electric filed distribution across the plasma between the two electrodes [16]. The potential in the plasma positive column region, known as the plasma potential (V_p), is always positive with respect to the ground potential. It should be noted that the substrate installed on the grounded electrode is negative with respect to the plasma, and is therefore constantly exposed to bombardment by the positive ions.

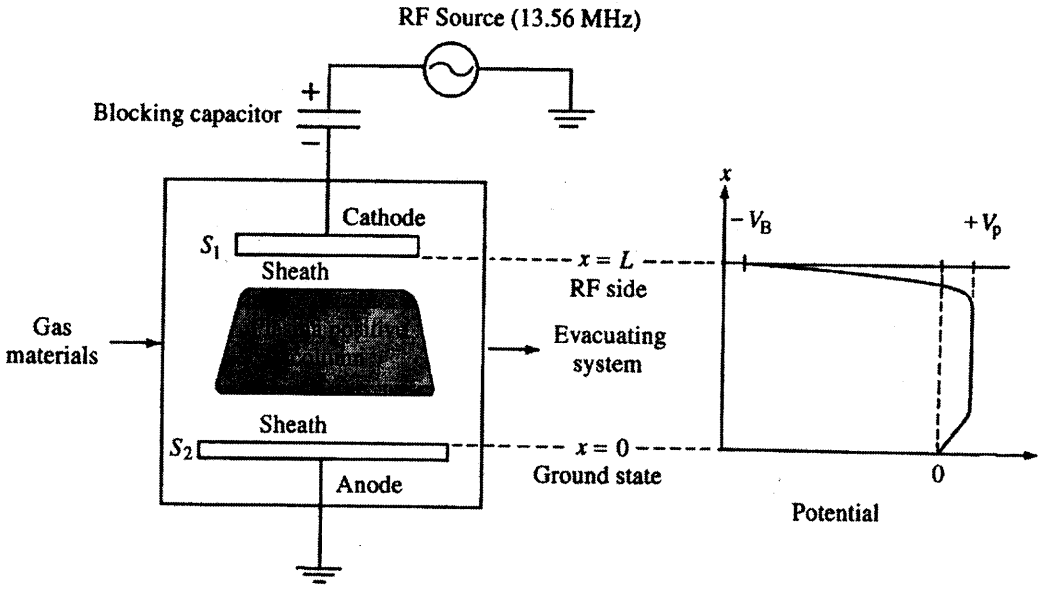

Figure 2.5 Schematic configuration of RF-PECVD reactor and the potential distribution in steady-state plasma operation [16].

The potential in the powered electrode is also negative with respect to the plasma. The large difference in mobility between electrons and ions in a glow discharge results in the static I–V characteristic of the plasma being similar to a leaky diode, as shown in Figure 2.6. An RF voltage applied to this type of load induces a large electron current toward the powered electrode during one-half of the cycle and a small ion current on the other half of the cycle. As a result, the capacitor connected to the RF power source is negatively charged to develop the average self-bias potential V_B (for this reason this electrode is called the cathode) [17]. This takes place in the light non-emitting area known as the plasma sheath.

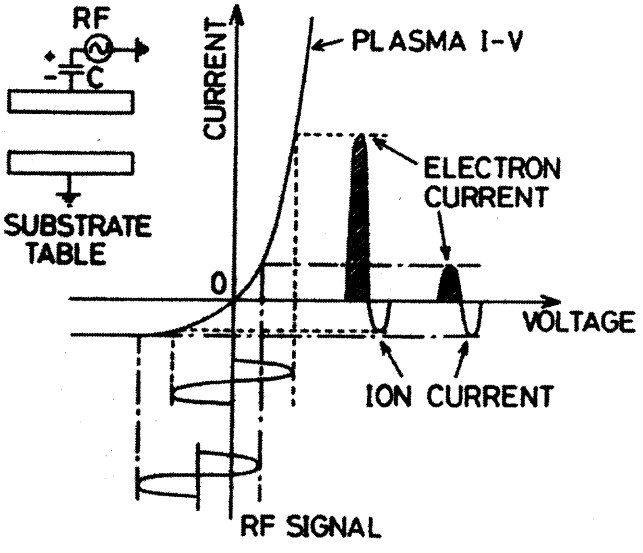

Figure 2.6 Development of a negative self-bias on the powered electrode [17].

The frequency at which the ions do not effectively respond to the changing field, namely the cut-off or critical frequency f_c, is given by the following equation:

$$f_c = \frac{eE\lambda i}{2\pi m_i v_i L} \tag{2.7}$$

where m_i is the mass of the ion, v_i is the ion velocity, λ_i is the mean free path, e is the charge of the electron, L is the distance between the anode and the cathode, and E is the amplitude of the RF field.

The magnitude of V_B varies depending on the ratio of the areas of the top and bottom electrodes, the ion mass, and the gas pressure. The ratio of the voltage drop at the plasma sheath for the two electrodes is a function of the effective electrode area ratio and given as:

$$\frac{V_p}{V_p + V_B} = \left(\frac{S_1}{S_2}\right)^{\alpha} \tag{2.8}$$

where α is ~4 (theoretically) or ~1 (experimentally). If the relative electrode area is reduced, then the voltage drop at the electrode rises steeply. Within the plasma positive column, electrons accelerated by the voltage V_p collide with molecules to either dissociate or ionize them. In the vicinity of the cathode where the self-biased high voltage (V_B) is effective as illustrated in Figure 2.5, electrons of high energy accumulate. For this reason, the most intensive light emission occurs around the cathode in the positive column, and the rate of molecular dissociation, and hence, the rate of SiH_4 consumption, is at a maximum [16].

2.2.3 Characterization of α-Si:H

Experimental results demonstrated that α-Si:H film contains from a few to about 20 at.% of hydrogen in two different phases depending on the method of preparation. Most of the hydrogen forms Si-H bonds and less than 1 at.% exists as free hydrogen molecules. Incorporation of hydrogen into α-Si relaxes the constrained structure and thus changes the optical and electrical properties of the films. Its importance can never be overestimated and various techniques were developed to measure it. Representative methods include infrared absorption, secondary-ion mass spectrometry (SIMS), nuclear-reaction method, hydrogen thermal evolution, proton-electron nuclear double resonance spectroscopy (^{1}H-ENDOR) and proton nuclear magnetic resonance spectroscopy (^{1}H-NMR).

Among those, infrared spectroscopy is perhaps the most widely used since it is nondestructive and easily performed, and yields information about hydrogen content as well as the bonding configurations. The infrared absorption studies of Si-H bonds in late 1970s identified the stretching modes in the 2000-2100 cm^{-1} region, the bending modes in

the 800-900 cm^{-1} region, and the rocking and wagging modes at 630 cm^{-1} [17-19]. Such studies demonstrated that α-Si:H films grown at lower temperature (i.e., room temperature) contain not only monohydride (Si-H), but also dihydride species such as $Si{=}H_2$, $(Si{=}H_2)_n$, and $Si{\equiv}H_3$. In films grown at higher temperature, Si-H type bond is predominant [20].

The hydrogen content in α-Si:H can be obtained by determining the bonded-hydrogen content C_H from the areas of various bands in the infrared absorption spectrum. The most widely used approach was given by Brodsky *et al.* [18],

$$C_H = AI \tag{2.9}$$

where,

$$I = \int(\alpha/\omega)d\omega \tag{2.10}$$

where α is the absorption coefficient, ω is the frequency in cm^{-1}, and the integral is over the absorption band of interest. The constant of proportionality (A) is empirically determined. For the wagging mode at around 630 cm^{-1}, most studies support $A = 1.6\times10^{19}$ cm^{-2}. For the absorption band around 2000-2100 cm^{-1} and 800-900 cm^{-1}, 1.4×10^{20} cm^{-2} and 2.0×10^{19} cm^{-2} were widely accepted [16]. It has been argued that Brodsky's approach leads to considerable overestimation of the absorption data for films thinner than 1 μm. If the film is thinner than 1 μm, Brodsky's approach should be corrected by additional correction factors to compensate the overestimation of the IR absorption [21].

In 1992, Langford *et al.* argued that A_{2000} and A_{2100} should be determined separately and made the correction to $A_{640} = (2.1 \pm 0.2) \times 10^{19}$ cm^{-2}, $A_{2000} = (9.0 \pm 1.0) \times 10^{19}$ cm^{-2}, $A_{2000} = (2.2 \pm 0.2) \times 10^{20}$ cm^{-2}, respectively [22].

If the frequency is expressed in terms of photon energy (eV), the concentration of hydrogen was given by:

$$C_H = A \int a(hv) dhv \tag{2.11}$$

For the absorption band around 2000-2100 cm^{-1}, A= 1.06 [19].

Proton nuclear magnetic resonance spectroscopy (^{1}H-NMR) provides some useful information with regards to the spatial distribution of hydrogen. Typical ^{1}H-NMR spectrum can be split into two components which are attributed to concentrated hydrogen in the form $(SiH_2)_n$ chains or SiH_x (x=1,2,3) and distributed hydrogen of the SiH type, respectively. The hydrogen distribution, in terms of concentrated hydrogen and distributed hydrogen, can be determined by this method. Analysis of hydrogen evolution upon heating in vacuum also provides information about Si-H bonds and hydrogen distribution in α-Si:H films [16].

Unlike in crystalline solids, where a defect is defined as the displacement of an atom from its proper position in a perfectly regular lattice, the structural defect in α-Si:H is defined as an anomaly in the covalent bond with relation to the short-range order in amorphous silicon network. Any bonding different from the stable coordination number of 4, as determined according to the (8-N) rule of Mott, is defined as a defect. The concentration of the most common defect in α-Si, i.e., dangling bond (the under-coordinated Si atom of coordination number 3), can be determined by electron spin resonance (ESR) with great sensitivity. The concentration of dangling bonds, Ns, ranges from 10^{18} cm^{-3} to 10^{20} cm^{-3} for α-Si. With the introduction of hydrogen in α-Si:H, it is reduced to the range from 10^{15} cm^{-3} to 10^{17} cm^{-3} [16].

Owing to the short-range structural disorder in α-Si, the sharp band edge is tailed into the energy gap and the levels present in the bandgap are called localized states. When the electrons or holes conduct through the solid, their mobility is great in the conduction band or valence band. However, their mobility whitin the localized states decreases sharply due to the hopping conduction between the localized states. If the mobility is expressed as a function of energy, mobility edges exist and a mobility gap can be roughly defined as shown in Figure 2.7. In α-Si without hydrogen incorporation, the defect levels are too numerous to determine the structure of energy bands. With introduction of hydrogen (bonded hydrogen), the defects are blocked efficiently, thus the localized state density decreases sharply and *p-n* control becomes possible. The hydrogen not only fills localized states, but also relaxes local structure. Furthermore, when hydrogen is bonded to Si, the band gap increases since Si-H bond energy (3.4 eV) is higher than that of Si-Si bond energy (2.2 eV) [23].

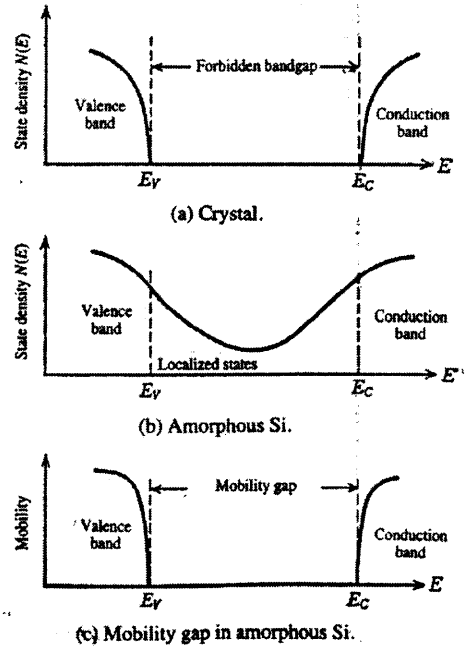

Figure 2.7 Schematic bandgaps of crystalline Si and amorphous Si [23].

The dark conductivity of α-Si:H is usually determined using a single layer deposited on highly resistive substrate (e.g., Corning 7059 or Corning 1737F). Coplanar configuration is most widely used in which two coplanar strips of a metal with low work function are evaporated or pasted less than 1 mm apart on top of the layer, each providing an ohmic contact. The layer under study should be thick enough (i.e., 1 μm) to prevent depletion extending in a region larger than the contact region. A metal box should be used to provide a grounded shield and to prevent all traces of stray light. For device quality α-Si:H, the dark conductivity (σ_d) should be no more than $1 \times 10^{-10}\ \Omega^{-1}cm^{-1}$.

The photoconductivity is determined with the same configuration as used for σ_d except for the film is illuminated with light that has AM1.5 spectrum at an intensity of 100 mW/cm^2. At this wide spectrum illumination the film should be not much thicker than 1 μm. Generally, the requirement of photoconductivity (σ_{ph}) for device quality α-Si:H is no less than $1 \times 10^{-5}\ \Omega^{-1}cm^{-1}$.

The photoresponse σ_{ph}/σ_d reflects to a large extent the opto-electronic quality, but itself is relatively independent of the position of the Fermi level. A low σ_d (e.g., $< 1 \times 10^{-10}\ \Omega^{-1}cm^{-1}$) does not guarantee the absence of electronically active impurities as it could be just as well as due to a relatively large band gap. The activation energy (E_A) of the dark conductivity is a good measure of the energy difference between the Fermi level and the conduction band for electron transport (the valance band for hole transport). It is determined from the temperature dependent conductivity ($\sigma(T)$) by fitting to the relation:

$$\sigma(T) = \sigma_0 \exp(-E_A/kT) \tag{2.12}$$

where, σ_0 is the conductivity prefactor, T is the absolute temperature, and k is the Boltzman's constant. This linear relationship between $log(\sigma(T))$ and $1/T$ is an approximation since the mobility, and thus the prefactor is weakly temperature dependent. It has been estimated that E_A could be determined in the range 50 °C $<T<$ 160 °C with an accuracy of about 100 meV. Combined with the optical band gap, the value of E_A is a very accurate indicator for the presence or absence of impurities [20].

The absorption spectrum of α-Si:H is usually determined from transmission and reflection spectra of thin films considering multiple interference effects. Figure 2.8 shows a typical absorption spectrum of non-doped α-Si:H, obtained by combination of the light transmission spectrum with the photocurrent measurement method. Region A in Figure 2.8 is generally called the "Tauc region" where the spectrum form can be approximated by equation (2.13) and is attributed to the optical electron transition between the extended valence band and the conduction band:

$$\alpha(E)E \propto (E-E_0)^2 \tag{2.13}$$

where, E is the photon energy, $\alpha(E)$ is the absorption coefficient at photon energy E, E_0 is termed the optical energy (or Tauc) gap and is normally used for defining the energy gap of α-Si:H [16]. There is very good linearity in region A if the graph is replotted as $(\alpha(E)E)^{1/2}$ against E. Thus the optical gap can be obtained by extrapolating the linear part as shown in Figure 2.9 [23].

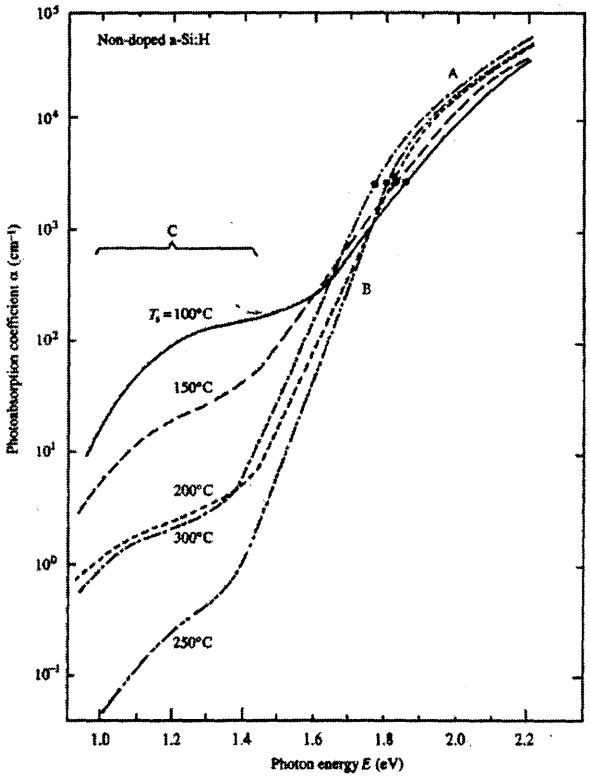

Figure 2.8 Light absorption spectra of non-doped α-Si:H prepared at different substrate temperatures [16].

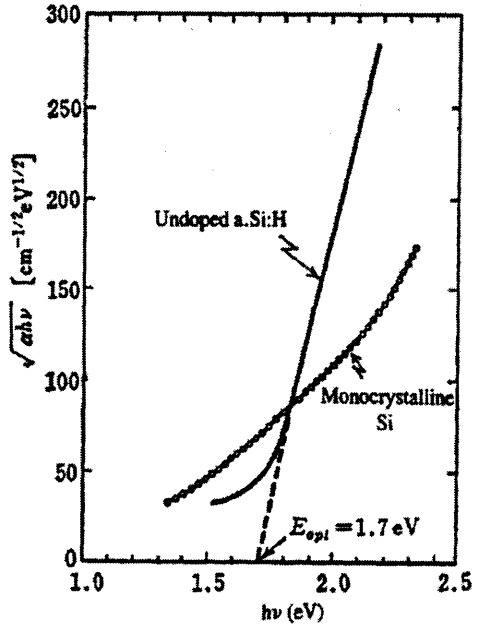

Figure 2.9 Method of determining the optical bandgap of α-Si:H [23].

2.3 Development of Amorphous Silicon and Microcrystalline Silicon Solar Cells

2.3.1 Amorphous Silicon Solar Cells

The conventional *p-n* junction solar cell design doesn't work for α-Si:H solar cells. Doping α-Si:H *p* or *n* type not only leads to active coordination as acceptors and donors but also creates recombination centers at deep levels within the bandgap. This obviates the simple *p-n* junction design: although a junction field would exist, photogenerated carriers would simply recombine before they could be accelerated and separated by the field. Instead, typical α-Si:H solar cells have a *p-i-n* configuration: an ultrathin, highly doped *p* layer; a thicker intrinsic (*i*) layer; and a thin *n* layer. The *p* layer and *n* layer set Fermi levels in the neighborhood of the valence and conduction bands, respectively, thus creating internal electric field for carrying the electrons and holes from the *i* layer to either electrode. However, band tails and defects prevent a full shift of the Fermi level from the center of the bandgap towards the band edges upon doping. In fact, the Fermi level cannot be shifted closer than 0.2 eV and 0.3 eV for highly doped *n* and *p* type α-Si:H, respectively, to the delocalized band states. Thus, the built-in potential of α-Si:H solar cells is limited and consequently the achievable open circuit voltage (Voc) is lower than that expected theoretically from the bandgap energy.

Depending on the deposition sequence of doped and intrinsic layers, α-Si:H solar cells can have a *p-i-n* or *n-i-p* diode structure. The typical configuration of *p-i-n* type single junction α-Si:H solar cell is schematically shown in Figure 2.10. For both structures the light is entering through the *p* layer that efficiently supports hole collection in the device owing to the fact of the smaller mobility of holes compared to that of electrons. A transparent conductive oxide (TCO) film contacts the α-Si:H diode from the

front side and, in the most simplest case, a metal film serves both as rear contact and back reflector. The very thin (10–30 nm) *p* and *n* doped layers build up an electric field over the intrinsic layer with typical thickness of 200–500 nm. Electrons and holes generated in doped layers do not (or only partly) contribute to the photo-current due to their short lifetime in highly doped α-Si:H. Therefore, wide-bandgap alloys (e.g., α-SiC:H) [24] and μc-Si:H [25] can be applied as *p* doped window layers to reduce absorption losses and increase Voc.

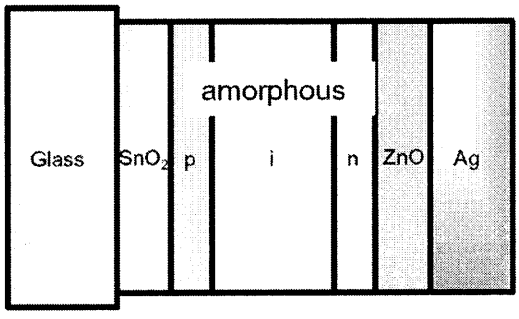

Figure 2.10 Typical configuration of single junction *p-i-n* type α-Si:H solar cell.

Collection of the photo-generated charge carriers and thus the solar cell performance are mainly determined by the material quality of the intrinsic layer as well as the strength and distribution of the internal electric field. Defects affect the charge carrier collection in both serving as recombination centers and influencing the electric field distribution over the *i*-layer. Schematic band diagram of solar cells is shown in Figure 2.11. According to the energy position of the Fermi level, defect states in the front part of the *i*-layer adjacent to the *p*-layer are positively charged (D^+ states), whereas defects adjacent to the *n*-layer are negatively charged (D^-). These charged defects enhance the electric field in the *p/i* and *n/i* interface regions, whereas the field is reduced in the volume of the *i*-layer [26].

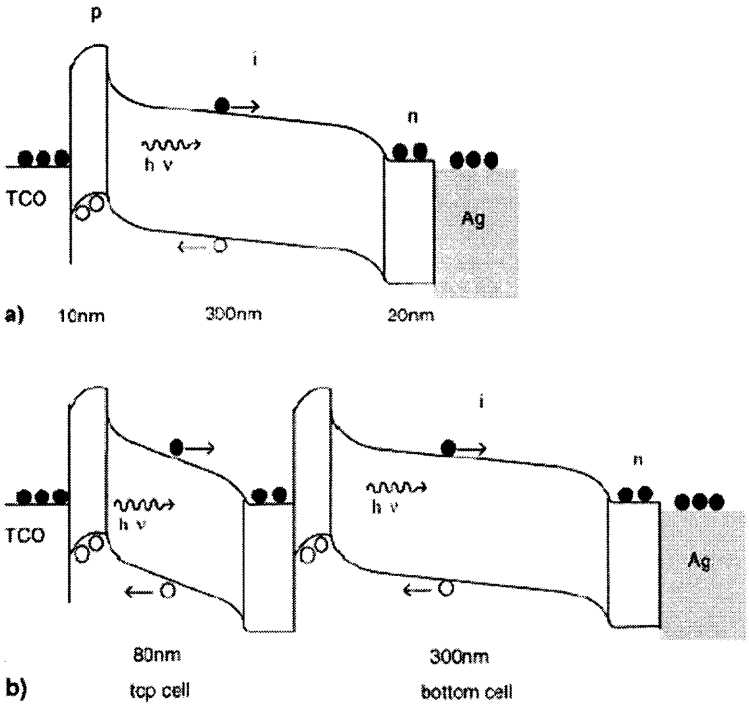

Figure 2.11 Band diagram of (a) single junction, and (b) tandem α-Si:H solar cells [26].

The *p/i* interface plays a crucial role in determining α-Si:H solar cell performance. Optimization of this region, e.g., introducing buffer layers to reduce the band discontinuity and prevent B from diffusing into *i*-layer [27], may improve both initial solar cell performance and the stability under light soaking. In general, this can be attributed to the decrease of recombination centers in the graded interface. The TCO/*p* interface is also of significance because a contact barrier may form in that area and μc-Si *p*-layer may provide a low Ohmic TCO/*p* interface in this case [26]. Relatively, the properties of the *n*-layer and the *i/n* interface are much less critical to solar cell performance because the local electron-hole pair generation rate is much smaller than that at the *p/i* interface.

2.3.2 Light-Induced Degradation in α-Si:H

Light-induced degradation in α-Si:H, Staebler-Wronski effect (SWE), was first observed as the large change due to sunlight in the conductivity of α-Si:H which was found to be completely reversible after annealing the films for several hours at temperatures above 150 °C [6]. Then, light-induced degradation of *n-i-p* α-Si:H solar cells was also reported in 1981 [28]. So far it is still one of the major factors seriously limiting the market share of α-Si:H based PV technology. Annealing the films or cells at over 170 °C could recover the degradation. However, this is not a practical solution. Since the discovery of SWE, the development strategies of α-Si:H solar cells have focused on not only improving the initial performance but also the stabilized conversion efficiency after long-term operation.

The changes of conductivity, as shown in Figure 2.12 [6], result from the introduction of metastable defects whose rate of creation and density depend on both the illumination intensity and temperature. The reversible changes that occur between an annealed state A and a light-soaked state B have become one of the most investigated phenomena in α-Si:H based materials and solar cells. However, progress has been relatively slow in obtaining a definitive understanding and control of the light-induced degradation due to the complex nature of the defects in α-Si:H as well as the difference in the microstructure of the materials studied which are prepared under a wide range of growth conditions. The general consensus so far is that hydrogen, which plays a key role in eliminating defects by passivating dangling bonds, also plays a key role in the creation of metastable defects that are sensitive to light [7].

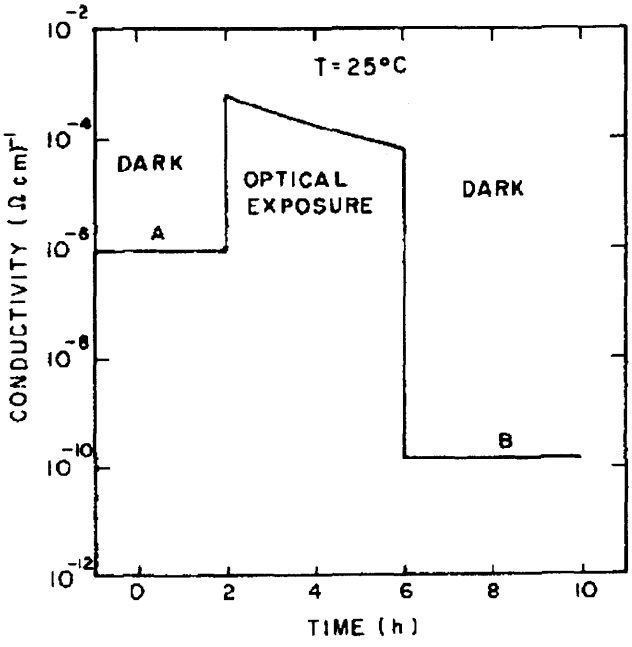

Figure 2.12 Conductivity of α-Si:H thin film as a function of illumination time with light [6].

Two general approaches to improve performance of α-Si:H solar cells are: (1) to improve the stability of α-Si:H materials, and (2) to make the *i*-layer thinner so that the stronger internal electric field sweeps out the photo-generated carriers before they are trapped or recombine and create metastable defects.

Stability of α-Si:H films under light soaking was improved by diluting SiH_4 with hydrogen [29] and similar effect was also observed in α-Si:H solar cells [30]. Now, diluting SiH_4 with hydrogen has been successfully used as the standard approach to obtain high quality α-Si:H based materials and solar cells [31]. The best quality α-Si:H films are grown at substrate temperature of about 200~250 °C using low power glow discharge of SiH_4 diluted in hydrogen. Under these circumstances, the as-grown defect density is ~10^{15} cm^{-3}, and the activation energy of the dark conductivity is ~0.8-0.9 eV. The optical bandgap of device quality α-Si:H is typically about 1.75 eV. The hydrogen

content of high quality α-Si:H films grown in PECVD systems is typically in the range of 7-10% and is mostly present in a monohydride bonding configuration [32].

Upon reducing *i*-layer thickness, the carrier collection is improved due to shorter path length for charge carries and enhanced internal electric field. However, insufficient light absorption and consequently low short circuit current density counteract the improvement in charge carrier collection. Thus the stacked-cell concept emerged to improve both the stability and overall conversion efficiency of α-Si:H based solar cells. As schematically sketched in Figure 2.11 (b), the top cell is much thinner than the bottom cell to fulfill the requirement of current matching. Consequently, the built-in potential in the top cell is distinctly higher, which strongly reduces light-induced defect creation. The thicker bottom cell is more stable than a comparable single-junction cell, because the intensity of the incident light is reduced due to the top cell acting as a filter. The practical problem of providing low-resistive inner *n-p* junctions has been solved by the use of microcrystalline contact layers [32].

2.3.3 Advances in α-Si:H Based PV Technology

Since α-Si:H solar cell prepared by glow discharge in SiH_4 was first reported in 1976 [4], α-Si:H based PV technology has had a development history of about three decades. The development of α-Si:H based solar cells proceeded along several tracks including improvements in materials, advances in device structures, and engineering of light trapping schemes, etc.

A major progress in the field of α-Si:H based materials is the ability to form α-SiGe:H and α-SiC:H alloys by concurrent decomposition of GeH_4 or CH_4. The bandgaps

of α-SiGe:H and α-SiC:H alloys depend on the concentrations of Ge and C as well as that of hydrogen. The alloys used in solar cells have up to about 60% Ge and up to about 20% C with bandgaps as low as 1.3 eV for the α-SiGe:H and as high as about 2.0 eV for α-SiC:H materials [7]. The transport properties of α-SiGe:H begin to degrade rapidly when the Ge content is increased above 45 at.% and the bandgap is reduced to less than 1.45 eV. Therefore, the narrowest bandgap region of α-SiGe:H used in solar cells is usually greater than about 1.45 eV [32].

The forming and tailoring of α-SiGe:H and α-SiC:H have allowed a variety of multi-junction solar cells to be developed. The structure of tandem α-Si:H based solar cells is illustrated in Figure 2.13 and even triple-junction stack has also been developed. In addition to higher stability, multi-junction solar cells offer the possibility to efficiently use the different part of the solar spectrum with thin component cells where the *i*-layer materials have appropriate bandgaps. Wide-bandgap top cells convert the blue and green part of the sunlight at high voltages, while the red and infrared part light is transmitted and absorbed in the bottom cell. The spectral splitting of the solar spectrum is clearly illustrated in Figure 2.14 by quantum efficiency curves measured for the component cells of an α-Si:H/α-Si:H/α-SiGe:H triple-junction solar cell. The top cell has a wide bandgap α-Si:H *i*-layer, the middle cell has a standard α-Si:H *i*-layer and the bottom cell contains a bandgap-graded α-SiGe:H *i*-layer [26]. Accomplished by optimizing factors such as bandgap profiling, hydrogen dilution for film growth, current matching, back reflection, and microcrystalline tunnel junctions, record stabilized efficiency of 13% has been reported using a triple-junction solar cell with α-Si:H and graded α-SiGe:H i-layers [33-35].

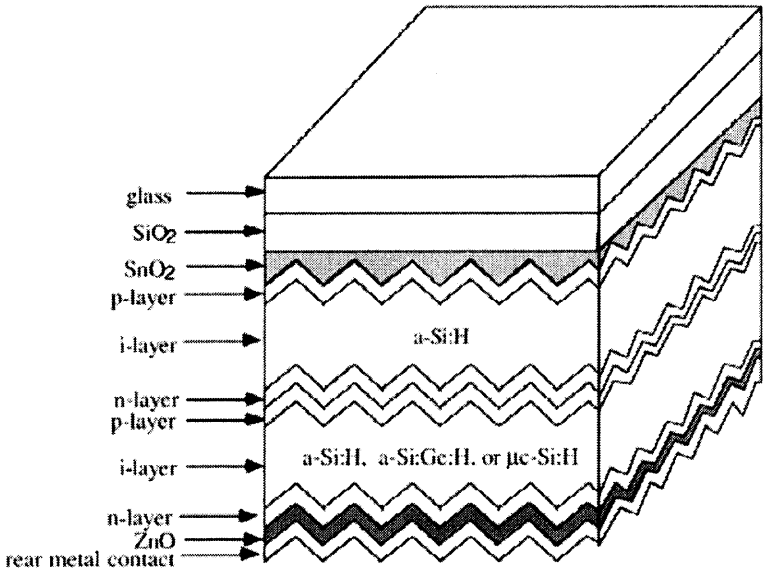

Figure 2.13 Schematic configuration of tandem α-Si:H solar cell [3].

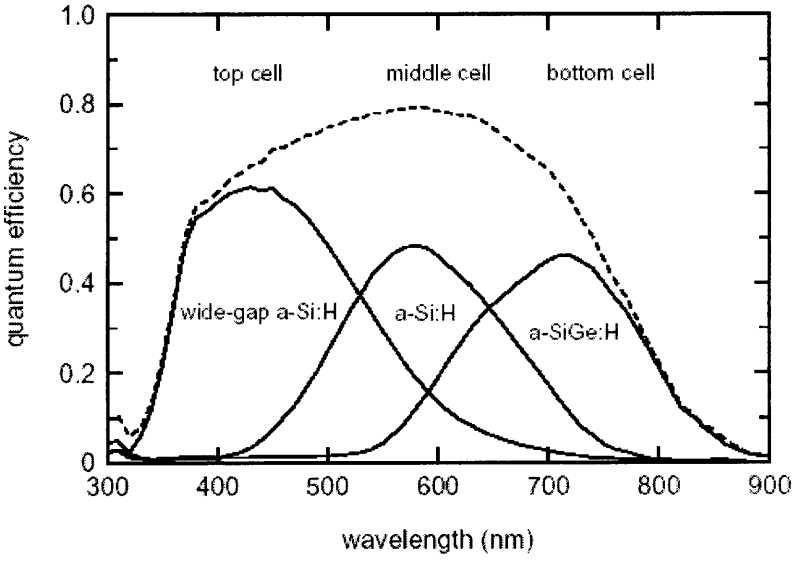

Figure 2.14 Quantum efficiency of an α-Si:H/α-Si:H/α-SiGe:H triple-junction solar cell [26].

Both tandem and triple-junction α-Si:H based PV modules, either using α-Si:H/α-SiGe:H or low-cost α-Si:H/α-Si:H *i*-layer combination, have been commercialized with up-to-date large-scale, high-throughput industrial manufacturing approaches such as large batch, in-line multi-chamber, and roll-to-roll processes [36-39]. Depending on the deposition sequence of doped and intrinsic layers, either superstrate (*p-i-n* multi-junction) or substrate (*n-i-p* multi-junction) configuration can be employed. The superstrate configuration is fully compatible with laser scribing techniques and thus facilitates the formation of an efficient thin film module with a monolithically integrated series connection of individual cells. With such series interconnection (shown in Figure 2.15), even very large modules (0.8 m^2) are still monolithic and can provide very high operating voltage. The glass substrate provides an effective encapsulation of the cell from the front side, thus the encapsulation materials "behind" the cell layers do not necessarily have to be transparent. The substrate configuration has the advantages of using a variety of cheap transparent or non-transparent substrates including flexible ones (e.g., stainless steel, plastic or metal foils, aluminum sheets, glass, etc.), the application of roll-to-roll processing which promises low production costs. Moreover, this configuration is ideally matched to the substrate temperature requirements in multi-junction devices. In contrast to the *p-i-n* structure where *i*-layer deposition above 200 °C deteriorates the *p/i* interface, the *n-i-p* process allows for the fabrication of low-bandgap bottom cells at high temperatures. The subsequently prepared top cell can be prepared at distinctly lower substrate temperatures favoring high open circuit voltages [26]. Unfortunately, the typical roll-to-roll process, which can continuously deposit α-Si:H onto stainless steel sheet over several kilometers long, doesn't allow one of the advantages of the thin film approach,

automatic interconnection during deposition, to be fully exploited. The tandem stack cells thus deposited need to be cut from the stainless steel roll and interconnected within the module, as in a bulk crystalline silicon module.

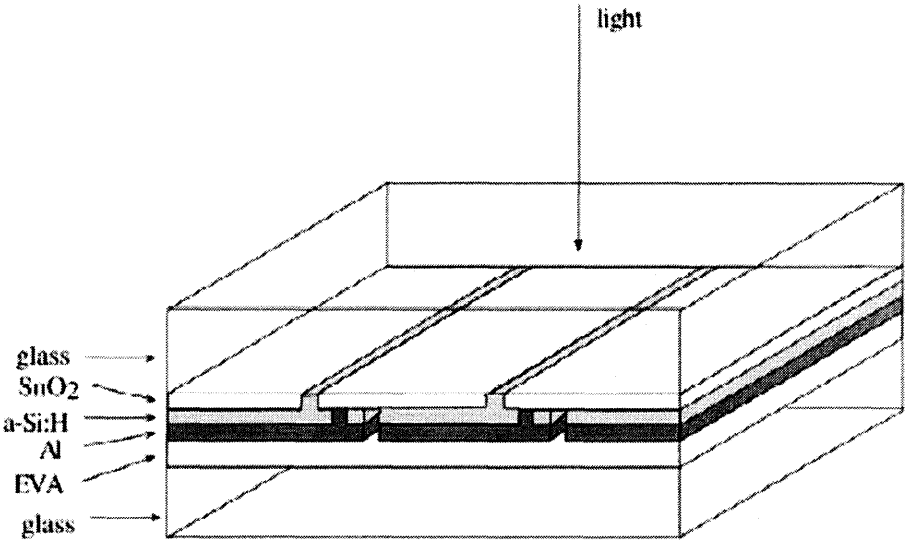

Figure 2.15 Series interconnection of α-Si:H modules [3].

The market shares of different PV technologies in 1999 is shown in Figure 2.16 [5] and similar distribution was confirmed in recent survey [3]. After the development over the past two decades, the high expectancy in α-Si:H based PV technologies is still curbed by the relatively low efficiency obtained so far and the light-induced degradation of such solar cells. Though stable conversion efficiency as high as 13% has been confirmed with laboratory α-Si:H solar cell, the efficiencies of current commercially available α-Si:H modules are only approximately 6-8%, which is much lower compared with the 10-15% conversion efficiencies of commercial bulk crystalline silicon PV modules [1, 3, 5].

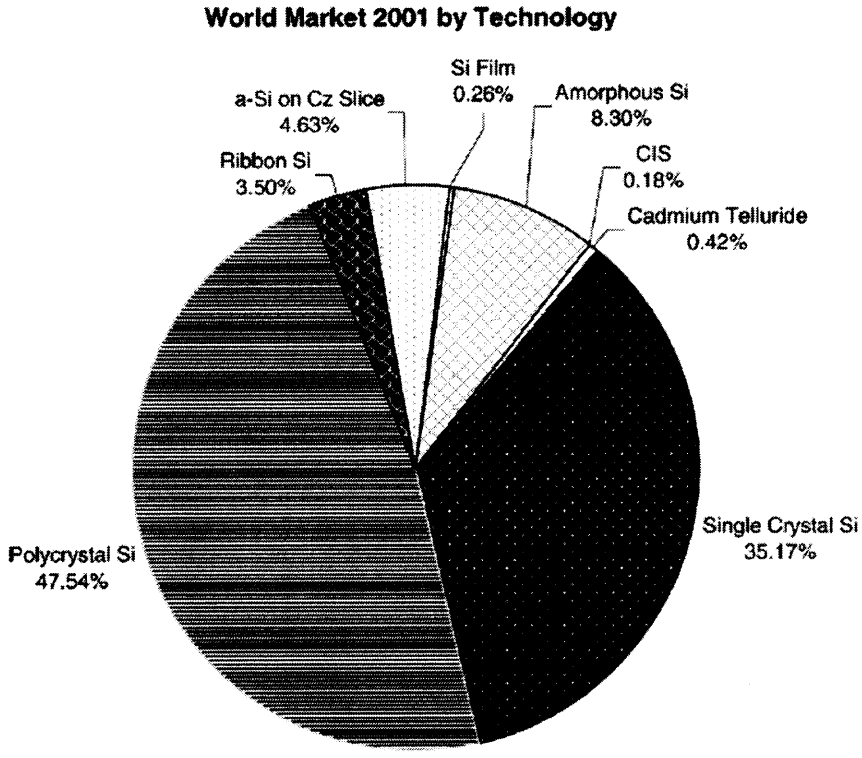

Figure 2.16 Market shares of different PV materials [5].

To survive well and capture an even more significant market share, α-Si:H based PV technology needs to further improve on its advantages, i.e., low-cost and large-scale fabrication. The current module prices of commercially available α-Si:H solar cells are approximately $3/Wp, which is lower than that of modules made from crystalline silicon wafers (~$4/Wp) [1]. The manufacturing costs can be even greatly reduced to lie in the range of $1-2/Wp by employing massive parallel process [36].

The visual appearance and large substrate size make α-Si:H PV modules suitable for facade applications. For example, PV panels can be integrated into buildings during construction. In addition to providing electricity, e.g., as back up power, it can lower the incremental costs of the system and enhance the exterior appearance of the buildings by

properly modifying the surface of PV panels to produce different colors. Such a building integrated photovoltaics (BIPV) concept could be one of the fast growing sectors in the future PV market.

2.3.4 Development of μc-Si:H Solar Cells

Under certain deposition conditions, e.g., strong presence of etching species such as hydrogen or fluorine in the discharge, μc-Si:H may form rather than α-Si:H. It is also promoted by the presence of dopants such as phosphorus that appear to act as nucleation centers. Both *p* and *n* doped μc-Si:H layers have been used in some multi-junction solar cell structures. The relatively high conductivity of doped μc-Si:H layers (compared to that of α-Si:H) makes a good tunnel junction and leads to a low series resistance when the layers are in contact with metal or transparent conductive oxide electrodes [32].

Early studies on μc-Si can be traced to 1968 when Veprek *et al* tried to deposit a microcrystalline semiconductor specimen in glow discharge plasma using chemical transport in hydrogen plasma [40]. During early 1980s, it was demonstrated that μc-Si:H films could be deposited from glow discharge of silane using similar approaches as that for α-Si:H deposition. Structural and electrical properties of thus deposited μc-Si:H films were also studied [41]. However, a breakthrough occurred in this filed only when device quality μc-Si:H films were prepared and incorporated into *p-i-n* type solar cells as the intrinsic absorber layers [42]. Two reasons explain why μc-Si:H wasn't taken into account for solar cell application as the active absorber layer in early days. Indirect bandgap of μc-Si:H limits its light absorption and correspondingly thick layer is

necessary. Meanwhile, grain boundaries may form carrier transport barriers if they are not passivated properly.

Typically, μc-Si:H was deposited using glow discharge of silane strongly diluted by hydrogen. Pioneering work in fabricating *p-i-n* type μc-Si:H solar cells using VHF-PECVD was reported in middle 1990s. The narrower bandgap of μc-Si:H offers an option of combining μc-Si:H solar cell with α-Si:H solar cell to take the advantage of long wavelength absorption as in the case of standard α-Si:H/α-SiGe:H tandem solar cells. The concept of 'micromorph' tandem solar cell, which consists of a mixed stack α-Si:H/μc-Si:H solar cell, was introduced and stable efficiency over 7% was reached in a short period. More effective utilization of the solar spectrum by incorporation of μc-Si:H *i*-layers is demonstrated by the comparison of spectral responses of α-Si:H and μc-Si:H solar cells, as shown in Figure 2.17. The μc-Si:H absorption in the near infrared region opened a potential of additionally making use of sun spectrum to a higher extent and consequently increasing the current of solar cells [43-46]. Such μc-Si:H solar cells also showed excellent resistance to light-induced degradation [44]. Furthermore, μc-Si:H based solar cells are of significance because of its full compatibility with the α-Si:H PV technology and cost reduction resulting from the replacement of Ge containing intrinsic layers by μc-Si:H.

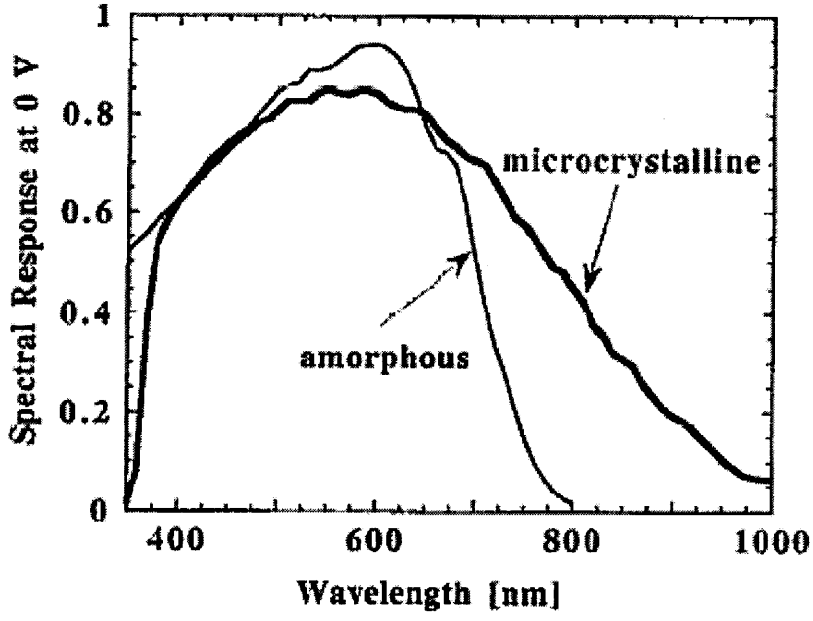

Figure 2.17 Spectral response of a 1.7 μm thick entirely μc-Si:H solar cells in comparison of a α-Si:H solar cell [43].

Following the success of VHF-PECVD, some other deposition techniques were also explored with considerable efforts. Among them, Hot-Wire CVD (HWCVD) has attracted relatively more attention and device quality μc-Si:H films have been made by this method [47-48]. The principle of the success of HWCVD in obtaining high quality films is that the feedstock gas, e.g., SiH_4, is efficiently decomposed into atomic radicals at the surface of the filament (usually tungsten or tantalum) which is generally kept at a temperature higher than 1500 °C. In combination with a low pressure, this enables a high deposition rate without gas-phase nucleation of particles. The α-Si:H films deposited by HWCVD also have lower hydrogen concentration compared with that in the α-Si:H films deposited by RF-PECVD [49], this might be helpful to reduce the light-induced degradation of α-Si:H.

Though VHF-PECVD has been widely used to deposit high quality μc-Si:H, at those high frequencies, problems arise due to enhanced ohmic losses in the electrical parts. Further problems come up when the wavelength of the plasma excitation (e.g., ~3 m for 100 MHz) becomes comparable to reactor and substrate dimensions (~1 m^2 for industrial production). Inter-electrode voltage inhomogeneities increase with increasing excitation frequency and cause inhomogeneities in the deposition rate [50]. For this reason, lower excitation frequencies facilitate deposition of μc-Si:H on large substrates. Thus, conventional RF (13.56 MHz) excitation frequency, which is the most studied technique and compatible with existing equipment, is favorable and any new breakthrough can be most readily incorporated into the existing industrial processes used, for example, in the fabrication of solar cell modules. High quality μc-Si:H has been deposited in a high pressure regime using conventional RF-PECVD [51] and now it is one of the areas in μc-Si:H research attracting extensive attention. μc-Si:H solar cells with reasonable performance have been fabricated using RF-PECVD by several groups [52–55].

Over the past few years, initial efficiencies over 7% for single junction μc-Si:H solar cells and 10-12% for α-Si:H/μc-Si:H tandem solar cells have been reached using RF-PECVD or VHF-PECVD [55-56]. A tandem α-Si:H/μc-Si:H solar cell module with 14.5% conversion efficiency using an effective light trapping by a transparent interlayer between the top and bottom cells has been reported [57]. However, most of the results mentioned above were obtained in laboratory scale deposition systems and light trapping enhancement schemes, e.g., textured transparent conductive oxides (TCO), back reflection layer (Ag or ZnO/Ag), etc., were usually employed. For those publicly reported

modules, the technical details and cost are still tightly guarded secrets. Though most groups once involved in α-Si:H based PV technology are working on μc-Si:H solar cells as well and promising results have been reported, extensive efforts are still needed to commercialize μc-Si:H solar cells due to a lot of challenges in this field such as large-scale, uniform deposition, device structure design, optical engineering, etc.

2.4 Advances in Understanding Si:H Deposition Process

2.4.1 Deposition Process of Si:H Prepared Using PECVD

The deposition process of PECVD is very complicated since the physical and chemical interactions within the plasma and growing surface are dependent on all the parameters related to the plasma and deposition apparatus. Recently, crucial novel insights, which play an essential role in obtaining high quality α-Si:H and μc-Si:H layers, have been gained on the PECVD processes due to the application of modern *in situ* and *real time* diagnostic techniques.

Generally, monosilane, SiH_4, is used together with hydrogen dilution as the Si precursor in deposition of Si:H thin films using PECVD. Depending on where the events occur, the film growth process can be classified to three sub-processes, i.e., gas phase processes, surface processes, and sub-surface processes. Electron impact dissociation of SiH_4 molecules is the primary event within the plasma. The electron temperature in RF-PECVD at low plasma power is typically 2 eV, as shown in Figure 2.18 [58]. All electrons participating in radical and ion generation are in the tail of the energy distribution. The dominant primary processes in SiH_4 or SiH_4 + H_2 plasma are the generation of neutral SiH_3 and SiH_2 by electron impact dissociation of SiH_4 with

estimated thresholds of ~8.8 and 9.5 eV, respectively. Due to higher thresholds for ion production, the rate of ion generation is much lower than that of neutral radical production. Secondary processes in the SiH_4 + H_2 plasma are dominated by the reaction of SiH_4 and H_2 with the high reactivity radicals such as SiH_2. These can be beneficial as when SiH_2 reacts with H_2 to form SiH_4, or detrimental as when SiH_2 reacts with SiH_4 to form Si_2H_6. The successive insertion reaction, $SiH_2 + Si_nH_m \rightarrow Si_{n+1}H_{m+2}$, results in the formation of higher silane species and finally in powder formation. It is widely believed that the desired species are SiH_3 and atomic hydrogen (H) radicals, whereas SiH_2, SiH, and atomic Si radicals, as well as higher silanes Si_xH_y ($x \geq 2$) are detrimental to α-Si:H properties [59, 60].

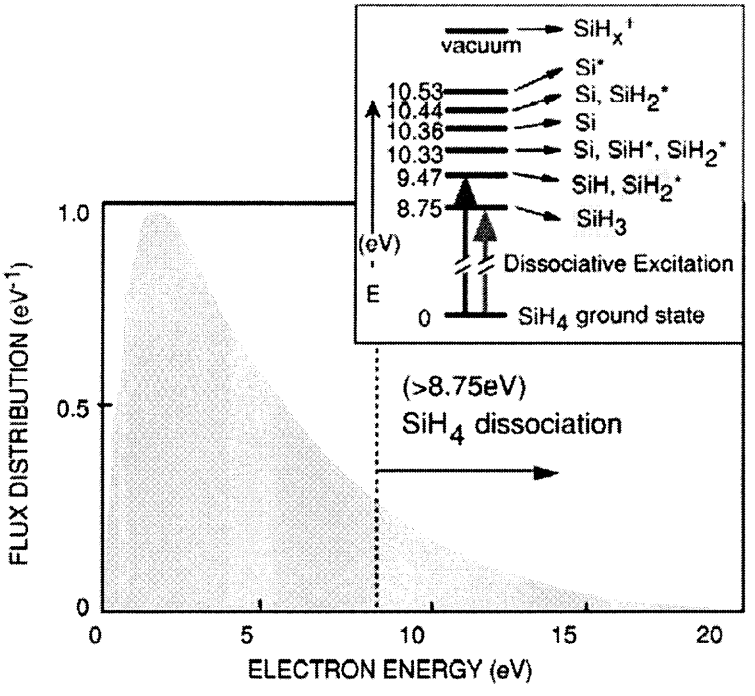

Figure 2.18 Schematics for the dissociation pathways of SiH_4 molecules excited by the electron impact [58].

Generally, high quality α-Si:H films are deposited at relatively low growth rate in actual device manufacturing process. At increased deposition rate, which is preferred for cost reduction, light-induced degradation becomes more significant. Recently, it has been identified that high-order silane-related radicals may be a major cause of the degradation of α-Si:H film properties at high growth rate. In the case of high rate growth of α-Si:H, the so-called short lifetime radicals such as SiH_2, SiH and Si survive due to less collision with SiH_4, and thus contribute to the film growth, leading to complicated reactions on the growing film surface, and usually causing higher dangling bond density in the resulting film due to high reactivity of those short lifetime radicals and less or no diffusion on the growing surface. Increasing the flow rate of SiH_4, which is employed to avoid the depletion of parent molecules, results in higher silane related reactive species within the plasma, leading to powder formation [61]. It is, therefore, suggested that suppression of gas phase high-order silane-related radicals as well as short-lifetime radicals is a clue for obtaining stable α-Si:H solar cells at high growth rate and several possible approaches to reduce SiH_2 density in α-Si:H films, e.g., reducing electron temperature, hydrogen dilution, and increasing substrate temperature, have been attempted. It is believed that higher plasma excitation frequency is the most effective factor that can lead to increased electron density and decreased electron temperature simultaneously. Hydrogen dilution suppresses the higher silane formation because of the recombination between H_2 and SiH_2. High substrate temperature may support the hydrogen elimination reaction in the surface region and it may also reduce the electron temperature [61-64].

Atomic hydrogen has been widely recognized as playing a crucial role in the formation of μc-Si:H. It can be generated from either SiH_4 or H_2. However, atomic hydrogen is annihilated by the recombination reaction with SiH_4 ($H + SiH_4 \rightarrow H_2 + SiH_3$). Thus, high hydrogen dilution suppresses the recombination reaction and allows a sufficient atomic hydrogen flux to the growing surface. It has been demonstrated that high rate growth of device quality μc-Si:H, and possibly α-Si:H as well, can be obtained in a SiH_4 depletion regime at high pressure, high hydrogen dilution, and relatively high plasma power [51, 65, 66]. High plasma power is helpful to increase the deposition rate while high hydrogen dilution can suppress the annihilation of atomic hydrogen and lead to increased atomic hydrogen density. On the other hand, high pressure can reduce the electron temperature as well as reduce the damage resulting from high-energy ion bombardment.

Surface processes have been considered as the limiting factor of α-Si:H growth. Generally, plasma species interacting with the growing α-Si:H surface can be classified as either lower reactivity radicals such as SiH_3 that can diffuse along the surface through physisorption states, or higher reactivity radicals such as SiH_2 and Si_2H_4 that can insert at the surface without significant diffusion. The surface diffusion model, which emphasizes the diffusion and crosslink of film precursors (SiH_3) on the fully hydrogen covered growing α-Si:H surface, has been widely recognized [67-68]. This simplified model proposes that, in the temperature range below 350 °C, SiH_3 reaching the growing surface of α-Si:H starts to diffuse on the almost fully hydrogen covered surface. Surface diffusing SiH_3 abstracts surface hydrogen, forming SiH_4 and leaving Si-dangling bond on

the surface, and another surface diffusing SiH_3 finds the dangling bond and consequently forms Si-Si bond.

However, it is argued that hydrogen elimination to form Si-Si network is the rate-limiting step at lower temperature, and bulk dangling bond density is determined primarily through sub-surface processes, rather than by surface processes alone. The dangling bond defects arise from the weak bonds by the defect pool process, namely inter-conversion between weak Si-Si bond and Si dangling bond mediated by H. Elimination of excess hydrogen in Si network through interactions with free hydrogen radicals and ions has also been proposed [69-70]. Therefore, the possible processes of SiH_3 on the growing surface of α-Si:H can be schematically illustrated as that in Figure 2.19 [71].

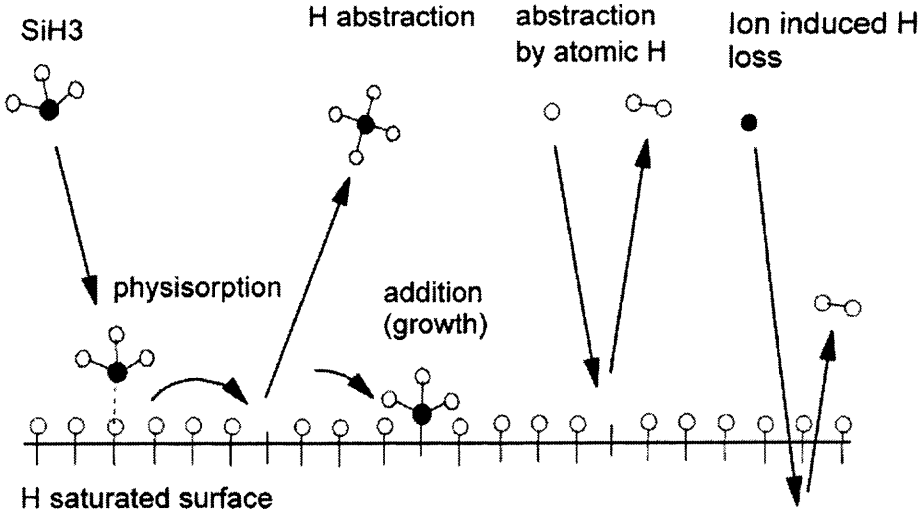

Figure 2.19 Schematic processes of SiH_3 radicals on α-Si:H surfaces [71].

The impact of sub-surface processes during α-Si:H growth has also been addressed through the concept of 'chemical annealing', which emphasizes the interaction between excited plasma species and the top few monolayers of the growing film, as well as the stabilization of ~100 Å top layer through hydrogen penetration followed by relaxation of weak Si-Si bonds [72-73].

The surface reaction model has been extended and some other models, e.g., etching model and chemical annealing model, have also been proposed to explain the formation of μc-Si:H [74]. Among these models, the most controversial issue relates to the role of hydrogen during μc-Si:H formation. Thus the layer-by-layer (LBL) technique has been used to investigate the crystallization of Si:H films by atomic hydrogen treatment. However, ''chemical transport'' during hydrogen plasma treatment makes it difficult to explain the LBL experimental results [75-76]. So far the microscopic mechanism of μc-Si:H growth is still not clear. Recently, studies of the surface, sub-surface, and bulk Si-H bonding in α-Si:H, mixed-phase (α + μc-Si:H), and single phase μc-Si:H provide results on the evolution of the sub-surface Si-H bonding with thickness in α-Si:H. It is suggested that SiH_n complex, formed by insertion of hydrogen into a strained Si-Si bond, contribute to the reactions that result in μc-Si:H nucleation [77-79]. It has also been reported that stress increases with increasing film thickness [80-81], leading to the increase of strained Si-Si bonds concentration. Furthermore, because hydrogen inserts at strained Si-Si bonds to generate SiH_n species, the SiH_n content is expected to increase with increasing thickness. Thus, two features in film growth are proposed to be required for microcrystallite nucleation from the α-Si:H phase: (i) high stress in the film, and (ii) a high hydrogen flux from the plasma to insert hydrogen at the

resulting strained Si-Si bonds. On this basis, it can be concluded that the bulk film processes occurring on the macroscopic scale during growth can influence the ultimate film properties on the microscopic [60].

2.4.2 Microstructural Evolution During Si:H Deposition

Recent studies suggested that optimum α-Si:H solar cells with high efficiency and stability should be prepared with *i*-layers being amorphous, yet as close as possible to the amorphous-to-microcrystalline transition boundary. However, as revealed by such studies, the amorphous-to-microcrystalline transition boundary is highly dependent on not only the hydrogen dilution ratio but also the substrate materials and accumulated film thickness. The factors affecting this dependence include (1) amorphous substrate may suppress μc-Si:H formation by imposing its structure on the growing film, (2) regions of higher ordering develop gradually as the α-Si:H grows and these serve as sites for microcrystal formation, and (3) stresses build up in the network and then are released through the development of roughness or void structures that may also induce microcrystal formation [82-84].

Recently, it has also been suggested that the optimum μc-Si:H *i*-layers for solar cells are deposited near the 'edge' of microcrystalline-to-amorphous phase transition without entering α-Si:H phase [55, 85, 86]. Owing to the critical importance of Si:H deposition near the boundary between the α-Si:H and μc-Si:H growth regimes, the development and application of deposition phase diagram pioneered by Penn State University have attracted great attention. The deposition phase diagram describes the accumulated thicknesses at which different microstructure and phase transitions are observed during the Si:H film growth process. In such a diagram, the transition

thicknesses are plotted as continuous functions of a key deposition parameter, mostly the H_2-dilution gas flow ratio R = $[H_2]/[SiH_4]$ in the low temperature PECVD process since it exerts the greatest control over the phase of the film—from α-Si:H at low R to μc -Si:H at high R [87-88].

Real time spectroscopic ellipsometry (RTSE) has been applied to study the microstructural evolution during Si:H deposition and establish the deposition phase diagram. Figure 2.20 shows the overlying surface roughness layer thickness d_s versus the bulk layer thickness d_b for three Si:H depositions as deduced by RTSE [89]. The general features of the microstructure and phase evolution during the growth of α-Si:H films, depicted as the evolution of the surface roughness layer are enumerated as [87]:

(i) Smoothing (or coalescence) of initial amorphous nuclei in the first ~100 Å of bulk layer thickness;

(ii) An even larger smoothening effect due to calescence of initial microcrystalline nuclei which can only be observed for depositions at higher R than those in Figure 2.20;

(iii) Stable surface growth as observed in Figure 2.20 (a), which corresponds to the highest performance and stability materials. The highest electronic performance α-Si:H materials exhibit the largest surface smoothing magnitudes and rates during coalescence as well as stable smooth surface throughout the growth of thick films;

(iv) Amorphous roughening transition as observed in Figure 2.20 (a), which corresponds to the beginning of the degradation of the material properties and stability;

(v) Roughening due to the amorphous-to-(mixed-phase-microcrystalline) transition; and

(vi) (Mixed-phase-microcrystalline)-to-(single-phase-microcrystalline) transition featuring a transition from roughening to smoothening. Once the crystallites have coalesced to cover the growing film surface completely, single-phase μc-Si:H growth proceeds with a resumption of surface roughening.

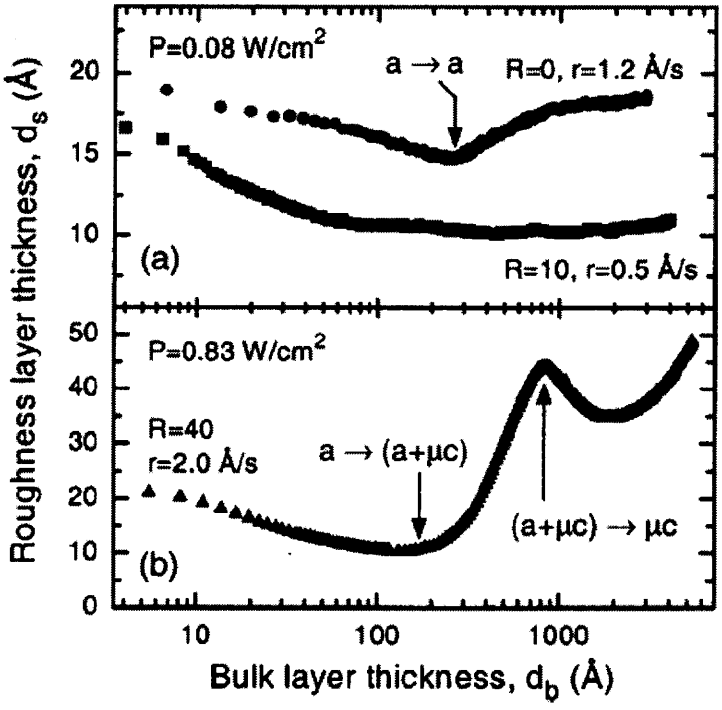

Figure 2.20 Surface roughness evolution for Si:H films prepared on c-Si substrates by RF-PECVD at different H_2 dilution ratio [89].

The simplest deposition phase diagrams incorporate only the single transition from amorphous growth regime to mixed-phase (amorphous + microcrystalline) growth regime (feature (v)) [90]. The so-called "extended" deposition phase diagrams which were developed recently include all the three transitions during the evolution of surface roughness layer thickness as shown in Figure 2.20:

(i) An onset of roughening due to surface morphological evolution during single phase α-Si:H film growth [denoted α → α],

(ii) An onset of roughening due to the nucleation of crystallites from the α-Si:H matrix leading to mixed-phase (α + μc)-Si:H [denoted α → (α + μc)], and

(iii) An onset of smoothing due to crystallite coalescence leading to single phase μc-Si:H [denoted (α + μc) → μc].

Figure 2.21 shows an "extended" deposition phase diagram, which provides deeper inside into the electronic quality of α-Si:H prepared near the α → (α + μc) transition, as well as provides the thickness ranges and conditions under which single-phase μc-Si:H films are obtained [87-89].

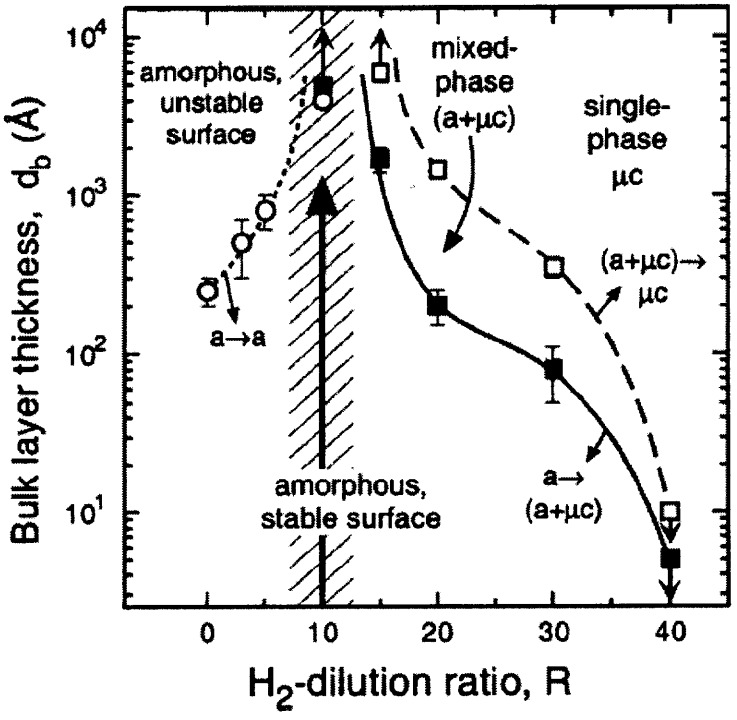

Figure 2.21 Deposition phase diagram for Si:H film growth on c-Si substrates held at 200 °C [89].

Larger $\alpha \rightarrow \alpha$ transition thickness indicates longer surface diffusion lengths and correlated with higher quality α-Si:H materials for the *i*-layer of electronic devices. On this basis, Figure 2.21 suggests an optimum in the region near R = 10 where the α-Si:H surface remains stable throughout deposition to at least 4000 Å (indicated by vertical arrow). This α-Si:H material has been described as being 'protocrystalline' Si:H owing to the fact that if the film were to continue accumulating, then the $\alpha \rightarrow (\alpha + \mu c)$ transition would be eventually traversed [83]. In addition to providing guidelines to obtaining optimum α-Si:H *i*-layers for PV applications, the deposition phase diagram has also been applied to optimize *p*-layers though the current work is inconclusive. It should also be noted here that deposition phase diagrams are very sensitive to the underlying substrates and other plasma parameters. The optimum window may be significantly narrowed by changing plasma parameters, e.g., increasing plasma power while keeping other parameters constant [87].

The TEM studies on μc-Si:H films prepared by VHF-PECVD have demonstrated that, for samples below or close to the $\alpha \rightarrow \mu c$ transition, nanocrystals of silicon embedded in α-Si:H matrix are observed. Under conditions favoring the formation of a high crystalline volume fraction, columnar growth is observed [91]. Cone-like crystallites grown from α-Si:H matrix has been clearly observed by TEM studies [87, 92]. Figure 2.22 illustrates the construction of a cone growth model of micro-crystallites in reference to the surface roughness evolution. In this model, it is assumed that all microcrystalline nuclei originate at the $\alpha \rightarrow (\alpha + \mu c)$ transition layer thickness (~300 Å, in this case). The area density of such nuclei is assumed to be N_d, and the nuclei are assumed to grow preferentially at the expense of the α-Si:H phase with a constant, thickness-independent

cone angle, θ. The cones are assumed to be spherically capped whereby the cap radius r evolves with bulk layer thickness according to $r = d_b - d_{b,t}$. Applying this geometry, N_d and θ can be deduced from the values of $\Delta d_b = d_{b,c} - d_{b,t}$ and $\Delta d_s = d_{s,c} - d_{s,t}$. Here $d_{b,t}$ and $d_{s,t}$ are the bulk and surface roughness layer thicknesses at the $\alpha \rightarrow (\alpha + \mu c)$ transition and $d_{b,c}$ and $d_{s,c}$ are the corresponding values at the $(\alpha + \mu c) \rightarrow \mu c$ transition [87].

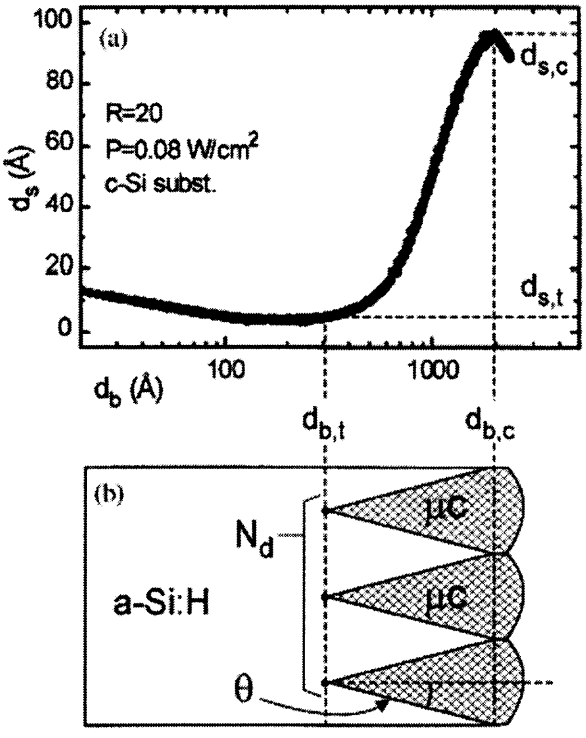

Figure 2.22 Schematic construction of the cone growth model [87].

The deposition phase diagrams provide a convenient guide to the device design by describing the regimes of layer thickness and deposition parameter space within which single-phase α-Si:H, (α+μc)-Si:H, and single-phase μc-Si:H are obtained. Figure 2.23 shows the proposed schematic structure of ~5000 Å thick Si:H films on α-Si:H substrate

films deposited at R = 0, given as a continuous function of R along with the thicknesses of the $\alpha \rightarrow (\alpha + \mu c)$ and $(\alpha + \mu c) \rightarrow \mu c$ transition boundaries. In such structures, the cone angle for crystallite growth is relatively constant at 15-20° and the nucleation density increases rapidly with increasing R [88].

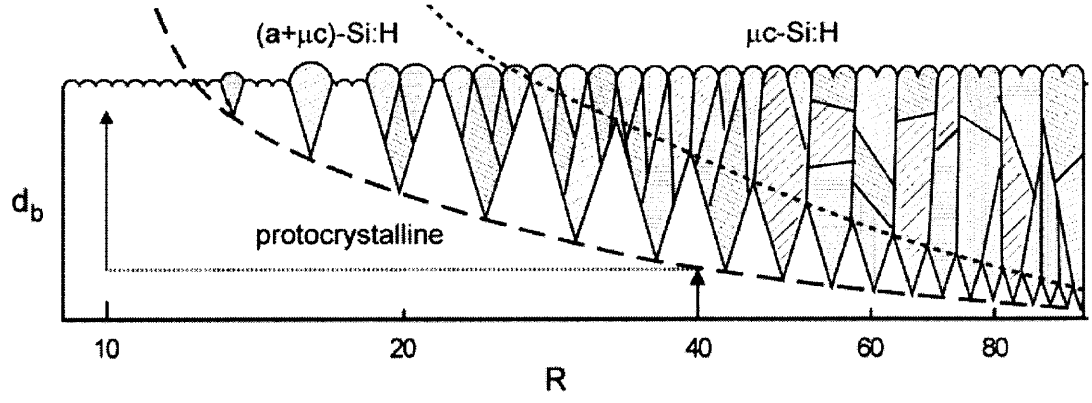

Figure 2.23 Schematics of the structure of Si:H films prepared as a function of R [88].

Though highly expected, the successful commercialization of μc-Si:H based PV devices with real low-cost, high efficiency, and good stability will take some time longer than once expected and need extra efforts. The critical issues identified by recent researches in obtaining high quality μc-Si:H films and devices, e.g., relatively harsh deposition conditions, non-uniformity, narrow optimal processing window, etc., and the recent advances in fabricating μc-Si:H PV devices as well as understanding the plasma chemistry and the microstructural evolution during deposition of μc-Si:H films using PECVD, provide valuable information on the further development of low-cost, high performance μc-Si:H solar cells.

CHAPTER 3

EXPERIMENTAL METHODOLOGY

3.1 Radio Frequency Plasma Enhanced Chemical Vapor Deposition System

The early success in fabricating μc-Si:H solar cells was achieved using VHF-PECVD [43]. It is generally believed that higher plasma excitation frequency can reduce the electron temperature and simultaneously increase the electron density within the plasma, which favor the growth of high quality α-Si:H and μc-Si:H films [63]. Though VHF-PECVD has been widely used in fabricating μc-Si:H solar cells, this less standard approach may present problems in matching the well-established RF-PECVD technique used in industrial manufacturing of α-Si:H based PV devices. Non-uniformity issue may arise as well when the plasma excitation frequency is high enough such that its wavelength is comparable with the reactor and substrate dimensions used in industrial production. Therefore, there is a move recently towards the studies on fabricating μc-Si:H solar cells using conventional RF-PECVD, which has proven to be capable of producing high quality μc-Si:H PV devices by several groups including ourselves [52-55].

A compact, single chamber PECVD system with conventional RF power excitation at 13.56 MHz was constructed at EPV. The overall structure of this R&D RF-PECVD system is shown in Figure 3.1. This low-cost, batch-process type system, with a parallel-plate (capacitively coupled) deposition chamber, is capable of simultaneously coating 4 plates equal in size of 15" × 12". The vacuum chamber is routinely exposed to the ambient for loading and unloading substrates. The base pressure of the deposition chamber is usually in the lower 10^{-6} torr range or below. No special measures, except for

regular sealing, are taken to prevent the chamber from ambient contamination. The use of this conventional RF-PECVD system takes the following advantages:

- Low-cost, simple, high throughput manufacturability resulting from simple design, large substrate area, easy operation, high gas utilization, controllable contamination profile, and low maintenance;
- Direct coupling between fundamental materials study and practical device engineering;
- Good scale-up capability resulting from compatibility with the existing large-area α-Si:H thin film PV manufacturing equipment and processes.

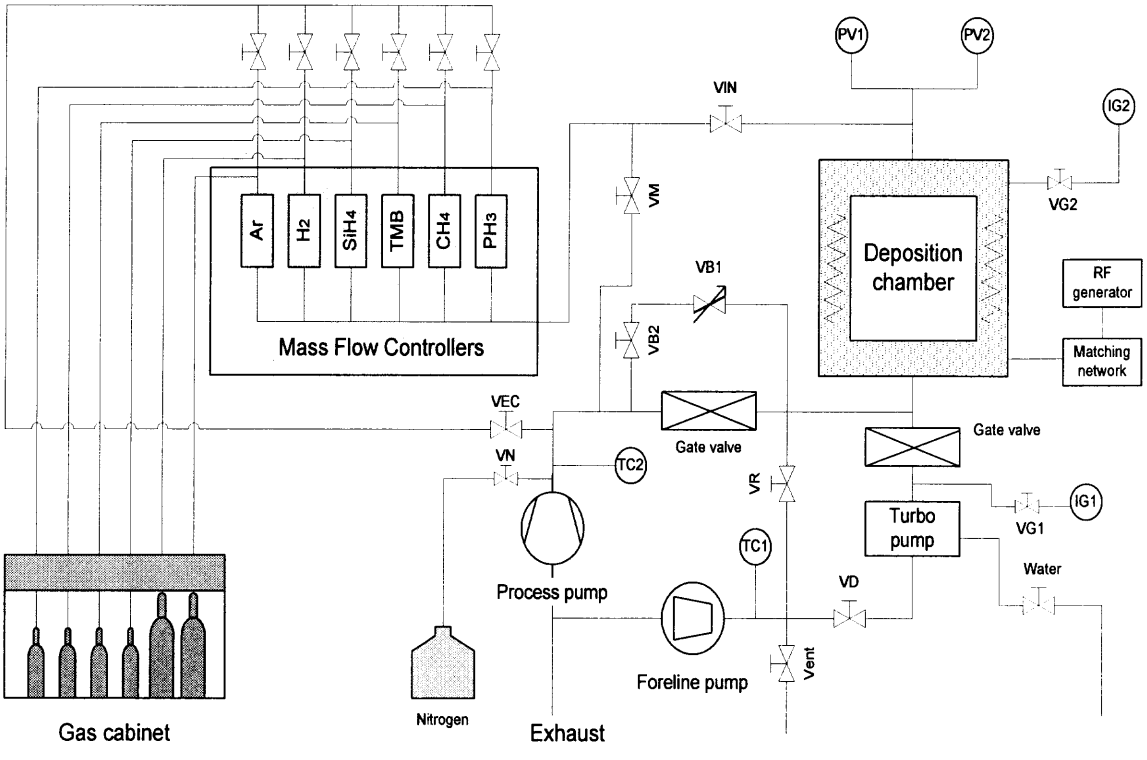

Figure 3.1 Schematic configuration of the single chamber RF-PECVD system.

The RF-PECVD system shown in Figure 3.1 mainly consists of six subsystems as described in the following:

- A vacuum system including a high-vacuum chamber and three vacuum pumps, i.e., a dry process pump, a turbo-molecular pump, and a dry backing pump. Uniform heating is achieved using heater strips installed outside the chamber.

- A batch-process type deposition chamber capable of simultaneously coating 4 plates of 15" × 12" in size.

- An RF power generation and matching network feeding RF power into the deposition chamber.

- A process gas manifold capable of delivering 6 different gases or gas mixtures to the PECVD reactor.

- An exhaust gas handling system.

- A system control including system control cabinet, computer, and associated hardware and software.

The entire deposition system, including vacuum sub-systems, heating, RF power supply, and gas manifolds, is fully computer controlled. High accuracy control of gas flow and automatic grading, i.e., changing feedstock gas flow rate without interrupting the ongoing deposition process, are achieved with computer-controlled mass flow controllers. While the entire system simulates a low-cost manufacturing process, the system automation allows for the realization of easy but tight control over the deposition process, which facilitates the implementation of various specially designed R&D tasks.

3.2 Structure of μc-Si:H Solar Cells

The major goal of this research is not pursuing record high efficiency μc-Si:H solar cells. Instead, it focuses on developing deposition processes of high quality μc-Si:H *i*-layers, which is critical to the fabrication of μc-Si:H PV devices. Therefore, all μc-Si:H solar cells fabricated in this research have a relatively simple device structure as shown in Figure 3.2. The single junction, *p-i-n* type solar cells are deposited onto commercial grade SnO_2 superstrate coated on 1/8 inch thick soda-lime glass. In such a typical μc-Si:H solar cell, a very thin boron doped α-SiC:H layer is first deposited as the *p*-layer, followed by an intrinsic μc-Si:H layer as the active absorber layer (*i*-layer), and then a thin phosphorous doped α-Si:H layer is deposited as the *n*-layer. A layer of Al, without any TCO as part of the rear light reflection enhancement, is directly deposited over the *n*-layer as the back reflector and electrical contact.

The simplicity of the device structure not only simulates the existing low-cost, large-area α-Si:H PV manufacturing technology, but also helps focus the research on exploring the deposition processes and properties of μc-Si:H *i*-layers. To reduce the factors affecting the evaluation of the deposited μc-Si:H *i*-layers, deposition conditions for *n*-layers and Al back contacts are basically kept constant throughout this study. On the other hand, modifications are often made during *p*-layer deposition to induce nucleation of the investigated μc-Si:H.

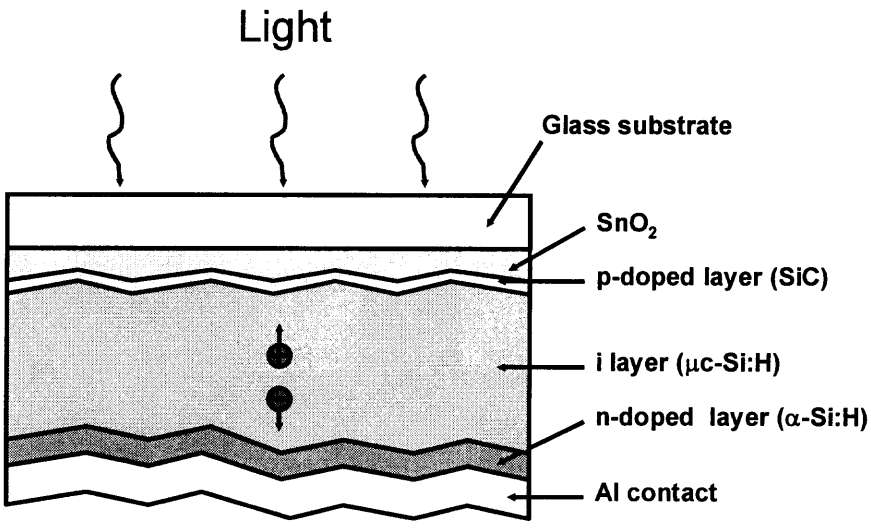

Figure 3.2 Schematic configuration of single junction *p-i-n* μc-Si:H solar cells.

3.3 Fabrication of μc-Si:H Solar Cells

The fabrication of real PV devices was preceded by depositing a number of α-Si:H films and single junction *p-i-n* α-Si:H solar cells to verify the performance of the RF-PECVD system. The *p*-layers of the α-Si:H solar cells were deposited using mixtures of silane and methane as feedstock gases, and trimethylboron (TMB, $B(CH_3)_3$) as doping gas, the *i*-layers were deposited using plasma of moderately hydrogen diluted silane, and the α-Si:H *n*-layers were deposited using phosphine as doping gas. The plasma power and chamber pressure are generally moderate and the deposition time are determined by the desired thickness of respective layers. These α-Si:H solar cells fabricated using the R&D RF-PECVD were optimized to obtain reasonable device performance comparable with that of 'standard' device fabricated using existing low-cost, large-area α-Si:H PV manufacturing process. The optimized recipes for the doped layers are later used, with modifications when necessary, in the fabrication of μc-Si:H solar cells.

Glow discharge of highly hydrogen diluted silane is used as the basic approach to systematically investigate the deposition of μc-Si:H *i*-layers using conventional RF-PECVD. By changing deposition parameters, e.g., chamber pressure, hydrogen dilution ratio, gas composition, plasma power, and substrate temperature, all three layers are deposited in the same chamber without any movements of the substrates or the reactor. Due to relatively lower optical absorption of μc-Si:H compared to that of α-Si:H, thick μc-Si:H *i*-layer is needed to obtain sufficient carrier collection. Thus, relatively high chamber pressure and high plasma power are usually used to facilitate the formation of μc-Si:H and maintain a reasonable growth rate. The substrate temperatures are kept near 200 °C.

Though the microscopic mechanism of μc-Si:H growth has yet to be better understood, it is generally believed that the initial nucleation of μc-Si:H crystallites, on α-Si:H, α-SiC:H or other under-layers, is critical to obtaining high quality μc-Si:H films. In this study, a wide variety of seeding processes are employed to enhance the nucleation and growth of bulk μc-Si:H *i*-layers. The effects of seeding schemes and growth conditions for bulk μc-Si:H *i*-layers on the microstructure and device performance of μc-Si:H solar cells are evaluated by device performance test and structural characterization.

The seeding process results in a transition layer near the *p/i* interface sandwiched between the conventional α-SiC:H *p*-layer and bulk *i*-layer. It is well known that *p/i* interface, where the seeding layer exists, plays a crucial role in the performance of solar cells [26]. Small changes in *p/i* interface may result in significant change in the initial performance and stability of solar cells. Defects created in this region by inappropriate

processing conditions can serve as recombination centers and redistribute the internal electric field within *i*-layers, leading to inferior device performance. Therefore, great care must be taken and systematic investigation must be conducted to identify the critical issues affecting the growth of μc-Si:H *i*-layers and performance of μc-Si:H solar cells.

The seeding processes we have explored can be classified into two categories: (i) *p*-layer seeding, which refers to all seeding methods involving boron doped *p*-layer, and (ii) *i*-layer seeding referring to the nucleation methods inside the 'intrinsic' Si:H layer. For the *p*-layer seeding methods, the principle is to induce the nucleation of μc-Si:H within *p*-layer, thus the damages associated with creating nucleation sites by harsh plasma are within the dead, heavily boron-doped *p*-layer and thus of little concern. Both the *p/i* interface and the region (within *i*-layer side) near the *p/i* interface are less defective and are grown more 'smoothly'. Since no amorphous-to-microcrystalline transition layer exists within the 'active' bulk *i*-layer, better carrier collection may be obtained. For the *i*-layer seeding methods, a fast amorphous-to-microcrystalline phase transition is needed to uniformly grow the bulk *i*-layer. Conceptually, this type seeding methods take the advantages of minimized optical loss associated with the thicker, defective *p*-layers resulting from *p*-layer seeding approaches and higher Voc due to the wider bandgap of the non-microcrystalline *i*-layer near the *p/i* interface. Presumably, the disadvantage of this type seeding methods is the unavoidable defects near the *p/i* interface (*i*-layer side) created by the hydrogen rich plasma used to create nucleation sites, which might lead to poor carrier collection.

With the introduction of seeding step, rather than the simple *p-i-n* structure shown in Figure 3.2, the real μc-Si:H solar cells fabricated in this study should be more accurately described as having the following structure:

Glass/SnO_2/α-SiC:H *p*-layer/Seeding layer/Bulk μc-Si:H *i*-layer/α-Si:H *n*-layer/Al.

Depending on the seeding scheme employed, the seeding layer can be in the *p*-layer side or *i*-layer side of the *p/i* interface.

The fabrication procedure of μc-Si:H solar cells, as illustrated in Figure 3.3, mainly consists of substrate preparation, system baking and evacuation, deposition of *p-i-n* layers, defining small area devices using shadow masks, and Al sputtering.

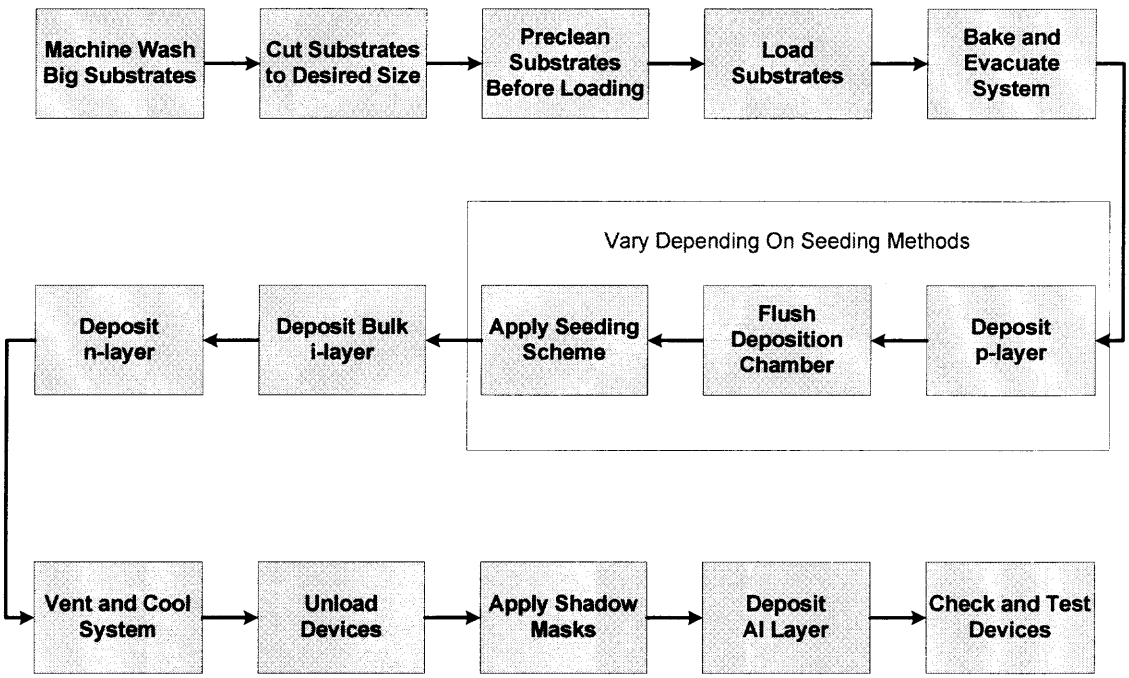

Figure 3.3 Schematic fabrication procedure of μc-Si:H solar cells.

3.4 Device Performance Test

3.4.1 Preparation of Small Area Solar Cells

The performance of μc-Si:H solar cells, including I-V characteristics, quantum efficiency, and light soaking, are routinely evaluated using small area devices defined during or after Al sputtering. The areas of the small devices are usually between 0.15 ~ 0.3 cm^2. A small area device is formed by separating an Al dot, which is surrounded by bare α-Si:H, from other Al coating. The small Al dot, which determines the size of the active solar cell under test, can be produced by applying shadow masks during Al sputtering or by etching out the Al coating surrounding the predefined dot. The Al dot serves as the negative contact and a copper wire, which is soldered to the SnO_2 by scratching away Si:H near the Al dot, serves as the positive contact.

Before performance test, all solar cells are subject to routine check using a curve tracer which not only displays the diode characteristics of solar cells, but also cures some inferior devices by burning out the shunting paths and consequently resulting in better devices. Only those good devices confirmed by curve tracer are tested. The major goal of performance test is not to simply provide performance parameters, i.e., Voc, Jsc, FF, conversion efficiency, stability, etc., it is rather to gain insights into the deposition processes by analyzing the data obtained from those tests. Parameters such as Voc, FF, and quantum efficiency can provide information, either explicitly or implicitly, regarding the issues concerned in depositing high quality μc-Si:H solar cells, e.g., effect of seeding process, microstructure of *i*-layer, quality of *p*-layer and *p/i* interface, etc.

3.4.2 Measurement of I-V Characteristics

The light intensity used for measuring I-V characteristics in this study is the standard Air Mass 1.5 (AM 1.5) spectrum which corresponds to a power of 100 mW/cm^2. The AM, equal to 1/cos(θ) with θ being the angle between the sun and the zenith, measures the atmospheric path length relative to the minimum path length when the sun is directly overhead. Thus the solar spectrum is defined as AM 0 when the sun is outside the earth's atmosphere and AM 1 when the sun is at zenith. The AM 1.5 represents the spectrum when the sun is positioned at 45° above the horizon and is used to characterize the solar-weighted average for terrestrial conditions. The value of 100 mW/cm^2 is standardized from the true solar power of 84.4 mW/cm^2 corresponding to the AM 1.5 spectrum to simplify the characterization of solar cells [11].

The I-V measurement station used in this study is schematically illustrated in Figure 3.4.

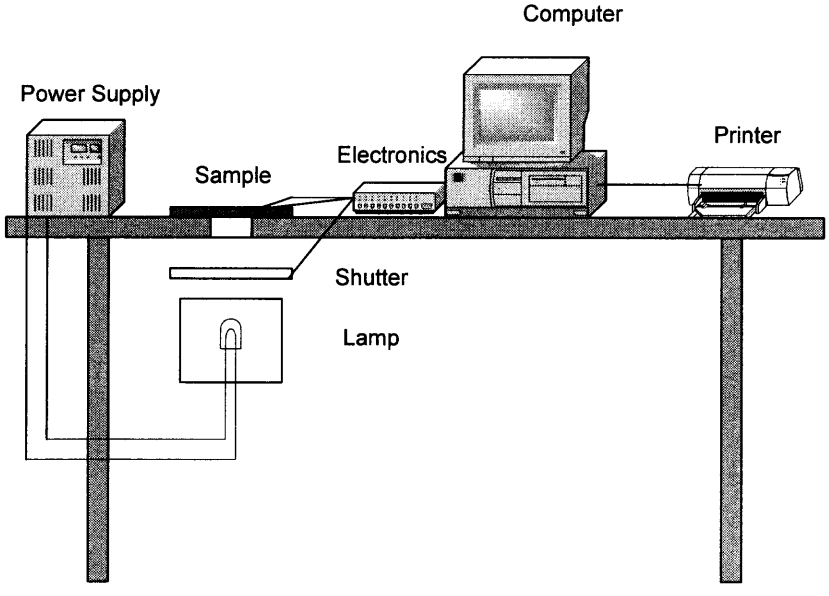

Figure 3.4 Schematic configuration of I-V measurement station.

Except for the light source and its power supply, the entire I-V measurement station, including testing, data collection, data process and output, is fully controlled by a computer through electronic circuits. The I-V measurement (AM1.5, 25 °C) always starts from stabilizing and calibrating light source so that it can simulate the AM 1.5 spectrum or, using a 'standard cell', produce same PV output as that obtained under standard AM 1.5 spectrum. An automatic shutter is used to prevent the sample from extra light exposure before and after taking I-V measurements.

The major parameters obtained from I-V characteristics have been introduced in Section 2.1.2. The conversion efficiency is defined as the ratio of the maximum output power, P_M, of the solar cell to the power of incident light, P_L. Here, P_M can be obtained form I-V characteristics using $P_M = Jsc \times Voc \times FF$ and P_L is 100 mW/cm^2 by definition. Thus, the conversion efficiency can be easily determined from I-V measurement.

Among the various parameters obtained from I-V characteristics, conversion efficiency presents the overall performance of the solar cell, fill factor (FF) provides information about carrier collection which is mainly determined by the quality of *i*-layer, and Voc is an important parameter used in this study to deduce the microstructure of *i*-layer. Generally solar cells with α-Si:H *i*-layer has a Voc of 0.75~0.8 V and μc-Si:H *i*-layer results in much lower Voc though inferior, defective *p/i* interface may be another factor which lowers Voc as well. Combining those parameters together, information about the effect of seeding process and/or the growth of bulk μc-Si:H *i*-layer on the performance and *i*-layer microstructure of Si:H solar cells can be obtained.

3.4.3 Measurement of Quantum Efficiency

Quantum efficiency is the ratio of the number of electron-hole pairs (which are produced by the incident photons) collected from the solar cell to the number of incident photons. It is also called spectral response providing the quantum efficiency is taken as a function of the wavelength of incident light. Generally, quantum efficiency is represented in a percentage and is determined using the following equation:

$$QE = \frac{S \times 1240}{\lambda} \times 100\% \tag{3.1}$$

where λ is the wavelength in nanometer (nm) and S is the radiant sensitivity in Amperes/Watt (A/W), which is the photoelectric current, divided by the incident radiant power.

Generally, spectral response of a solar cell, with either α-Si:H or μc-Si:H *i*-layer, is taken as a figure of merit because it presents the overall efficiency of generation and collection of photo-generated carriers within the *i*-layer. Furthermore, the spectrum itself can provide information pertaining to the microstructure and light absorption within solar cells. The short-wavelength part of the spectrum can be used to evaluate the *p*-layer and *p/i* interface since most short-wavelength light is absorbed in that region. The long-wavelength part, especially that near the infrared range, can be taken as a signature of *i*-layer microstructure. Due to the wide bandgap of α-Si:H (usually ~1.7 eV), solar cells with α-Si:H *i*-layers show little or even zero spectral response in the wavelength range longer than 800 nm. On the other hand, spectral response in the wavelength range of 800~1000 nm or even longer can be detected in solar cells with μc-Si:H *i*-layers since charge carriers can generated when low-energy photons strike the solar cell owing to the narrow bandgap of μc-Si:H (usually ~1.1 eV). Therefore, spectral response provides a

sensitive and handy tool to evaluate *i*-layer microstructure. In this study, red-light response (i.e., QE in wavelength longer than 800 nm) is usually used as a signature of the existence of μc-Si:H in *i*-layers.

The quantum efficiency measurement system used in this study is shown in Figure 3.5. A steady light source is fed into the monochromator to generate monochromic light which is incident to the sample in a manner of scanning from short wavelength, typically 400 nm, to long wavelength such as 800 or 1000 nm. A chopper is placed between the monochromator and sample to generate alternate signals which are fed into the lock-in amplifier used to pick up the photoelectric current generated within the solar cell. All data are eventually input into the computer and plotted as spectral response spectrum. A filter is applied at long wavelength (>560 nm) to filter out possible high-energy light from the system and ambient. The entire system is automated through GBIP interfaces and programs written using LabView. The measurement can be conducted in a dark room or using a black box to cover the optical path.

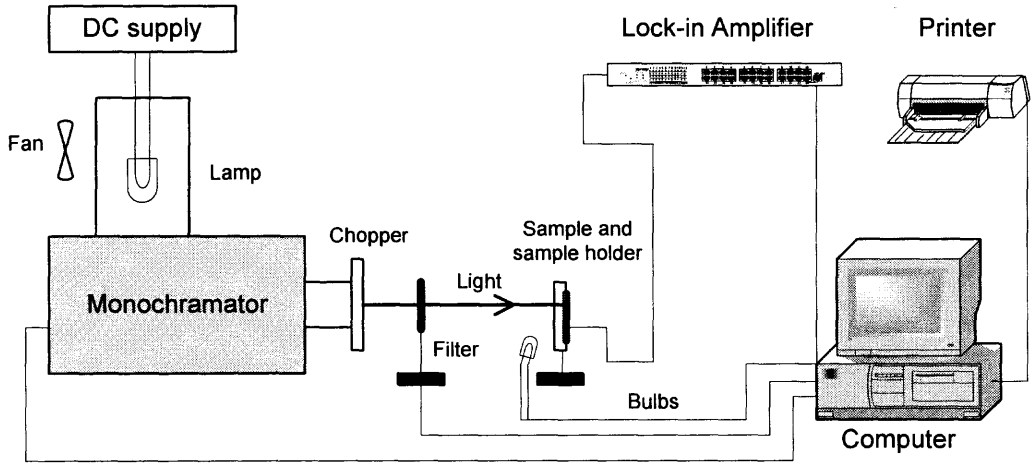

Figure 3.5 Schematics of quantum efficiency measurement system.

3.4.4 Light Soaking Test

Improving the stability of α-Si:H films and PV devices against light exposure is one of the major driving forces in developing μc-Si:H solar cells which are assumed to possess much higher resistance to light-induced degradation. The purpose of light soaking test in this study is not to explore the microscopic mechanism of light-induced degradation in α-Si:H or μc-Si:H solar cells, which is still one of the most controversial issues in the field. Instead, its main goal is to study the stability of μc-Si:H solar cells against light soaking. A wide variety of light soaking behaviors have been observed for solar cells with various *i*-layers which have different, complex microstructures and qualities depending on actual deposition sequences. Thus, light soaking can also contribute to the studies on the device fabrication processes.

Normally light soaking tests are performed with continuous conditions of open circuit, AM 1.5 at ~50 °C. For typical α-Si:H solar cells, such tests usually take a month or even longer though most degradation occurs during the beginning of the experiment. The experimental setup for the conventional light soaking, given in Figure 3.6, mainly consists of a continuous light source simulating one sun and a rotating sample station to expose the samples uniformly.

An accelerated light soaking station, with a light intensity of 47 suns, was constructed at EPV, which can take a light soaking test within hours to provide a fast evaluation (compared to hundreds of hours by the extremely time-consuming conventional light soaking). The fully automated accelerated light soaking station is schematically shown in Figure 3.7. The light intensity of 47 suns is achieved by applying

a concentration lens over the normal ELH lamp. A temperature sensor can be put atop the solar cell to read out the temperature on the sample surface.

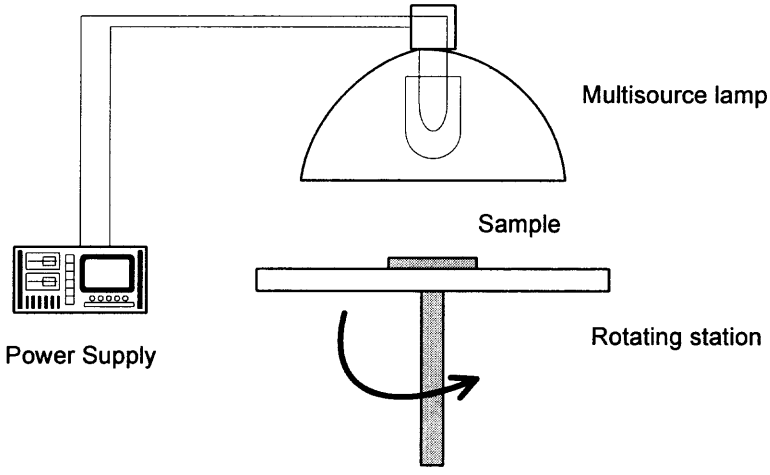

Figure 3.6 Configuration of conventional light soaking station.

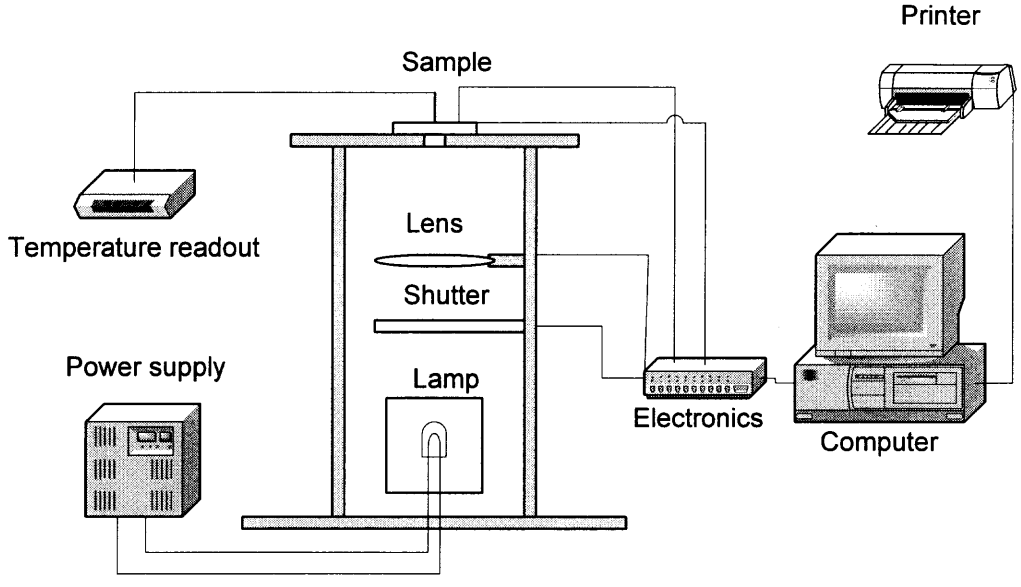

Figure 3.7 Configuration of accelerated light soaking station.

3.5 Structural Characterization of μc-Si:H Solar Cells

3.5.1 Introduction to Direct Structural Characterization of μc-Si:H Solar Cells

Structural characterization has shown that μc-Si:H is a highly complex material which can take on a variety of microstructures and exhibit very different qualities depending on the exact deposition conditions. Unlike α-Si:H, which can be grown readily on various substrates, μc-Si:H and performance of μc-Si:H based solar cells are highly affected by the nature and surface morphology of substrates, reactor geometries, as well as the processing sequences [93-96]. Generally, stand-alone films (rather than devices) deposited on special substrates (e.g., Corning 7059 glass, etc.) are used to characterize α-Si:H. In the case of μc-Si:H, however, properties obtained from stand-alone films may not be necessarily translated into the μc-Si:H *i*-layer within actual *p-i-n* device configurations. Some other issues recently revealed by our own and other groups such as the effect of accumulated bulk layer thickness on the growth of μc-Si:H, non-uniformity during μc-Si:H deposition, and narrow optimum processing windows for high quality μc-Si:H [50, 52, 85, 88], enhance the necessity of direct structural characterization of μc-Si:H solar cells, rather than stand-alone films.

Throughout the context of this study, therefore, we focus on direct structural characterization of actual μc-Si:H *p-i-n* solar cells fabricated using the R&D RF-PECVD. This approach, while takes a quick, direct evaluation of μc-Si:H solar cells and provides handy feedback to the device fabrication processes, limits the application of some experimental techniques which require special sample substrates and sample structures such as TEM, FTIR, etc. Consequently, the techniques used in this research for structural characterization of μc-Si:H solar cells mainly include Raman Spectroscopy, XRD, AFM,

and thickness measurement. Raman Spectroscopy, XRD, as well as AFM are conducted at NJIT and thickness measurement is carried out at EPV. All experiments are designed and conducted with concentration on establishing correlations among *i*-layer microstructure, device deposition processes, and device performance.

3.5.2 Raman Spectroscopy

The schematic configuration of the integrated Raman scattering system used in this study is shown in Figure 3.8. It consists of a high sensitivity CDIR 830-1024 spectrometer, a PI-ECL-830-300-FC frequency stabilized diode laser, and a RP830-65-05-FC fiber optic sampling Raman Probe. The Raman spectrometer uses a high QE, back thinned, thermo-electronically cooled FFT-CCD array to collect the Raman scattering and thus provide high performance and high sensitivity. The diode laser can provide light with a highly stabilized wavelength of 830 nm (±0.2 nm) with adjustable power up to 300 W. The fiber optic Raman probe utilizes micro-optic components for delivering the laser light to the sample and for collection of scattered light, resulting in a compact probe head that is fiber optically coupled to the laser source and spectrometer.

The schematic configurations of the Raman probe and fiber optic cable are shown in Figure 3.9 and Figure 3.10, respectively. Through the efficient use of dichroic and edge filters for separating the excitation and scattered light, the Raman probe utilizes a back scattering (θ=180°) sampling geometry which allows for easy sample alignment and provides optimum throughput because of the total overlap between the excitation and collection cones. In Figure 3.10, the two 20 gauge hookup wires are integrated into the fiber optic cable to power up the LED emission indicator which provides laser safety indication when the laser source is turned on. The collection and excitation fibers are

bundled separately within a protective jacket and the entire Raman probe head is coupled to the excitation source via optical fibers to allow remote measurement of samples with different sizes and configurations.

In this research, the Raman probe is secured on a rigid stand and the distance between the probe head and sample surface can be smoothly adjusted such that the focal spot is on the sample surface. The focal spot size is less than 1 mm so as to enable the user to pinpoint the measurement spot precisely on the sample and the coaxial design also ensures the collection and excitation spots overlap as much as possible for highest Raman signal. Such flexible design enables quick, full scale (different positions on one sample) evaluations which are critical especially when spatial non-uniformity exists.

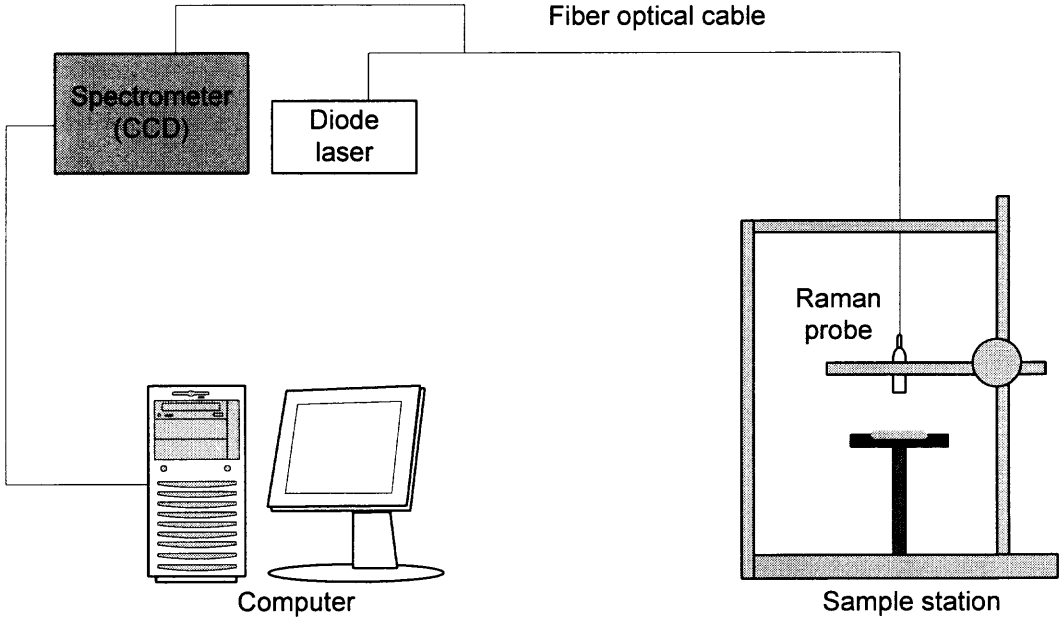

Figure 3.8 Configuration of Raman Spectroscopy.

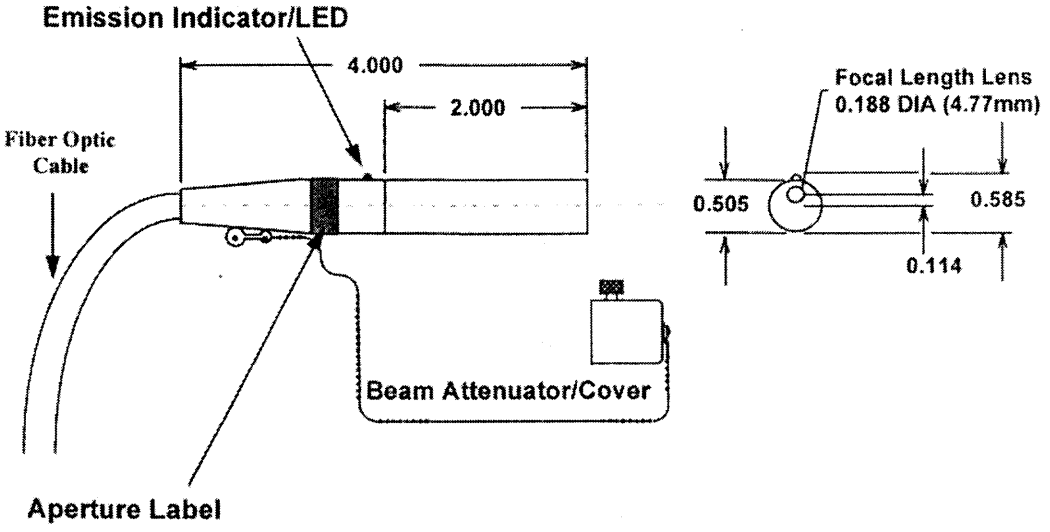

Figure 3.9 Schematic diagram of the Raman probe.

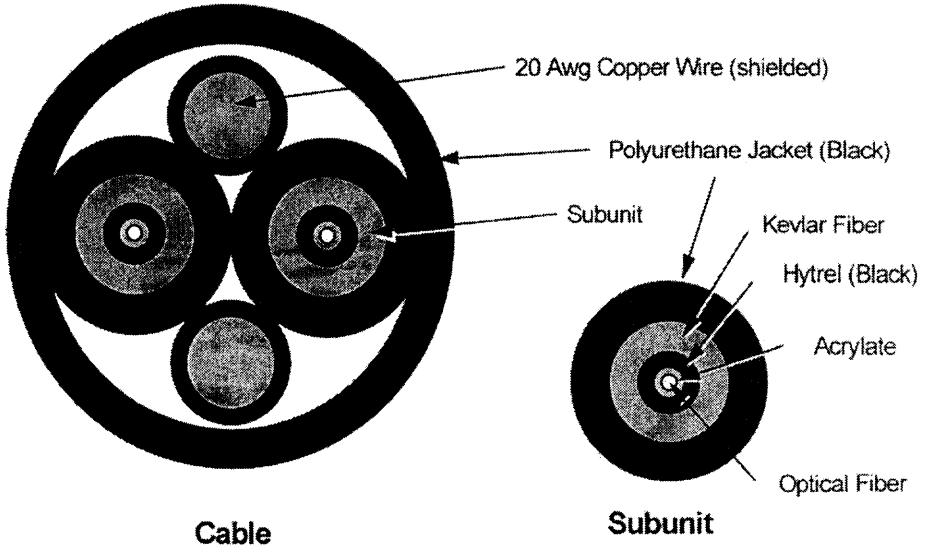

Figure 3.10 Components of the fiber optic cable.

For μc-Si:H solar cells, thick *i*-layers are needed due to its relatively low optical absorption. As revealed by recent studies, a transition from α-Si:H to μc-Si:H occurs during deposition of μc-Si:H using PECVD and thickness of the transition layer strongly depends on the plasma conditions. Thus deep penetration during Raman scattering experiment is critical to obtaining overall structural information throughout the entire thickness of the solar cell. Insufficient penetration of excitation laser will provide information of only part of the *i*-layer near the *n*-layer side and such data are prone to misinterpretation providing the *i*-layer is thick enough so that even thick amorphous or transition layer cannot be detected.

In this study, a diode laser with center wavelength of 830 nm is used so that deep penetration is readily obtained. Though μc-Si:H solar cells used in this study have *p-i-n* structures, contributions from both doped layers to the Raman scattering are small compared to that from *i*-layer since they are both Raman inactive and very thin compared to *i*-layer. However, contributions from the SnO_2 substrates are inevitable as the trade-off for deep penetration, especially when samples are thin or transparent (highly crystalline).

Typical Raman spectra show a broad peak at about 480 cm^{-1} for amorphous silicon and a sharp peak at around 520 cm^{-1} for crystalline silicon, For μc-Si:H, which is often a mixture of micro-crystallites embedded within amorphous matrix, the Raman spectra present a variety of patterns, form either one of the two peaks or both, depending on the microstructure of μc-Si:H *i*-layers.

The most common equation used to deduce the micro-crystallinity of μc-Si:H, presented as crystalline volume fraction, Xc, can be presented as the following:

$$X_c = \frac{I_c}{I_c + yI_a} \tag{3.2}$$

where, *Ic* and *Ia* are the integrated Raman scattering intensities due to the crystalline component (~520 cm^{-1}) and amorphous component (~480 cm^{-1}), respectively. *y* is the ratio of the integrated Raman cross section for c-Si to that for α-Si, and is taken as ~1 (0.88 for μc-Si:H) [97] or taken as the correction for the crystallite size *x*, with $y(x) = 0.1 + e^{-x/250}$ [98]. Another formula,

$$X_c = \frac{I_c + I_m}{I_c + I_m + \sigma I_a} \tag{3.3}$$

or its similarities, is also used by some groups to calculate the crystalline volume fraction where *Im* is a deconvoluted peak at ~510 cm^{-1} and σ is a correction factor being ~1 [99,100].

However, it has been argued that Raman scattering cannot be used to accurately calculate the average crystallite size and crystalline volume fraction without support of other data, e.g., XRD [101]. In our research, even though adjustable laser power and flexible focusing are usually applied during Raman scattering measurement, contributions from substrates and doped layers make the deconvolution of Raman spectra inconsistent among different samples. The usually mixed-phase nature of μc-Si:H *i*-layers, as revealed by our own and other groups, makes the calculated Xc further unreliable since grain boundaries may contribute to the Raman scattering pattern and intensity as well [102].

Another parameter obtained from Raman scattering spectra, *Ic/Ia*, has been used to present micro-crystallinity throughout this study and proven to be very sensitive to the overall microstructure of μc-Si:H *i*-layers. Its sensitivity to structural change enables its application in investigating the micro-crystallinity of μc-Si:H i-layers, which is critical to establishing the correlations among deposition process, device performance, and μc-Si:H *i*-layer microstructure.

3.3.3 X-Ray Diffraction

The XRD experiments are conducted using a commercial Rigaku D/MAX-B XRD system equipped with a powder diffractometer. Solar cells to be tested are cut to either about 0.5" × 0.5" or 1.4" × 2" in size. The former is used with a sample holder designed for powder sample while the latter is used directly in place of the standard sample holder. Cu *Ka* line (λ=1.5406 Å) is used as the X-Ray source. Standard θ/2θ scanning method with a 2θ scanning range from 25° to 60° is used. In view of the weak XRD signal from μc-Si:H but relatively strong background from the substrate, A 30 kV voltage and a 20 mA current are applied. The step size of 2θ scan is 0.02 and the scanning speed is usually very slow (~20 min/degree).

For μc-Si:H solar cells, XRD peaks at 2θ equal to about 28.5° and 47.4° are taken as signatures of Si (111) and Si (220) planes, respectively. Since the grain sizes of μc-Si:H are usually small, the average grain size, t, can be calculated using Scherrer Formula:

$$t = \frac{0.9\lambda}{B\cos\theta} \tag{3.5}$$

where B, presented using radiant, is the Full Width of Half Maximum (FWHM) of the XRD peak corresponding to Bragg angle θ [103]. The real microstructure of μc-Si:H, however, is generally believed to be columnar such that the grain size along the direction of grain growth may be much longer than its width, which is inconsistent with the assumptions used in obtaining Scherrer Formular. Furthermore, XRD signal from μc-Si:H solar cells is usually very weak unless the sample is highly crystalline. Low signal to noise ratio makes the determination of FWHM inaccurate and inconsistent. However, XRD still provides valuable information to confirm the micro-crystallinity and determine the orientation of μc-Si:H *i*-layers.

3.3.4 Atomic Force Microscopy

The AFM experiments are conducted using a commercial Nanoscope IIIa AFM system under tapping mode. As depicted in Figure 3.11, tapping mode AFM operates by scanning a tip attached to the end of an oscillating cantilever across the sample surface. The cantilever is oscillating at or near its resonance frequency with an amplitude typically ranging from 20 nm to 100 nm. The tip tightly "taps" on the sample surface during scanning, contacting the surface at the bottom of its swing. The feedback loop, by maintaining a constant RMS of the oscillation signal acquired by the split photodiode detector, maintains a constant oscillation amplitude. By maintaining a constant amplitude, the tip-sample interaction is maintained constant during scanning. In order to maintain a constant "setpoint" amplitude, the vertical position of the scanner is changed at each (x, y) data point. These displacements are stored in the computer to form the topographic image of a sample surface.

The surface roughness of μc-Si:H solar cells revealed by AFM is comparable to the *n*-layer thickness. Thus it could be assumed that the AFM surface morphologies of μc-Si:H solar cells are mainly determined by *i*-layer though it is covered by *n*-layer which is very thin compared to *i*-layer and usually uniformly deposited. Though non-uniform, irregular surface morphologies are usually observed in this study, good correlations among microscopic surface morphology, macroscopic non-uniformity, and micro-crystallinity of μc-Si:H solar cells are found as well.

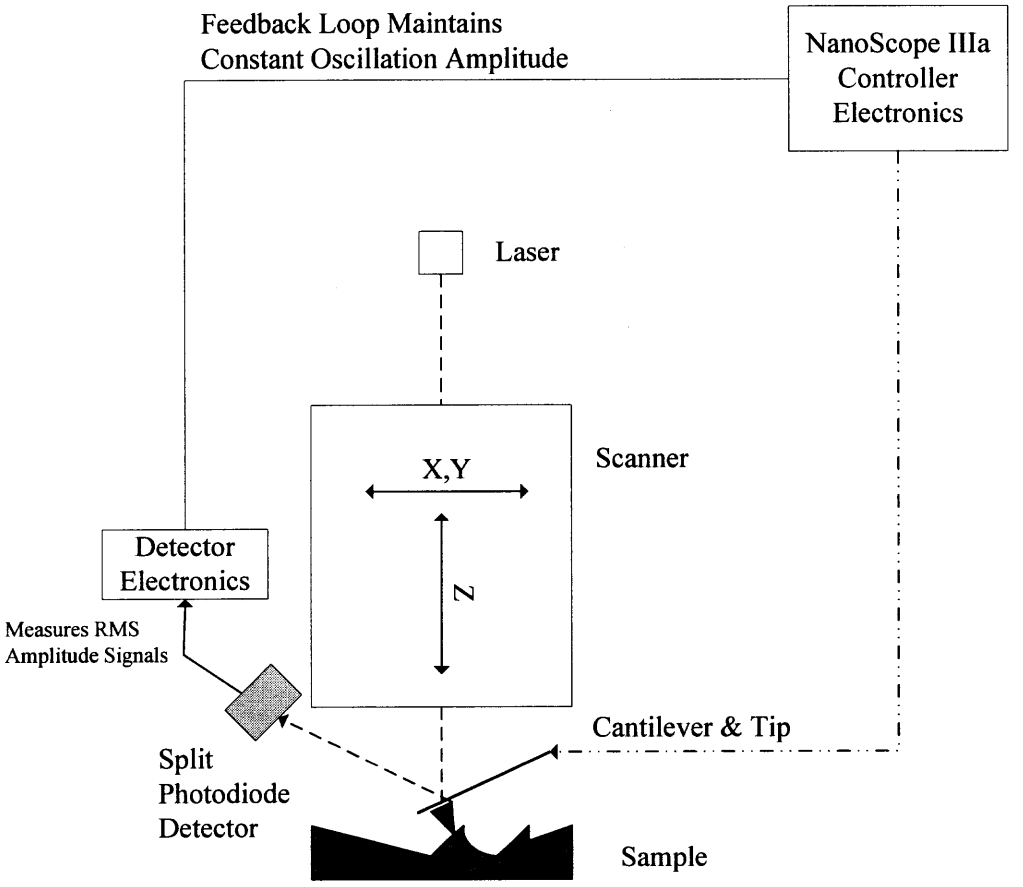

Figure 3.11 Operation principle of tapping mode AFM.

3.4.5 Thickness Measurement

Thickness measurements are performed using a commercial Dektak IIIa stylus profilometer. Step height of trenches formed by laser scribing or steps formed by etching out silicon is measured by the stylus profilometer and thickness of μc-Si:H *i*-layer is estimated by subtracting the thicknesses of doped layers which could be empirically determined from deposition conditions. The thickness measurement is usually used to determine growth rate of μc-Si:H *i*-layers, certify device performance, and provide information on spatial uniformity.

CHAPTER 4

RESULTS AND DISCUSSION

4.1 Introduction

The fabrication, performance, and structural properties of μc-Si:H solar cells are discussed in this chapter. Major topics discussed include: (i) fabrication of μc-Si:H solar cells, (ii) structural characterization, (iii) stability of μc-Si:H solar cells under light soaking, and (iv) correlations among device fabrication, performance, and structural properties.

Throughout this study, major efforts are made in exploring the deposition processes of μc-Si:H *i*-layers. Various seeding methods are applied to induce the formation of μc-Si:H on α-Si:H or α-SiC:H underlayers and to obtain high quality μc-Si:H *i*-layers. Device performance obtained from routine test, including I-V characteristics, QE, and light soaking, are correlated to μc-Si:H *i*-layer deposition processes and used to deduce *i*-layer microstructure. The importance of the initial nucleation step (seeding methods) in determining the growth and properties of μc-Si:H *i*-layers, as well as device performance are recognized and discussed as the main topic in the section of fabrication of μc-Si:H solar cells.

Direct structural characterization of actual μc-Si:H solar cells, rather than stand-alone μc-Si:H films, are carried out using Raman scattering, XRD, and AFM. Micro-crystallinity obtained from Raman scattering, presented using *Ic/Ia*, proved to be sensitive to the micro-crystallinity and microstructure change of μc-Si:H *i*-layers. Various *i*-layer microstructures, including amorphous, mixed-phase, and highly crystalline,

are revealed in solar cells deposited using various seeding processes and bulk *i*-layer deposition conditions. By means of structural characterization, non-uniformity over large substrates, in terms of *i*-layer microstructure and device performance, is identified and used to study the correlations among device performance, deposition conditions, and microstructural properties of μc-Si:H *i*-layers.

Stability of μc-Si:H solar cells against light exposure is studied by light soaking experiment. A wide variety of light soaking behaviors are observed from solar cells with *i*-layers showing different micro-crystallinity. Under either conventional or accelerated light soaking, solar cells with truly μc-Si:H *i*-layers exhibit excellent stability.

Though understandings on the microscopic mechanisms of μc-Si:H growth and its effect on the performance of μc-Si:H solar cells are hindered by the complexities of μc-Si:H resulting from harsh deposition conditions, correlations among μc-Si:H *i*-layer deposition, microstructure, and device performance are observed and summarized in the final section of this chapter. A narrow optimum processing window for high quality μc-Si:H is identified, which presents a critical challenge in developing high performance μc-Si:H solar cells.

4.2 General Characteristics of α-Si:H and μc-Si:H Solar Cells

A number of single junction, *p-i-n* α-Si:H solar cells are deposited on SnO_2 coated glass superstrates to verify the performance of the newly constructed RF-PECVD system. These solar cells are deposited using relatively "standard" recipes used everywhere to obtain high quality α-Si:H PV devices, e.g., low hydrogen to silane dilution ratio, moderate pressure, low plasma power, low substrate temperature (below 200 °C), etc.

Though higher deposition rates can be obtained, deposition rates of ~ 1 Å/s are used to produce high quality, stable α-Si:H solar cells. Under such deposition conditions, good thickness and device performance uniformity is generally maintained. Fill factors (FF) at ~0.7 or higher are considered as a signature of good devices. Those α-Si:H solar cells usually show conversion efficiencies in the range of 7% ~ 8% and Voc in the range of 0.75 ~ 0.8 V.

These α-Si:H solar cells provide references to the μc-Si:H solar cells fabricated thereafter. Compared to α-Si:H solar cells, solar cells with μc-Si:H *i*-layers generally exhibit lower Voc due to the lower bandgap of μc-Si:H. Two solar cells, one with α-Si:H *i*-layer and the other with μc-Si:H *i*-layer, are compared in Table 4.1. The corresponding I-V characteristics are shown in Figure 4.1.

Figure 4.1 shows the I-V characteristics of a "perfect" α-Si:H solar cells along with that of a "fairly well" μc-Si:H solar cell. In ideal case, the μc-Si:H *i*-layer should be made much thicker than its amorphous counterpart due to its low light absorption and light trapping schemes should also be employed such that higher current density can be obtained and conversion efficiency of μc-Si:H solar cells can be improved.

Table 4.1 Comparison of α-Si:H and μc-Si:H Solar Cells

Sample	Device Type	Voc (V)	Jsc (mA/cm^2)	FF (%)	Efficiency (%)
R30-3	α-Si:H	0.78	13.7	66	7.0
R48-1	μc-Si:H	0.51	13.3	57	3.8

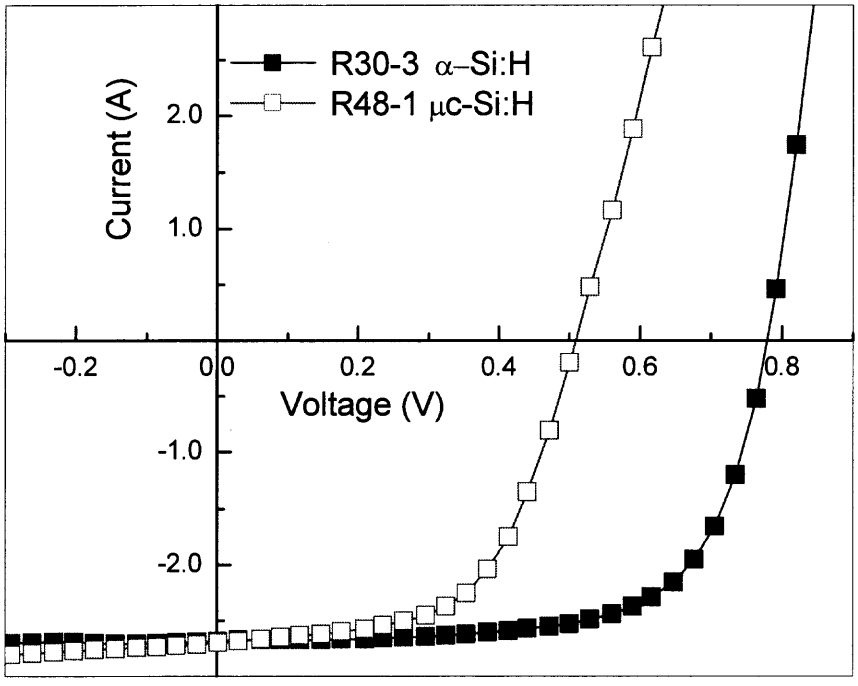

Figure 4.1 I-V characteristics of α-Si:H and μc-Si:H solar cells.

Spectral response, i.e., QE versus wavelength, is usually measured to verify the overall carrier collection of solar cells. It turns out that QE also provides a sensitive tool in detecting the existence of μc-Si:H within *i*-layers. As shown in Figure 4.2, α-Si:H solar cells show little or even zero QE when the wavelength of incident light is longer than 800 nm. For μc-Si:H solar cells, spectral response is observed in the wavelength range from 800 to 1000 nm or even longer due to the low bandgap of μc-Si:H. Though Voc can also be taken as the signature of μc-Si:H *i*-layers, misinterpretation may occur since low Voc may result from highly defective *p/i* interface or inferior α-Si:H *i*-layer. In another case where structural evolution from α-Si:H to μc-Si:H or mixed-phase Si:H occurs within *i*-layer, high Voc as that of normal α-Si:H solar cells may be obtained despite the

existence of μc-Si:H in part of the *i*-layer. In this study, existence of small fraction of μc-Si:H within solar cells with high Voc at 0.78 V has been clearly detected by QE measurement. Therefore, combination of Voc and red-light response (QE at wavelength 800 nm or longer) provides a signature of μc-Si:H which leads to less possibility of misinterpretation.

The red-light response of μc-Si:H solar cell shown in Figure 4.2 is relatively low, mainly due to the simplicity of the solar cell used in this study. Low light absorption of μc-Si:H, combined with the lack of effective light trapping by rear reflectors (only a layer of Al is used), leading to low QE in the long wavelength part of the QE spectrum.

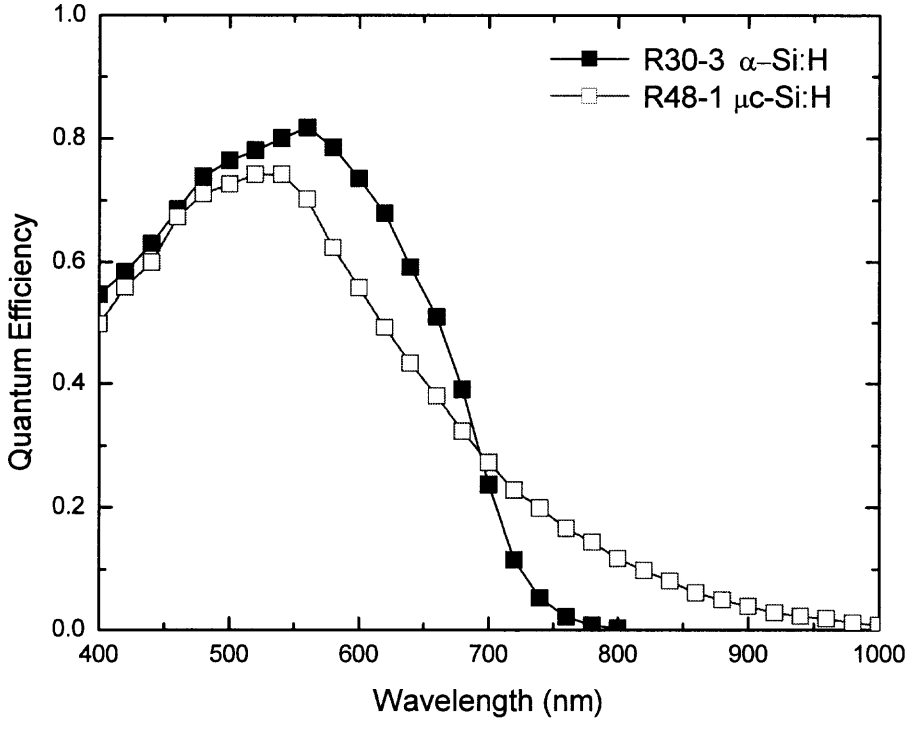

Figure 4.2 QE spectra of α-Si:H and μc-Si:H solar cells.

4.3 Fabrication of μc-Si:H Solar Cells

4.3.1 Seeding Methods Used for μc-Si:H *i*-layer Deposition

To grow μc-Si:H on an α-Si:H or α-SiC:H under-layer, a transition layer exists at or near the *p/i* interface which may make that region highly defective and affect carrier generation and collection by reducing *i*-layer optical absorption and/or weakening the internal electrical field over *i*-layer. Therefore, reducing the transition layer thickness, i.e., fast and intensive nucleation, is conceptually beneficial to obtaining uniform, high crystalline μc-Si:H *i*-layers and thus improves the overall device performance. To limit the transition layer thickness, highly hydrogen rich plasma conditions can be applied to induce initial μc-Si:H nucleation followed by growth of bulk μc-Si:H *i*-layer under relatively softer plasma conditions. However, the hydrogen rich plasma used in seeding processes could do severe damages to the microstructure and performance of μc-Si:H solar cells. Furthermore, the seeding process and bulk *i*-layer growth interplay with each other given the *i*-layer thickness is usually less than 2 μm (typical thickness for single junction α-Si:H solar cell is only about 0.5 μm or less). Those issues form the major difficulties in obtaining and reproducing high performance μc-Si:H solar cells.

In this study, therefore, seeding methods are widely explored in terms of their effects on the growth of μc-Si:H *i*-layers and performance of μc-Si:H solar cells. Depending on the position where the seeding methods being applied, they can be classified into two categories:

(i) *i*-layer seeding, which refers to the nucleation methods within the intrinsic layer side of the *p/i* interface; and

(ii) *p*-layer seeding referring to all seeding methods involving boron doped *p*-layer.

These two types of seeding methods can also be combined to form more complicated but potentially more rewarding seeding processes, however, we prefer to simplify the seeding approaches such that the critical issues can be identified with less influential factors. The *p*-layer seeding approaches take the advantage of limiting the damages associated with energetic seeding plasma within the PV non-active *p*-layer and consequently leading to better overall carrier collection. However, concerns about cross contamination in single chamber system resulting from dopants arise when the deposition time of *p*-layer is inevitably much longer providing *p*-layer seeding is applied. Though highly defective transition layer within *i*-layer resulting from *i*-layer seeding approaches can do a lot damages to the performance of μc-Si:H solar cells, the *i*-layer seeding methods do not generate such contamination concerns and are relatively more suitable for single chamber systems as that we use in this study. A thin α-Si:H buffer layer is usually deposited before applying *i*-layer seeding schemes which could be helpful in boosting the Voc owing to its wider bandgap compared to that of μc-Si:H.

The *i*-layer seeding processes explored in this study generally consist of the following steps: deposition of a thin α-Si:H buffer layer, incubation layer deposited using either pure hydrogen plasma etching on the buffer layer or seeding using plasma with very high hydrogen to silane dilution ratio, and then silane grading-in steps, followed by the deposition of bulk *i*-layer with lower hydrogen dilution ratio. Similarly, the *p*-layer seeding methods consist of the following steps: deposition of initial boron doped α-SiC:H *p*-layer, incubation layer produced by pure hydrogen plasma etching, μc-SiC:H or μc-Si:H *p*-layer deposition, followed by μc-Si:H *i*-layer growth.

4.3.2 Effect of Seeding Methods on the Growth of μc-Si:H

High hydrogen to silane dilution ratio has been widely recognized as the most important factor to induce and sustain the growth of μc-Si:H. Therefore, hydrogen to silane dilution ratio, $R = [H_2]/[SiH_4]$, is used as the major parameter in analyzing the seeding processes. Table 4.2 lists the Voc and red-light response (QE at 800 nm) of several samples deposited using different seeding methods. All samples are deposited in the area close to the gas exhaust of the deposition chamber where silane is more easily depleted and growth of μc-Si:H is more favorable compared with areas near the gas inlet. In Table 4.2, the R used during seeding processes and deposition of bulk *i*-layers are listed separately in two columns to distinguish their contributions to the growth of μc-Si:H. Voc and QE under 800 nm excitation are taken as the signatures of μc-Si:H. Sample R18-1 and R23-3 are deposited without any seeding steps, only high hydrogen dilution ratio (compared to that used in α-Si:H deposition) is applied during *i*-layer deposition. All other samples are deposited using *i*-layer seeding methods. For sample R27-3 and R32-3, a thin α-Si:H buffer layer is deposited over α-SiC:H *p*-layer, then pure hydrogen plasma etching is applied to induce the nucleation of μc-Si:H, followed by the deposition of bulk *i*-layer. For sample R33-3, R36-1, R41-3, R43-3, and R63-1, extremely high hydrogen dilution ratio are used during seeding steps, followed by the deposition of bulk *i*-layers with lower hydrogen dilution ratios.

Table 4.2 Effect of Seeding Methods on the Deposition of μc-Si:H

Sample	R (Seeding)	R (*i*-Bulk)	Voc (V)	QE (%) at 800 nm	Seeding Method
R18-1		159	0.78	0.6	No
R23-3		70	0.72	0	
R27-3	Pure H_2	35	0.74	0	H_2 plasma etching on α-Si:H buffer layer
R32-3	Pure H_2	100	0.62	0.6	
R33-3	300	100	0.67	1.1	High R seeding over α-Si:H buffer layer
R36-1	989	250	0.51	3.8	
R41-3	200	200	0.74	0	
R43-3	854	200	0.61	3	
R63-1	875	159	0.53	0.9	

Existence of μc-Si:H within *i*-layers are deduced by combining Voc and red-light response. Results from sample R18-1, R23-3, R27-3, and R32-3 show that hydrogen dilution ratio during deposition of bulk *i*-layers, R (*i*-bulk), plays an important role in sustaining the growth of μc-Si:H. With bulk *i*-layers deposited under relatively low hydrogen dilution ratio, R23-3 and R27-3 are confirmed being α-Si:H by I-V characteristics and QE spectra though they show lower Voc than that of normal α-Si:H solar cells. On the other hand, R18-1 and R32-3 show signature of μc-Si:H with bulk *i*-layers deposited under higher hydrogen dilution ratio. Comparing R18-1 and R32-3, it is also observed that pure hydrogen plasma etching does help the growth of μc-Si:H.

From I-V characteristics and QE spectra, R32-3 looks more crystalline than R 18-1 even though its bulk *i*-layer is deposited with hydrogen dilution ratio lower than that for R18-1.

With assistance of seeding approaches, existence of μc-Si:H is observed in the *i*-layers of R33-3, R36-1, R41-3, R43-3, and R63-1. Except for the hydrogen dilution ratios used in seeding approaches, most of the plasma conditions used to deposit these samples are similar (only seeding layer and bulk *i*-layer of R33-3 are deposited under relatively lower chamber pressure compared to other samples). With the general consensus that nucleation of μc-Si:H is mainly induced by high hydrogen flux inside the plasma, it can be assumed that the differences of *i*-layer microstructures are strongly depending on the seeding steps. The Voc and red-light response of these samples are plotted against the hydrogen dilution ratios used in seeding steps in Figure 4.3 and Figure 4.4, respectively. The linear fit for each data set is also plotted in these two figures. The red-light response data include both QE measured without bias and those measured under negative bias (-3 V). Since R33-3 is deposited under lower chamber pressure, highly energetic ions may exist within the plasma and make the *i*-layer rather defective than that of the other four samples. Its red-light response under negative bias is weak (but still improved) and cannot be obtained under -3 V bias.

The data in these two figures are rather scattered, however, overall tendencies still can be observed. Generally, Voc decreases and red-light response increases along with increasing R (Seeding). It can be interpreted as the hint of increasing micro-crystallinity associated with enhanced nucleation steps. Due to the energetic plasma conditions and relatively complicated deposition sequences, microstructure of μc-Si:H *i*-layers might be very complicated and defective. Thus, many factors may affect the device performance

parameters including Voc and red-light response. A rather sharp Voc drop for R36-1 is observed in Figure 4.3. Correspondingly, R36-1 also shows red-light response less than expected. This is probably because the seeding process for R36-1 is more hydrogen rich and energetic (the plasma power used is comparable to that for R33-3, R43-3, and R63-1 but higher than that for R41-3) compared to that for other samples. Such plasma conditions create more deep level defects and result in low Voc as well as poor carrier collection. Same tendency is observed for R33-3 because of its lower deposition pressure which may result in high-energy ion bombardment on the growing μc-Si:H surface.

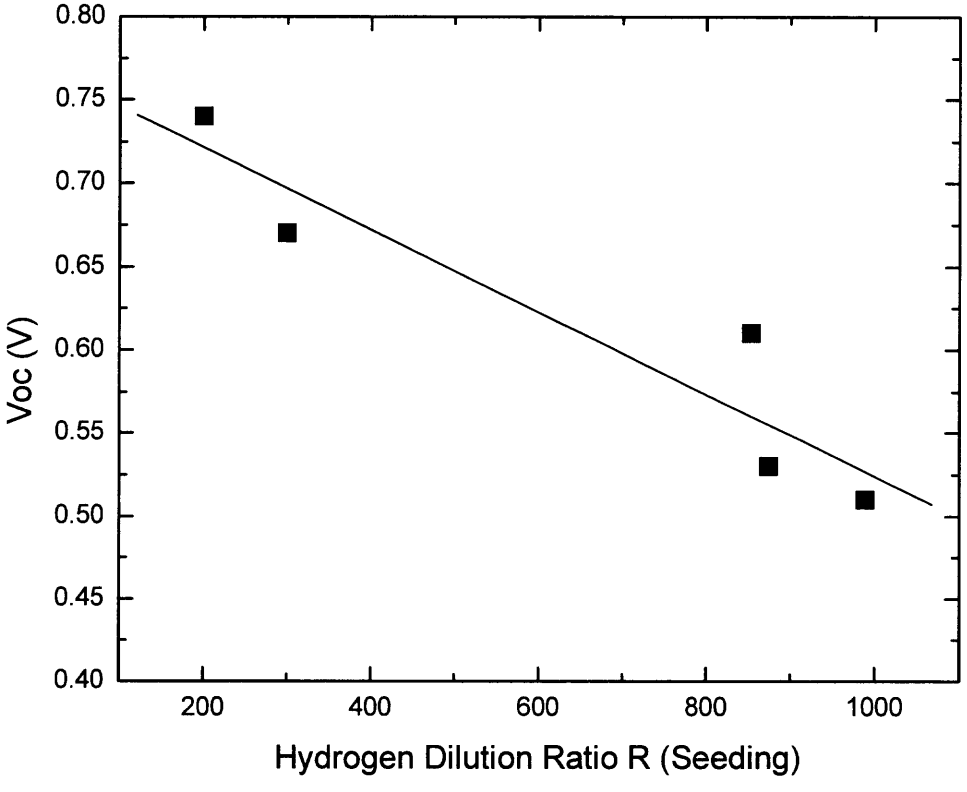

Figure 4.3 Open circuit voltage of μc-Si:H solar cells as a function of hydrogen dilution ratio used during *i*-layer seeding.

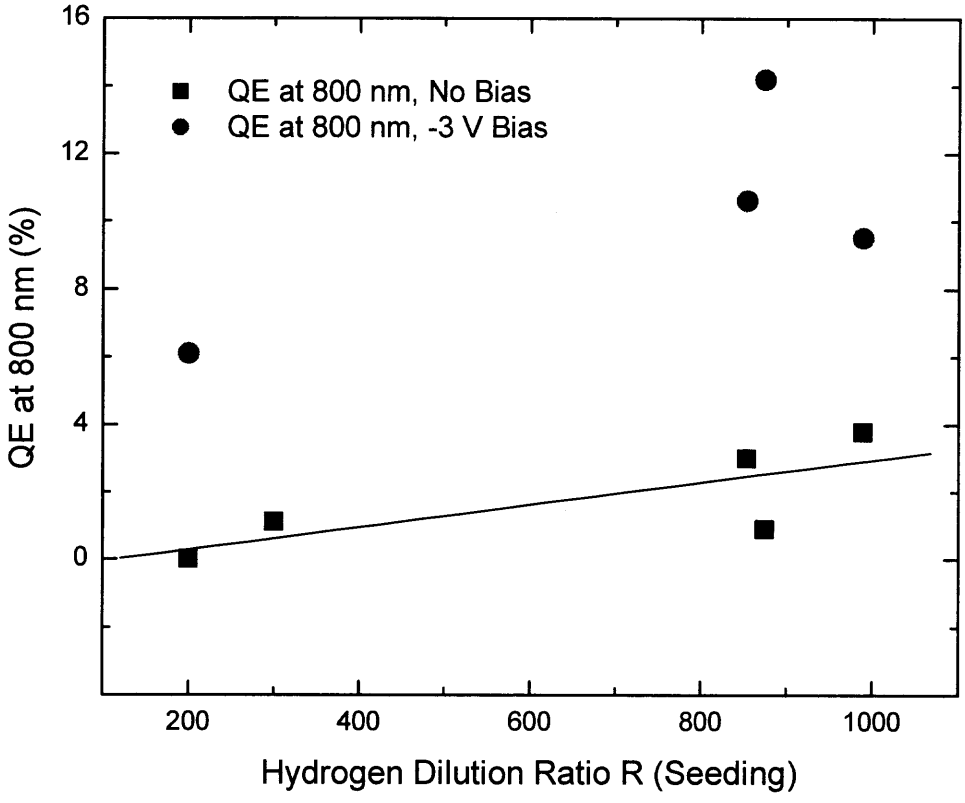

Figure 4.4 Red-light response of μc-Si:H solar cells as a function of hydrogen dilution ratio used during *i*-layer seeding.

Under -3 V bias, the red-light response for all samples are significantly increased, which means that collection of μc-Si:H related photo-generated carriers is enhanced under strengthened internal electrical field over the *i*-layer. Since the mobility of holes is much lower than that of electrons, most of the lost photo-generated carriers without negative bias are probably generated near the back side (*n*-layer side) of the *i*-layers. Unlike the red-light response which increases with increasing R (Seeding), the difference between red-light response with and without negative bias is relatively constant except

for R63-1. This indicates that, for these samples, μc-Si:H has been grown at least in the backside of the *i*-layers.

It is also interesting to note that R41-3, as well as R18-1, show Voc comparable to that of typical α-Si:H solar cells even though the existence of μc-Si:H within *i*-layers is confirmed by QE measurement. As shown in Figure 4.5, which plots the QE spectra of R41-3 measured under both zero bias and negative bias, the entire QE spectrum, especially in long wavelength range, is significantly increased when negative bias are applied. Even slight negative bias, e.g., -1 V bias, can produce obvious QE improvement. This observation, i.e., high Voc, low red-light response without bias, and much improved red-light response with negative bias, can be explained by the effects of seeding processes employed in these two runs. Compared to other μc-Si:H samples listed in Table 4.2, the plasma conditions of the seeding processes used in these two runs are rather 'softer' such that the initial nucleation steps are less effective. Therefore the transition from α-Si:H to μc-Si:H occurs far away from the *p/i* interface/α-Si:H buffer layer and the part of *i*-layers near *p/i* interface is dominant by α-Si:H, leading to high Voc comparable to that of typical α-Si:H silicon cells. However, transitions eventually occur at some point as the *i*-layer grows thick enough and μc-Si:H is grown within *i*-layer in the *n*-layer side, which is responsible for the red-light-generated carriers collected only under strong internal electrical field (negative bias). This explanation is consistent with the observation in Figure 4.4 as well. With enhanced seeding approach, transition from α-Si:H to μc-Si:H occurs near *p/i* interface, leading to lower Voc owing to the reduced bandgap of such mixed-phase Si:H. The μc-Si:H grown close to *p*-layer generates electron-hole pairs upon long wavelength light shining which could be collected providing the holes are swept into

the *p*-layer. Thus the red-light spectral response can be improved without negative bias but the carriers generated by μc-Si:H near *n*-layer side stay uncollected as shown in Figure 4.4. The *i*-layer microstructure evolution deduced from device performance is consistent with those models obtained from μc-Si:H films deposited on c-Si substrates [87] though actual device deposition sequences and commercial grade substrates severely delay the nucleation and growth of μc-Si:H.

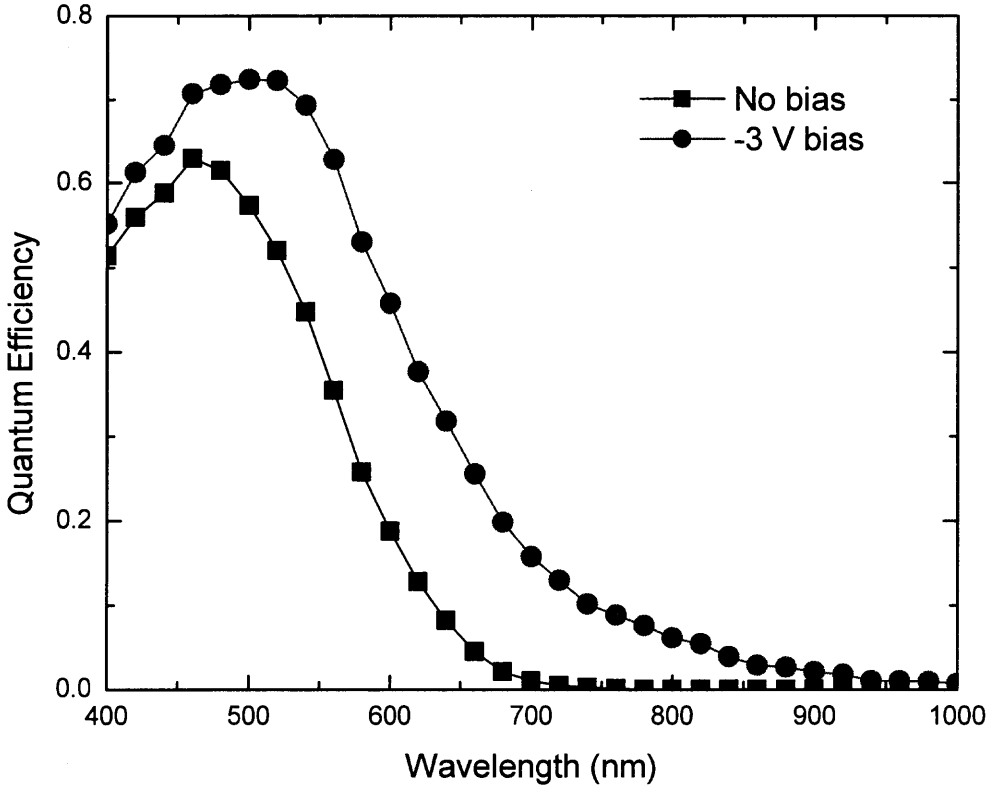

Figure 4.5 QE spectra of μc-Si:H solar cells with high Voc.

Briefly summarizing above discussion, the effect of seeding processes on the growth of μc-Si:H in the case of *i*-layer seeding can be deduced as the following:

- Without effective seeding step, *i*-layer can be grown staying amorphous even if it is deposited under high hydrogen dilution.
- High hydrogen to silane dilution ratio in the plasma can induce μc-Si:H nucleation and sustain μc-Si:H growth. Seeding processes with very high hydrogen dilution ratio can effectively enhance nucleation and growth of μc-Si:H.
- A transition from α-Si:H to μc-Si:H occurs inside the *i*-layer when seeding approaches are applied. The starting position of this transition, and possibly its thickness as well, depend on the seeding procedures applied.
- Less effective seeding results in slow α-Si:H to μc-Si:H transition which leads to high Voc and low red-light response.
- Seeding approaches using highly hydrogen rich plasma can induce fast α-Si:H to μc-Si:H transition, leading to low Voc and higher red-light response.

Most of the seeding processes explored in this study are even complicated than those listed in Table 4.2. In addition to the involvement of pure hydrogen etching or seeding using very high hydrogen dilution, the nucleation steps are generally followed by the grading-in of silane so as to sustain a smooth μc-Si:H growth and obtain high micro-crystallinity. As expected, those seeding procedures always induce the growth of μc-Si:H confirmed by Voc and red-light response. Similar to above discussion, lower Voc is expected in the case of *p*-layer seeding due to continuous growth of μc-Si:H over the *p/i* interface and *i*-layer. This has been confirmed by our experiments.

Compensations, however, must be made between growing highly crystalline μc-Si:H *i*-layers and obtaining high device performance when hydrogen rich, energetic plasma is considered of being beneficial to the growth of μc-Si:H. Such plasma conditions also create a lot defects and may severely reduce the carrier collection and overall device performance.

The critical importance of seeding processes, therefore, is not simply to induce μc-Si:H growth because, even without seeding methods, deposition of μc-Si:H can be eventually achieved using highly hydrogen rich plasma. In stead, seeding processes, combined with bulk *i*-layer deposition, are also critical to grow μc-Si:H *i*-layers with as less as possible damages to their PV related properties and consequently obtain high performance μc-Si:H solar cells. Issues related to the performance of μc-Si:H solar cells deposited employing different seeding methods will be discussed in the following section.

4.3.3 Effect of Seeding Methods on the Performance of μc-Si:H Solar Cells

Device performance of μc-Si:H solar cells is significantly affected by seeding types and plasma conditions used in respective seeding methods. The aforementioned conceptual advantages and disadvantages of *i*-layer and *p*-layer seeding types, i.e., higher Voc but poor carrier collection for *i*-layer seeding methods and lower Voc but better carrier collection for *p*-layer seeding methods, are observed throughout this study. Plasma conditions used in both seeding approaches and bulk *i*-layers, with focus on seeding approaches, such as plasma power, hydrogen dilution ratio, seeding time are varied over a wide range to study the effects of seeding methods on the performance of μc-Si:H solar cells.

For *i*-layer seeding methods, though various approaches are applied to induce fast nucleation and limit transition layer thickness, μc-Si:H *i*-layers deposited using this type seeding are defective and poor carrier collection is usually observed. While the highest conversion efficiency obtained so far from *i*-layer seeding methods is about 4%, most devices have efficiencies much lower than 3% featured by extremely low fill factor and short circuit current density. However, these bad solar cells clearly contain μc-Si:H in their *i*-layers as confirmed by I-V characteristics and QE spectra. As shown in Figure 4.6, the existence of μc-Si:H and poor carrier collection can be clearly observed from the QE spectra of such inferior μc-Si:H solar cells deposited using *i*-layer seeding methods. Without negative bias, very low spectral response is observed but which can be significantly improved under -3 V bias. It appears that collection of photo-generated carriers is highly suppressed by the defects within μc-Si:H *i*-layer created inevitably by the harsh, hydrogen rich plasma used in *i*-layer seeding. Thus advantages of *i*-layer seeding are by far outweighed by its disadvantages.

When using *p*-layer seeding methods, damages associated with creating nucleation sites by highly etching plasma are limited within the photovoltaic non-active, heavily boron doped *p*-layer and thus of little concern. Since the amorphous-to-crystalline transition mainly occur inside *p*-layer, the integrity of the critical *p/i* interface and uniformity in the growth direction of bulk μc-Si:H *i*-layer can be much improved, leading to higher fill factor and better overall carrier collection. In this study, conversion efficiencies of ~5% have been achieved using this type seeding methods. As an example, the I-V characteristics of such a μc-Si:H solar cell is shown in Figure 4.7.

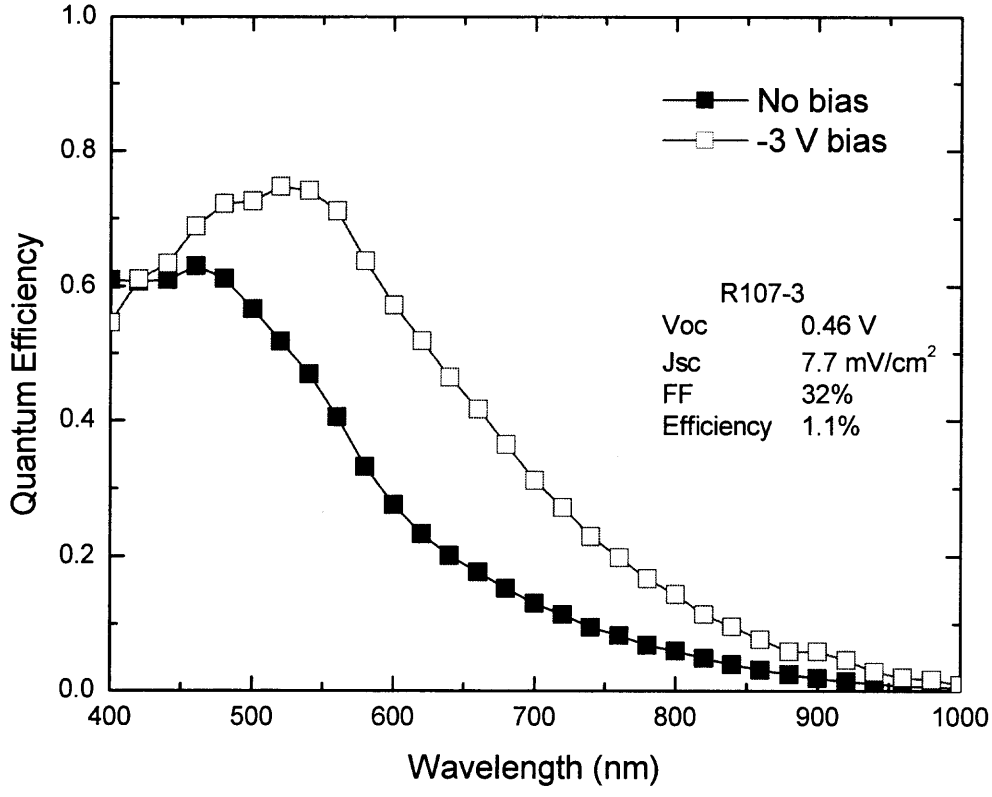

Figure 4.6 Spectral response of inferior μc-Si:H solar cells deposited using *i*-layer seeding.

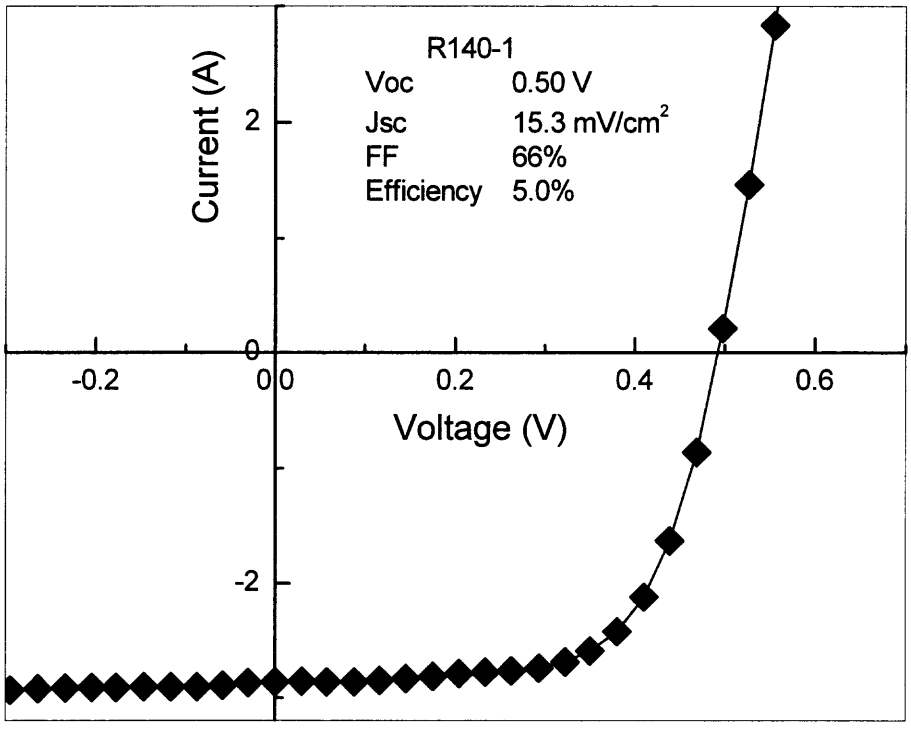

Figure 4.7 I-V characteristics of a μc-Si:H solar cell deposited by *p*-layer seeding.

Device performance parameters and seeding methods used for some μc-Si:H solar cells are listed in Table 4.3. Different performance characteristics for μc-Si:H solar cells deposited using these two types of seeding methods can be observed. Generally, μc-Si:H solar cells deposited using *i*-layer seeding methods show lower conversion efficiency featuring higher Voc but lower FF (always lower than 60%). Using *p*-layer seeding methods, higher conversion efficiencies are obtained due to very good fill factors.

Table 4.3 Performance Parameters of Selected μc-Si:H Solar Cells

Sample	Voc (V)	Jsc (mA/cm2)	FF (%)	Efficiency (%)	Seeding Methods
R48-1	0.51	13.3	57	3.8	High hydrogen dilution *i*-layer seeding over thin α-Si:H buffer layer
R60-1	0.60	13.5	52	4.2	
R69-3	0.51	13.4	45	3.1	
R138-1	0.60	14.8	46	4.0	
R139-1	0.51	14.2	48	3.5	
R141-1	0.53	15.0	45	3.6	
R130-1	0.48	14.1	54	3.9	*p*-layer seeding by etching α-SiC:H *p*-layer
R140-1	0.50	15.3	66	5.0	*p*-layer seeding by depositing μc-Si:H *p*-layer over α-SiC:H *p*-layer
R142-1	0.48	14.4	67	4.6	
R144-1	0.48	13.6	62	4.0	
R145-3	0.49	12.3	68	4.1	*p*-layer seeding by depositing μc-SiC:H *p*-layer over α-SiC:H *p*-layer
R147-1	0.48	16.2	64	5.0	

Among various *p*-layer seeding methods, etching α-SiC:H *p*-layer using pure hydrogen plasma is usually sufficient to induce growth of μc-Si:H *i*-layer. However, the fill factor and overall efficiency obtained from etching α-SiC:H *p*-layer alone (sample R1301 in Table 4.3) are usually lower than that in the case of using μc-SiC:H *p*-layer or μc-Si:H *p*-layer. Using *p*-layer seeding methods usually causes optical loss due to the resulting thicker and defective *p*-layers, as shown in Figure 4.8. With comparable Jsc, these μc-Si:H solar cells deposited using different seeding methods show different spectral response characteristics. Compared to *p*-layer seeding, *i*-layer seeding methods result in lower efficiency, but high blue-light response, i.e., higher QE at short wavelength is observed owing to its undisturbed *p*-layer which is more transparent and less defective. Due to increased *p*-layer thickness, and perhaps damages resulting from *p*-layer seeding as well, e.g., reduction of SnO_2 near TCO-*p*-layer interface, optical loss in the short wavelength range is evident in Figure 4.8. Even among *p*-layer seeding category, increased *p*-layer thickness (i.e., μc-SiC:H or μc-Si:H p-layer versus p-layer seeding by etching α-SiC:H p-layer alone), also causes more optical loss in short wavelength range.

It is also evident from Figure 4.8 that the red-light response of these μc-Si:H solar cells has been limited by the simple device structure, i.e., no rear light trapping enhancement. It has been reported that efficiencies of α-Si:H/α-SiGe:H tandem solar cells can be increased by ~15% by replacing Al rear contact with a ZnO/Al contact [32]. Higher conversion efficiencies and spectral response, especially in the red-light range, could be significantly improved providing rear light trapping schemes, e.g., good rear reflector such as ZnO/Ag back contact, and special substrate, e.g., Asahi type U SnO_2, are employed.

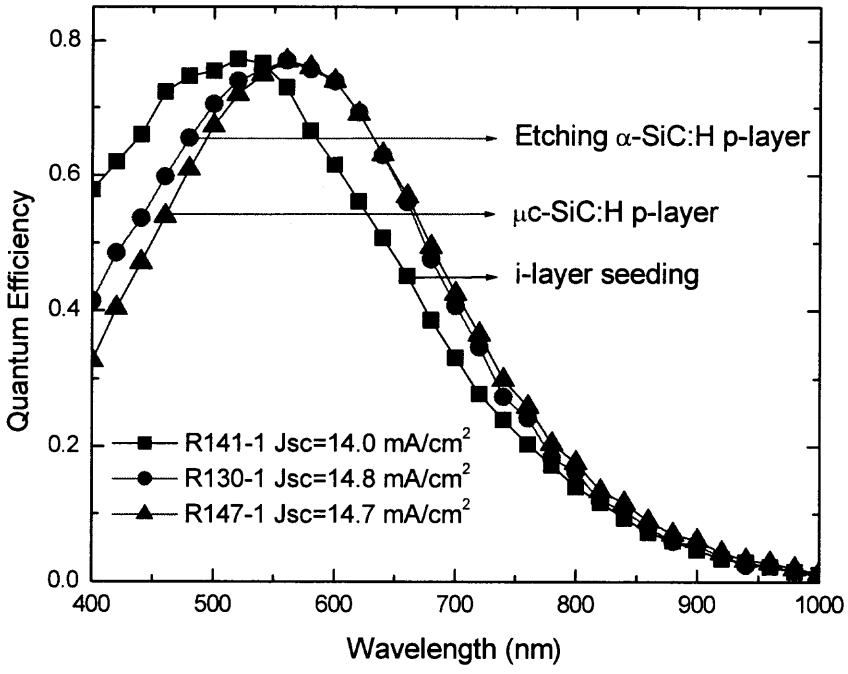

Figure 4.8 Effect of seeding methods on the spectral response of μc-Si:H solar cells.

Besides the aforementioned characteristics, μc-Si:H solar cells deposited using different seeding methods also show different QE dependence on negative bias and stability against light-induced degradation. Figure 4.9 illustrates the comparison of QE dependence, presented as the ratio of QE measured under -3 V bias to that measured under zero bias, between μc-Si:H solar cells deposited by these two type seeding methods. Even though μc-Si:H solar cells deposited by *i*-layer seeding show red-light response under -3 V bias comparable to that of μc-Si:H solar cells produced by *p*-layer seeding, their red-light response is suppressed without negative bias, obviously by much more defects inside *i*-layers introduced by *i*-layer seeding. Similar damages may have been made inside *p*-layer by *p*-layer seeding methods, their effects on photo-generated carrier

collection are minimized. Throughout this study, it is constantly observed that μc-Si:H solar cells deposited using *i*-layer seeding methods show strong QE dependence, especially in red-light range, on negative bias while those deposited using *p*-layer seeding methods show very little such dependence.

Compared to μc-Si:H solar cells produced by *i*-layer seeding methods, those produced by *p*-layer seeding exhibit better stability against light-induced degradation, which will be discussed in Section 4.5.1. In brief, it is demonstrated that *p*-layer seeding methods are preferable to *i*-layer seeding by limiting damages introduced by harsh, highly hydrogen rich plasma conditions used during seeding steps inside *p*-layers. Both initial and stabilized efficiencies are consequently improved by uniform, smooth growth of μc-Si:H across *p/i* interface and by reducing defects inside μc-Si:H *i*-layer.

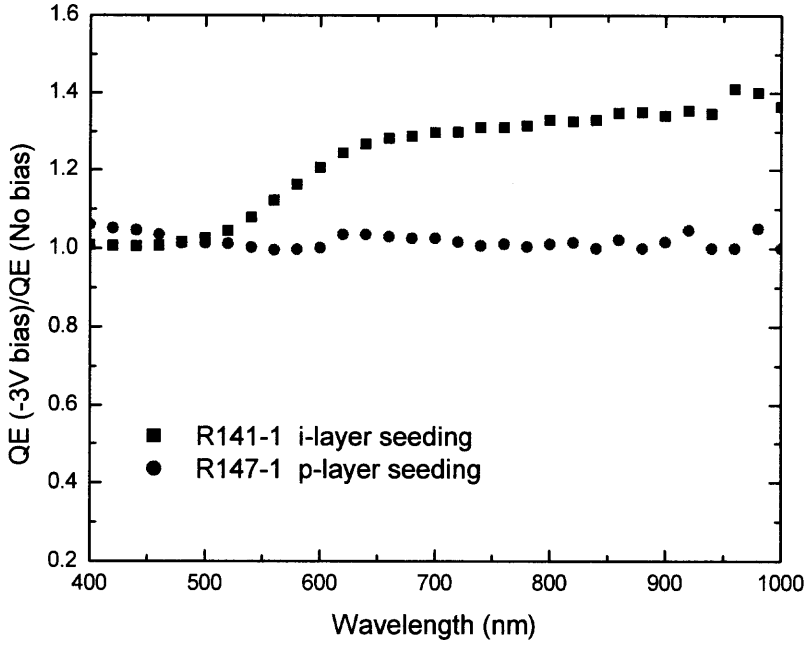

Figure 4.9 QE dependence of μc-Si:H solar cells deposited using different seeding methods.

4.4 Structural Characterization of μc-Si:H Solar Cells

As one of the few groups who highly recognize the dependence of μc-Si:H growth on under-layers and substrates as well as deposition sequences, we focus all device characterization, for both electrical and structural properties, on real devices which leads to less inconsistency between device performance and structural properties [52, 85]. Direct structural characterization not only provides general structural properties, but also further extends the relationships between seeding methods and device performance, as discussed in the previous section, to *i*-layer microstructures, and is thus capable of providing valuable insight into actual device deposition processes.

4.4.1 Raman Spectroscopy

Compared to *i*-layer, both *p*- and *n*-layers are very thin and generate little Raman response. Thus the Raman spectra measured on μc-Si:H solar cells are mainly determined by *i*-layer microstructure. Unlike α-Si:H which generally shows a broad Raman scattering peak at around 480 cm^{-1}, μc-Si:H deposited in this study exhibit a wide variety of Raman spectra depending on *i*-layer microstructure. For highly crystalline μc-Si:H *i*-layer, a sharp peak at around 520 cm^{-1}, similar with that measured from single crystalline silicon sample, is observed. Both the 480 and 520 cm^{-1} peaks, representing the amorphous and crystalline constituents of Raman scattering respectively, can coexist in the Raman spectrum when the *i*-layer is mixed-phase (α + μc)-Si:H. When the *i*-layer takes on a microstructure with little fraction of μc-Si:H crystallites embedded in α-Si:H matrix, only a slight shoulder appears at around 520 cm^{-1}. All these patterns, in reference to that of typical α-Si:H solar cell, are illustrated in Figure 4.10.

When the *i*-layer is very thin or highly crystalline, unavoidable contributions come from the SnO_2 coated plain glass substrates. Such contributions are not consistent from sample to sample and even from position to position in same sample due to widely varied properties of μc-Si:H materials. As mentioned in Chapter 3, rather than deducting crystalline volume fraction, the micro-crystallinity of μc-Si:H *i*-layer is presented in terms of the ratio of peak intensities (*Ic/Ia*) of Raman shift corresponding to μc-Si:H (*Ic*) and α-Si:H (*Ia*) constituents of the materials, respectively. The *Ic/Ia* values listed in the subfigures of Figure 4.10 clearly quantitate the corresponding overall micro-crystallinity qualitatively revealed by the patterns of Raman spectra.

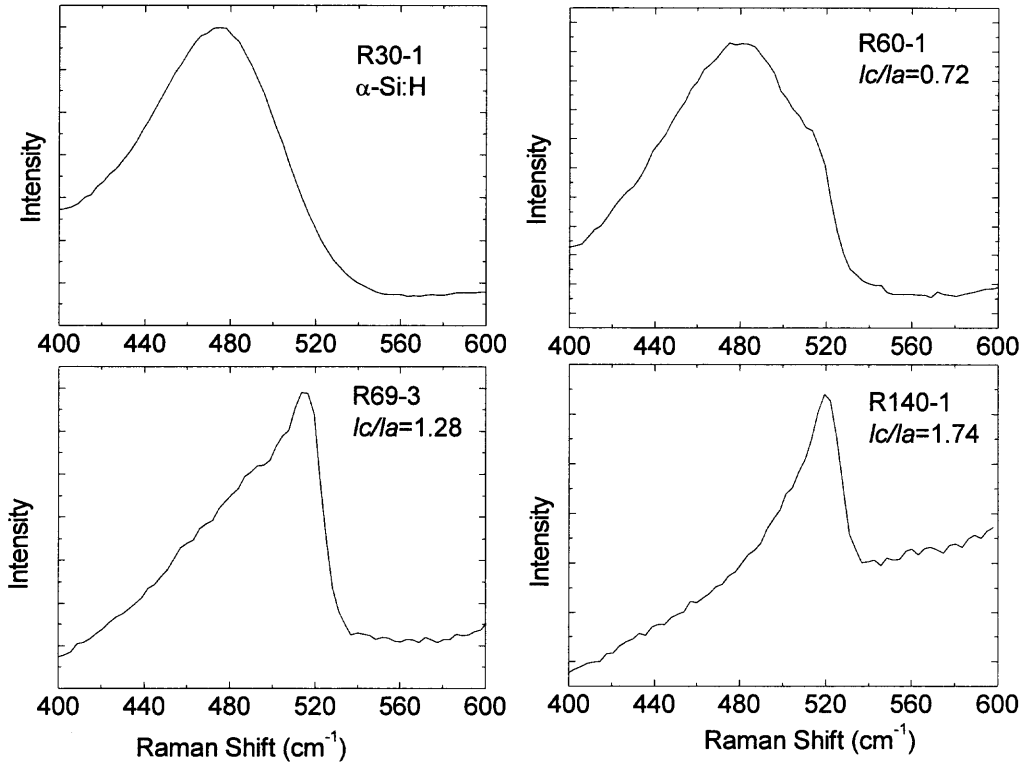

Figure 4.10 Raman spectra of solar cells with various *i*-layers.

Table 4.4 lists the micro-crystallinity obtained from Raman spectra, i.e., *Ic/Ia*, Voc, efficiency, red-light response, and light-induced degradation of sample R60-1, R69-3, and R140-1, respectively. The light-induced degradations are obtained after light soaking under conditions of AM 1.5 and 50 °C for over 800 hours. The micro-crystallinity obtained from Raman scattering coincides with I-V characteristics very well. For μc-Si:H solar cells with high *Ic/Ia*, low Voc and strong red-light response are observed while higher Voc and lower red-light response are obtained in μc-Si:H solar cells with less micro-crystallinity. For solar cell with mixed-phase *i*-layer dominant by α-Si:H (R60-1), higher initial efficiency is obtained, however, severe light-induced degradation occurs after long term light exposure. As the mixed-phase *i*-layer is dominant by μc-Si:H (R69-3), much lower light-induced degradation is observed. For highly crystalline μc-Si:H solar cell (R140-1), almost no light-induced degradation occurs.

Confirmed by device performance and deposition conditions, micro-crystallinity, as presented using *Ic/Ia*, is very sensitive to *i*-layer microstructure change and provides an easy, straightforward measure to study the correlations among *i*-layer microstructure and other properties of μc-Si:H solar cells.

Table 4.4 Micro-crystallinity and Device Performance of μc-Si:H Solar Cells

Sample	*Ic/Ia*	Voc (V)	Initial Efficiency (%)	QE (%) At 800 nm	Light-Induced Degradation (%)
R60-1	0.72	0.60	4.2	4.5	49.9
R69-3	1.28	0.51	3.1	8.7	15.4
R140-1	1.74	0.49	4.6	14.0	2.7

4.4.2 Non-uniformity of μc-Si:H Solar Cells

Unlike α-Si:H solar cells deposited using the same RF-PECVD system which always have very good uniformity over the 12" × 15" substrate, μc-Si:H solar cells usually exhibit strong spatial non-uniformity in all aspects including surface texture, thickness, *i*-layer microstructure, and device performance. The microstructure and thickness non-uniformity patterns can even be easily detected by visual check. Looking through the *p*-layer side, areas with α-Si:H or mixed-phase Si:H *i*-layer appear dark red and areas with μc-Si:H *i*-layer show light red or orange colors. Within areas with similar microstructure, the viusal color becomes lighter when the thickness decreases. Similar structural non-uniformity over very small substrates (10 cm × 10 cm) has also been reported by other group [50].

The non-uniformity features in our study are mainly resulting from the gas flow pattern inside the reaction chamber which leads to non-uniform hydrogen dilution profile across the substrates under high plasma excitation. Seeding methods, and probably bulk *i*-layer deposition as well, certainly play crucial roles in the spatial uniformity of *i*-layer microstructure and device performance. Generally, the uniformity tends to get worse with increasing growth rate (adjusted by plasma power) and silane depletion. It has been demonstrated that the non-uniformity patterns in micro-crystallinity are unambiguously accompanied by strong variation in device performance over the substrates.

Usually two types of non-uniformity can be observed in terms of thickness and micro-crystallinity depending on the seeding methods and *i*-layer deposition conditions. The first type features a gradual decrease in thickness from the gas inlet side to the gas exhaust side over the substrates. In addition to thickness change, difference in surface

appearance can be observed in the second type. A highly hazy patch with milky color appears in the part close to gas inlet side while the area apart from the patch shows dull, specular look. The shape and position of such patches are schematically shown in Figure 4.11.

The Raman scattering setup used in this study enables small area measurement (focal spot size < 1 mm^2) so that microstructure change over various positions can be identified rather precisely. It has been demonstrated that Raman scattering, by presenting micro-crystallinity using *Ic/Ia*, is very sensitive to the microstructure change. Some of the Raman spectra measured over R130-1, which shows the patch illustrated in Figure 4.11, are shown in Figure 4.12. Unsurprisingly, strong variations in micro-crystallinity, as well as corresponding device performance over the substrate, are observed in Figure 4.13. While leading to difficulties in making large-area, uniform μc-Si:H solar cells, such non-uniformity indeed provides us opportunities to study the relationships between *i*-layer microstructure and device performance.

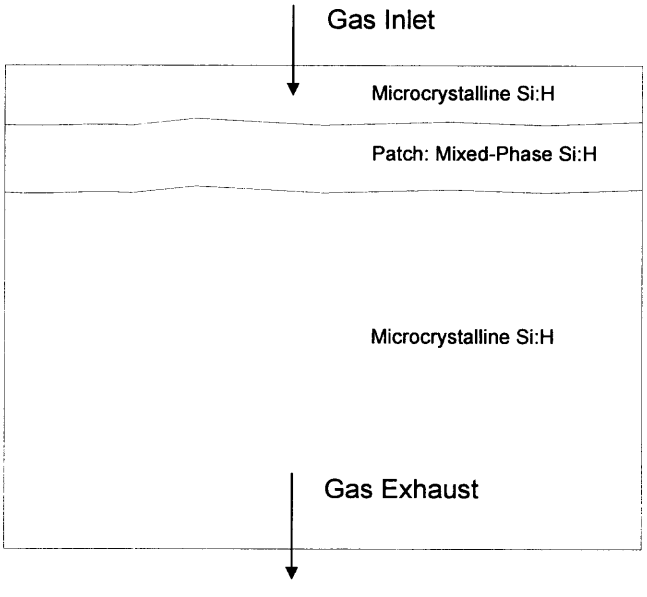

Figure 4.11 Schematic non-uniformity pattern over entire substrate.

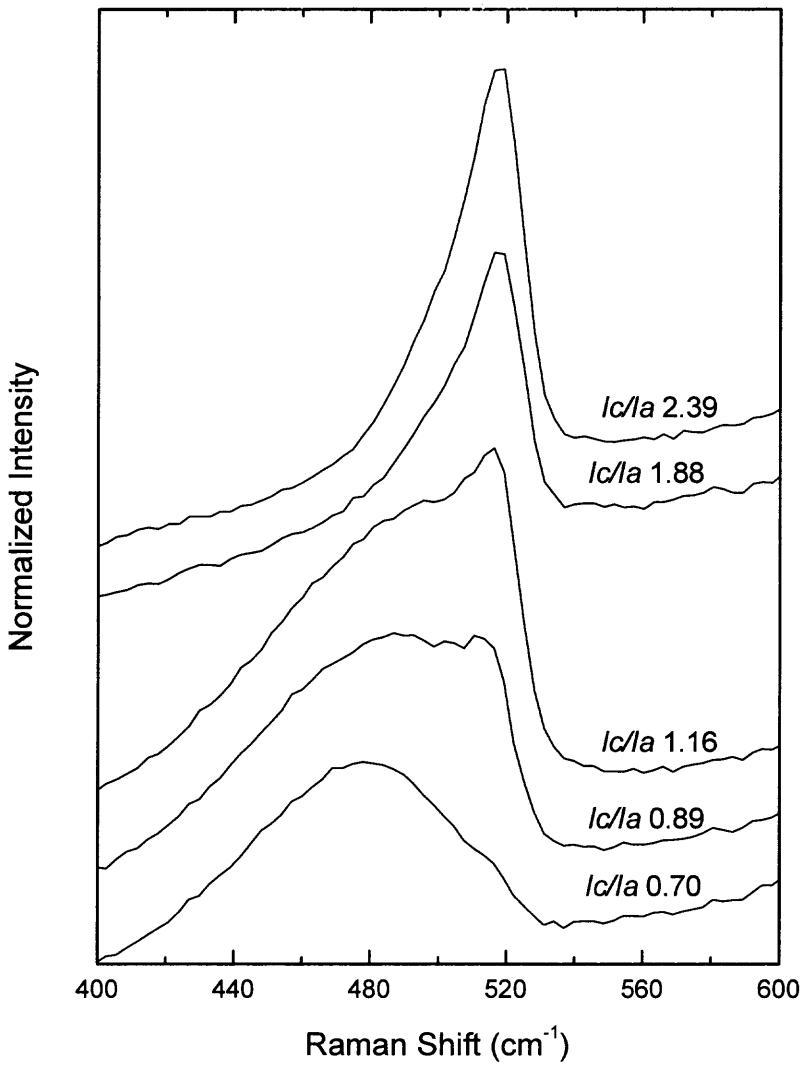

Figure 4.12 Raman spectra corresponding to non-uniformity of R130-1.

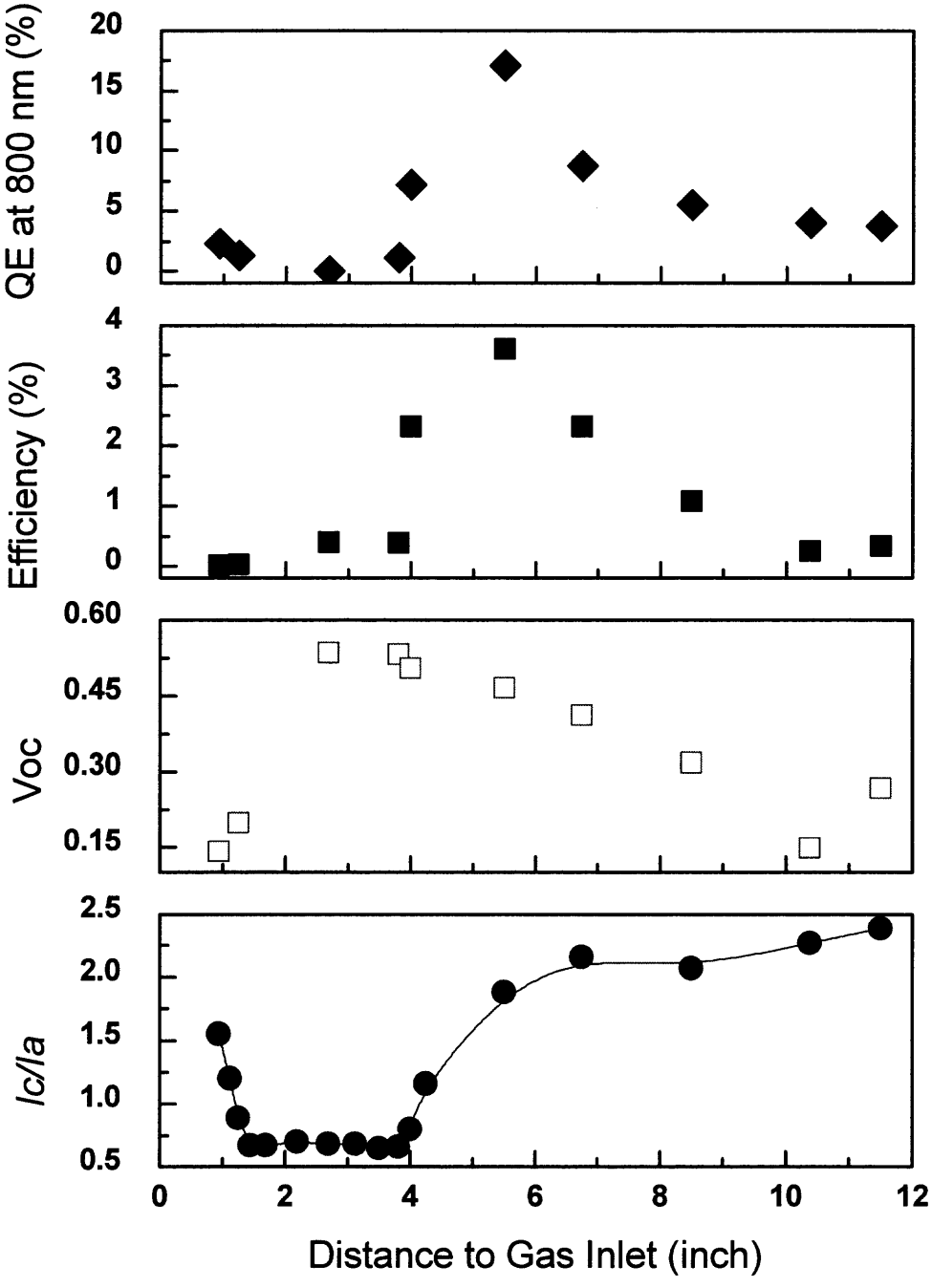

Figure 4.13 Non-uniformity in micro-crystallinity and performance of μc-Si:H solar cells as a function of position on the substrate.

The sensitivity of *Ic/Ia* to *i*-layer microstructure change can be clearly observed by identifying an mixed-phase Si:H area in Figure 4.13 which precisely corresponds to the patch depicted in Figure 4.11. The other regions on the plate show much higher micro-crystallinity. The non-uniformity exists mainly along with the gas flow direction and good uniformity is usually obtained on the other direction. Sharp changes, in both micro-crystallinity and device performance, occur at the two edges of the patch where strong phase transitions are revealed by Raman scattering. Similar results are also confirmed by measurements conducted with other samples. As pointed out in previous discussion, solar cells with mixed-phase Si:H *i*-layers (inside the patch in this case) show higher Voc compared to that with μc-Si:H *i*-layers. However, best red-light response and overall conversion efficiency are obtained from solar cells made on the high crystalline region, yet close to the edge of microcrystalline to mixed-phase transition. Moderate Voc is always obtained from solar cells made from this 'optimum' edge.

In the area near gas exhaust, even higher micro-crystallinity than that in the 'optimum' region, i.e., the μc-Si:H to mixed-phase Si:H transition edge, is obtained. However, solar cells made from this area, as well as those made from region near the gas inlet, show very low Voc, low red-light response, and low conversion efficiencies, which is contrary to the assumption that highly crystalline μc-Si:H *i*-layers will generate more carriers at long wavelength light excitation and lead to strong red-light response. When the red-light QE and Jsc of these solar cells measured without bias and that measured under -3 bias are plotted as functions of position as that in Figure 4.14 and Figure 4.15, it is clearly demonstrated that the extremely low initial device performance are mainly caused by the suppression of carrier collection.

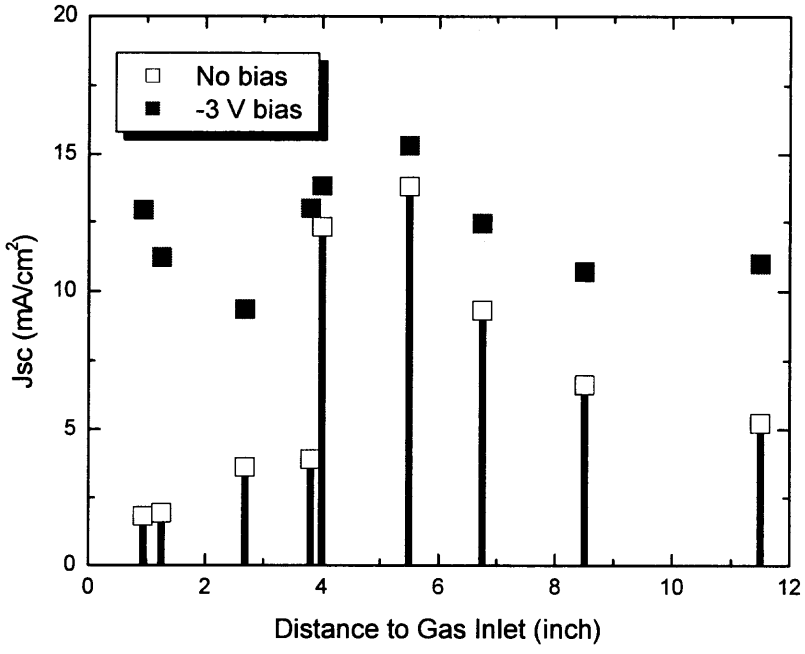

Figure 4.14 Change of short circuit current density under negative bias.

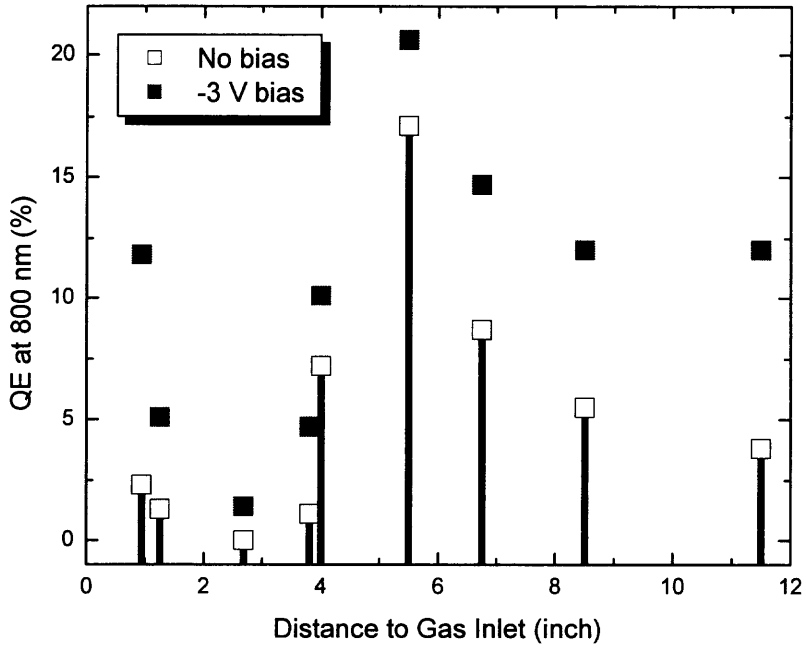

Figure 4.15 Change of red-light response under negative bias.

The drop lines in these two figures are visual guide. Under negative bias, Jsc of most solar cells, except for those devices made from the 'optimum' μc-Si:H to mixed-phase Si:H transition edge, are significantly improved, leading to comparable short circuit current densities across almost entire substrate. Similar tendency is observed in the change of red-light response with exemption of solar cells with mixed-phase Si:H *i*-layers which show low red-light response in both cases. It is evident that carrier collection is highly suppressed in both highly crystalline and mixed-phase Si:H areas. While it could be easily speculated that such suppression in highly crystalline area might be resulting from defects created by highly silane depleted plasma, the suppression of carrier collection observed in the mixed-phase Si:H area, where the concentration of Si precursors (i.e., SiHx species) is supposed to be high enough to sustain the growth of mixed-phase Si:H, cannot be straightforwardly related to defects creation by hydrogen rich plasma. Indeed, non-uniform distribution of SiHx species, complicated seeding approaches, and plasma conditions during bulk *i*-layer deposition may all play important roles in the formation of spatial non-uniformity of *i*-layer microstructure and device performance. Answers to how they are formed and how they affect the device performance of solar cells with very different *i*-layer micro-crystallinity remain unclear. In particular, any speculations on why higher crystalline μc-Si:H results in inferior device performance compared to the optimal 'edge' μc-Si:H are lacking solid support from experimental findings though basic understandings on it are sorely needed.

4.4.3 X-Ray Diffraction

The XRD spectra of μc-Si:H solar cells made from sample R140-1 are shown in Figure 4.16. XRD peaks at 2θ around 28.5°, 47.4°, and 56.2° are taken as signatures of Si (111), Si (220), and Si (311) planes, respectively. For most samples, Si (111) peaks are always very weak, if not undetectable. Compared to Raman scattering, XRD is less sensitive to the existence of μc-Si:H in the form of mixed-phase Si:H. No Si peaks are detected even though weak signal at 520 cm^{-1}, i.e., a slight shoulder, can be seen in corresponding Raman spectra.

The XRD measurement provides more information on the microstructure such as crystal plane orientation and grain sizes. The average grain sizes of μc-Si:H *i*-layers can been roughly calculated using Scherrer Formula. Once again, contributions from the substrates become an issue. It is clearly illustrated in Figure 4.16 that peaks from SnO_2 (110), (101), (200), (211), and (220) planes are much stronger than the aforementioned Si peaks. Even very slow scan speed is always adopted, the signal to noise ratios for Si peaks are still very low, which makes it extremely hard to consistently fit the XRD curve. Therefore, the grain sizes calculated form XRD spectra can only be used to roughly compare material microstructures.

Different crystallographic texture, i.e., preferential crystal growth orientation can be clearly revealed in Figure 4.16. In order to illustrate the relations among *i*-layer micro-crystallinity, device performance, and the crystallographic texture as well as grain sizes of R140-1, which has a non-uniformity pattern similar with that shown in Figure 4.11, these properties are plotted against sample position over the substrate in Figure 4.17, Figure 4.18, and Figure 4.19, respectively. The grain sizes are calculated from Si (111)

and Si (220) peaks respectively using Scherrer Formula. Under normal geometrical conditions of θ-2θ scan, only those planes parallel to the sample surface will contribute to constructive interference. Therefore, the preferential orientation, i.e., the preferential piling up direction of the crystal planes during μc-Si:H growth, is presented by the peak intensity ratio of Si (220) and Si (111), denoted as $I_{(220)}$, and $I_{(111)}$, respectively.

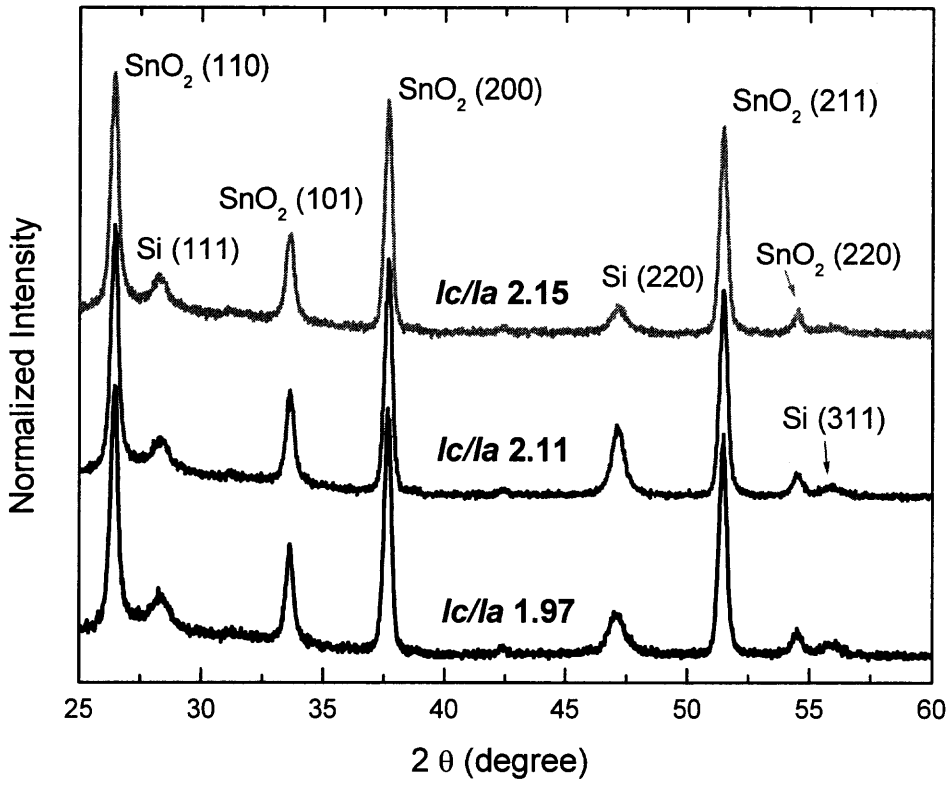

Figure 4.16 XRD spectra of μc-Si:H solar cells made from R140-1.

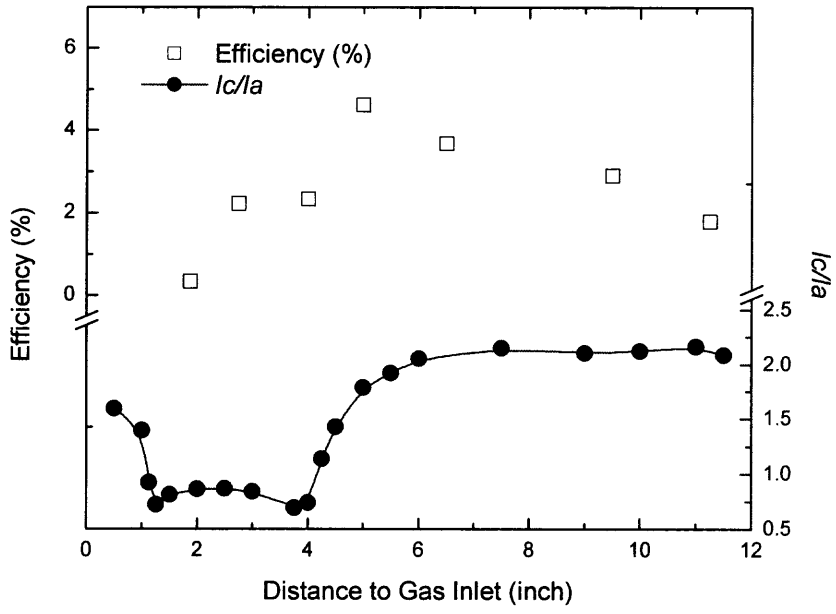

Figure 4.17 Micro-crystallinity and device performance of R140-1 as functions of position.

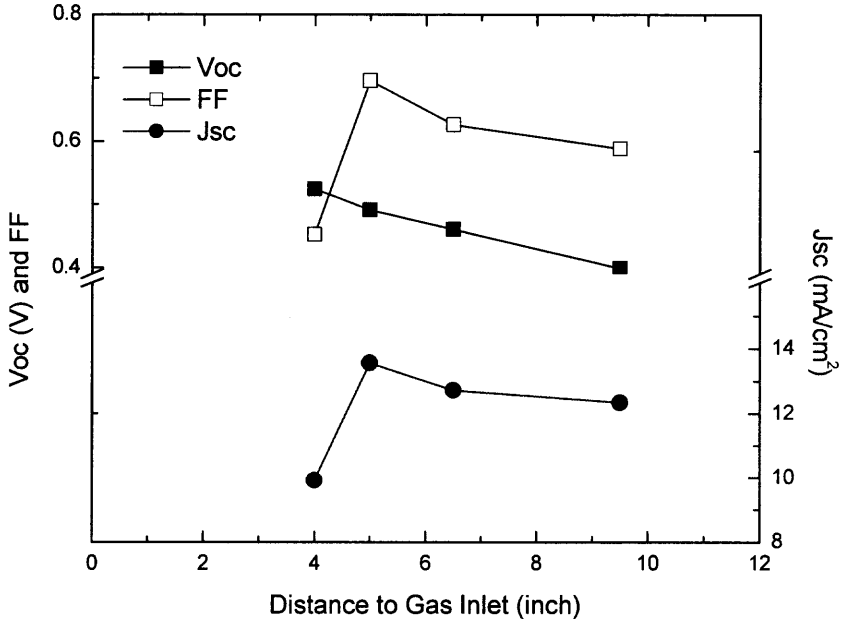

Figure 4.18 Device performance parameters of R140-1 as functions of position.

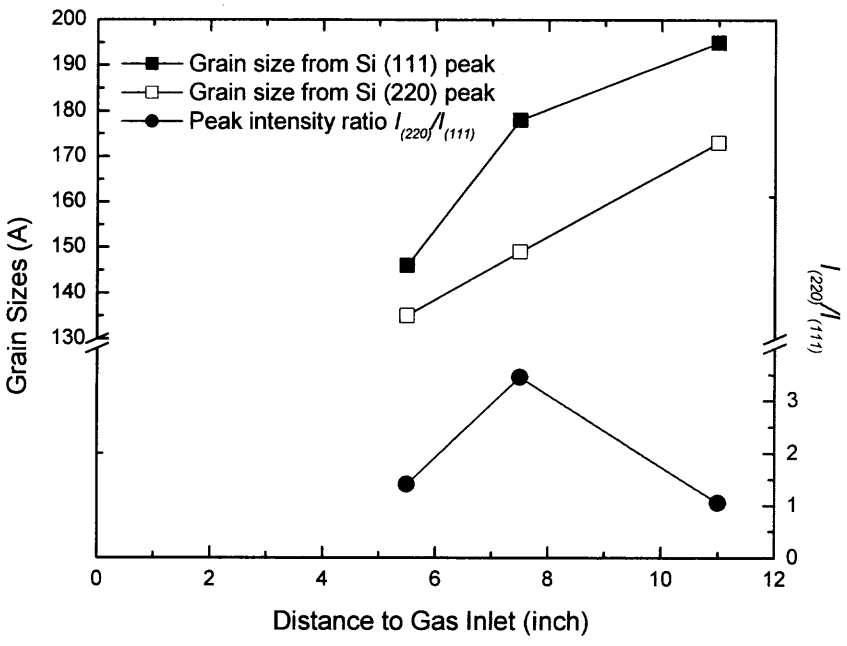

Figure 4.19 Grain sizes and preferential crystalline orientation of R140-1 as functions of position.

It is evident from above figures that the optimal μc-Si:H solar cell made from materials near the μc-Si:H to mixed-phase Si:H transition edge shows smaller grain size and a little preferential growth along Si (220) compared to that made from near gas exhaust materials exhibiting higher micro-crystallinity. Slight difference is observed between grain sizes calculated from Si (111) and Si (220) peaks, however, the general tendencies coincide with each other. Comparing Figure 4.17, Figure 4.18, and Figure 4.19, it can be observed that, for μc-Si:H solar cells with good or fairly well performance, the conversion efficiencies decrease with increasing grain sizes, which also agrees to the report from other groups [96]. Such decrease results from all the three major performance parameters, i.e., Voc, Jsc, and FF. It should be noted here that the assumption of a cubic shape of the coherent domains in the Scherrer Formula may not be true since columnar

growth has been rather widely recognized, and demonstrated in μc-Si:H samples deposited on single crystalline silicon substrates.

Unlike grain sizes, the change of preferential orientation doesn't show a pleasantly steady ascending or descending tendency. Materials between the optimum edge and highly crystalline, near exhaust region clearly show higher Si (220) preferential growth. In the optimum edge and near exhaust, highly crystalline region, Si (220) preference is observed being comparable, but slightly higher at the μc-Si:H to mixed-phase Si:H transition edge. In R140-1, $I_{(220)}/I_{(111)}$ about 1 is observed in these two regions which possibly indicates a non-preferential growth between Si (220) and Si (111) planes. However, it has also been observed in other samples that the edge materials show much higher Si (220) preferential growth than that in near exhaust, more crystalline region.

Crystal grains and grain boundaries are generally considered to strongly affect carrier transport. It is not clear what role is played by the preferential crystalline orientation of the film. While it has been shown that preferential growth strongly depends on plasma conditions, and the competition between selective etching and growth has been proposed as the growth kinetics of favorable crystal directions [104-106], detailed and precise mechanism remains elusive. So far, basic understandings on how the grain sizes and preferential orientation form and how they affect the device performance have yet to be established and more solid experimental evidences are needed.

4.4.4 Atomic Force Microscopy

A wide variety of surface morphologies, corresponding to the non-uniformity of surface appearance and micro-crystallinity, are observed by AFM. AFM surface morphologies of solar cells made from R140-1, with mixed-phase Si:H, near edge μc-Si:H, and highly crystalline μc-Si:H *i*-layers, are shown in Figure 4.20, Figure 4.21, and Figure 4.22, respectively. The surface roughness (RMS, root means square) taken from AFM is also plotted against device position and micro-crystallinity in Figure 4.24. The effect of doped *n*-layer covering *i*-layer is estimated to be little since the *n*-layer is uniformly deposited over entire substrate and its thickness is much less than the height of surface clusters observed in AFM surface morphologies. The corresponding device performance and crystallographic results obtained from XRD can be found in Figure 4.18 and Figure 4.19.

Good correlations among visual non-uniformity pattern, micro-crystallinity, AFM morphologies, and surface roughness are observed. The sample shown in Figure 4.20 (a) is made from the edge of non-uniformity patch. Its surface roughness can even be observed visually by its highly hazy, milky color appearance. Its AFM morphology, featuring sharp, large clusters unevenly distributed across the scanning area, show the highest RMS surface roughness among all samples. Figure 4.20 (b) shows the AFM morphology of the area right in the middle of the non-uniformity patch where, and at the microcrystalline area as well, relatively dull, specular appearance is observed. This mixed-phase Si:H area also shows large clusters but their heights and sharpness are much less than that shown in Figure 4.20 (a), leading to the lowest RMS surface roughness among all samples. Compared to all other samples, its surface morphology is also relatively regular.

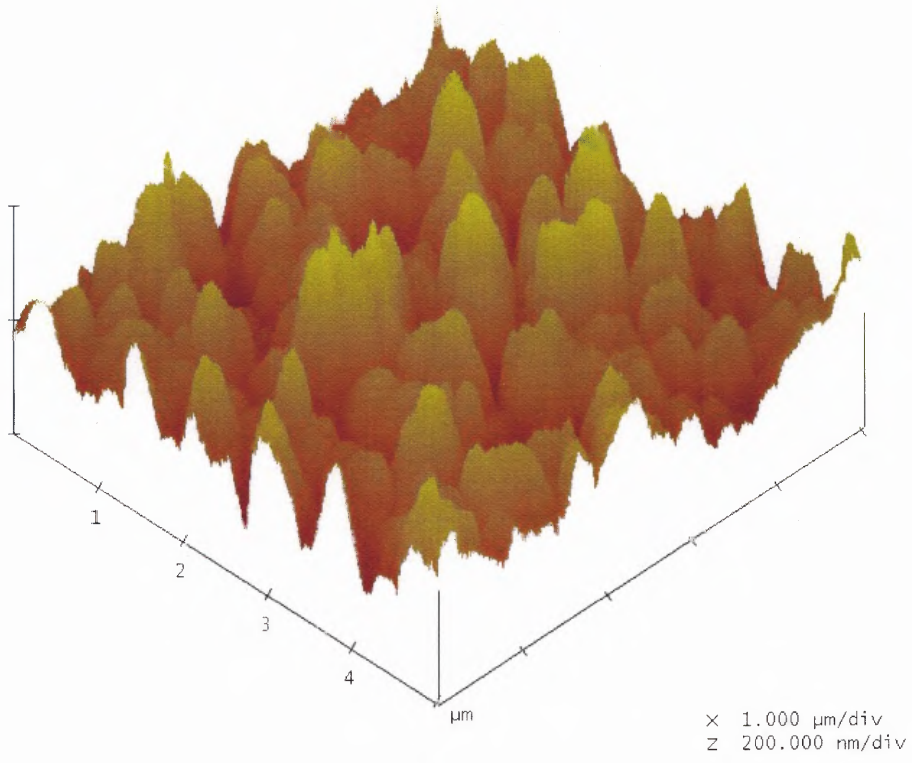

(a) *Ic/Ia* = 0.72, RMS = 48.7 nm

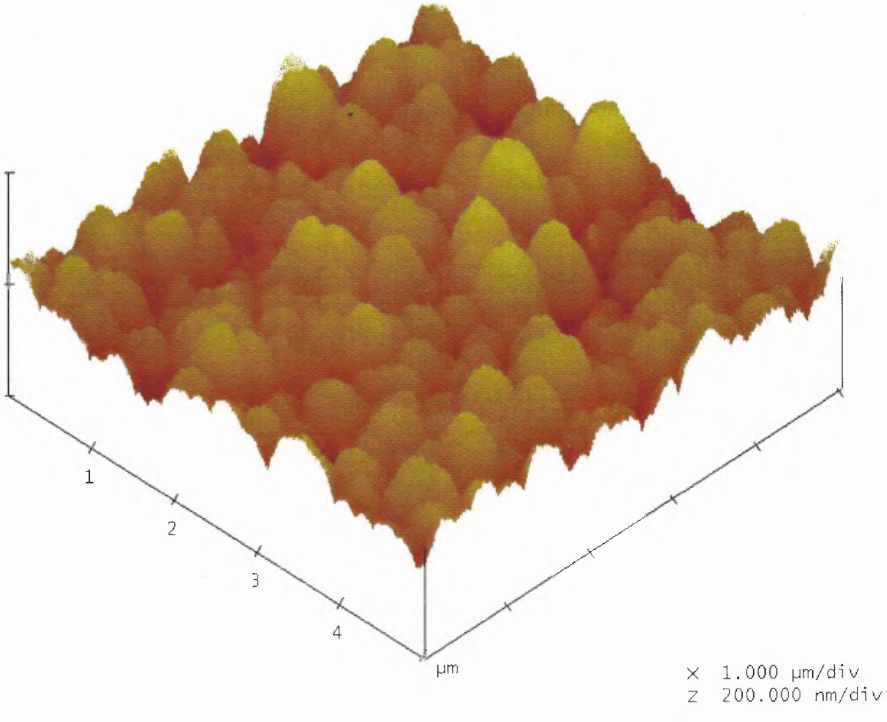

(b) *Ic/Ia* = 0.87, RMS = 28.2 nm

Figure 4.20 AFM morphologies of solar cells with mixed-phase Si:H *i*-layers.

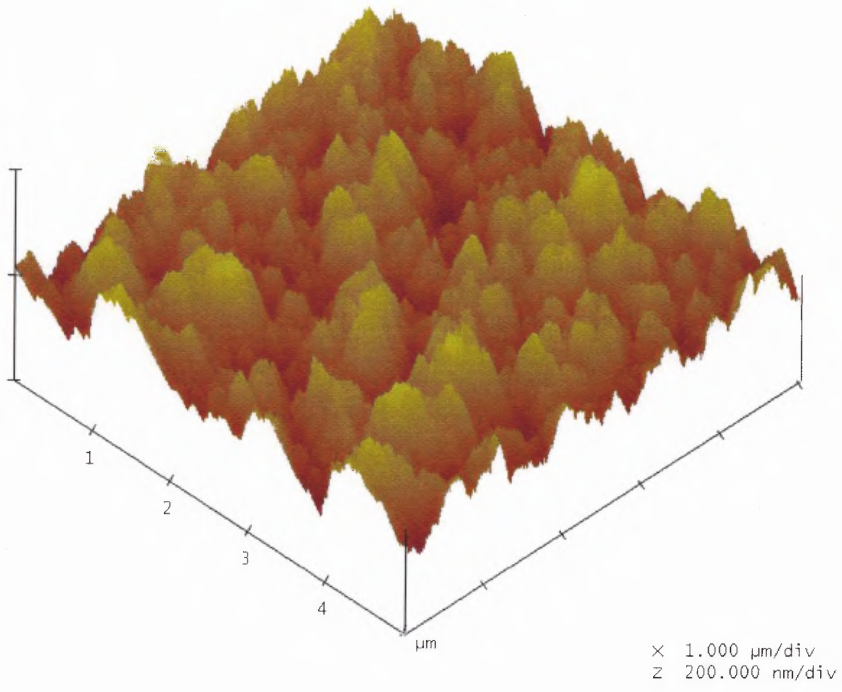

(a) *Ic/Ia* = 1.44, RMS = 30.9 nm

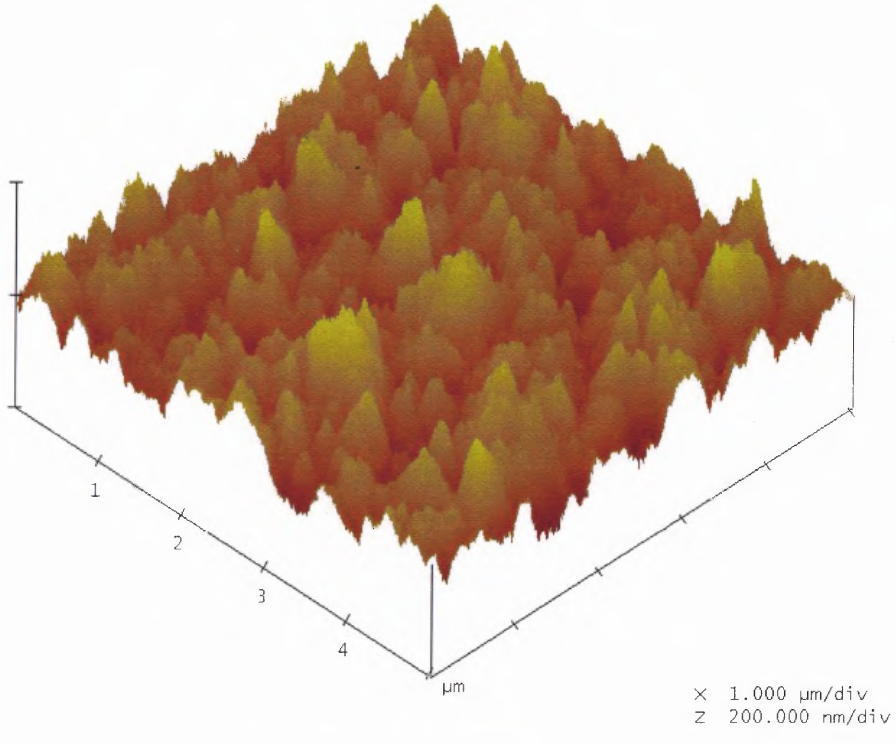

(b) *Ic/Ia* = 1.97, RMS = 29.4 nm

Figure 4.21 AFM morphologies of solar cells with near edge μc-Si:H *i*-layers.

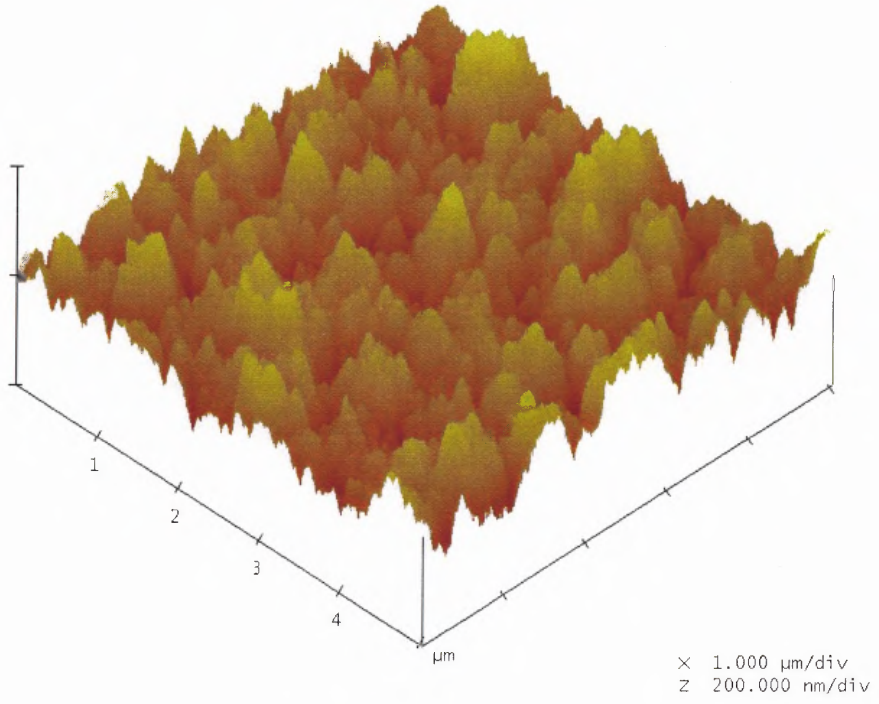

(a) *Ic/Ia* = 2.11, RMS = 33.8 nm

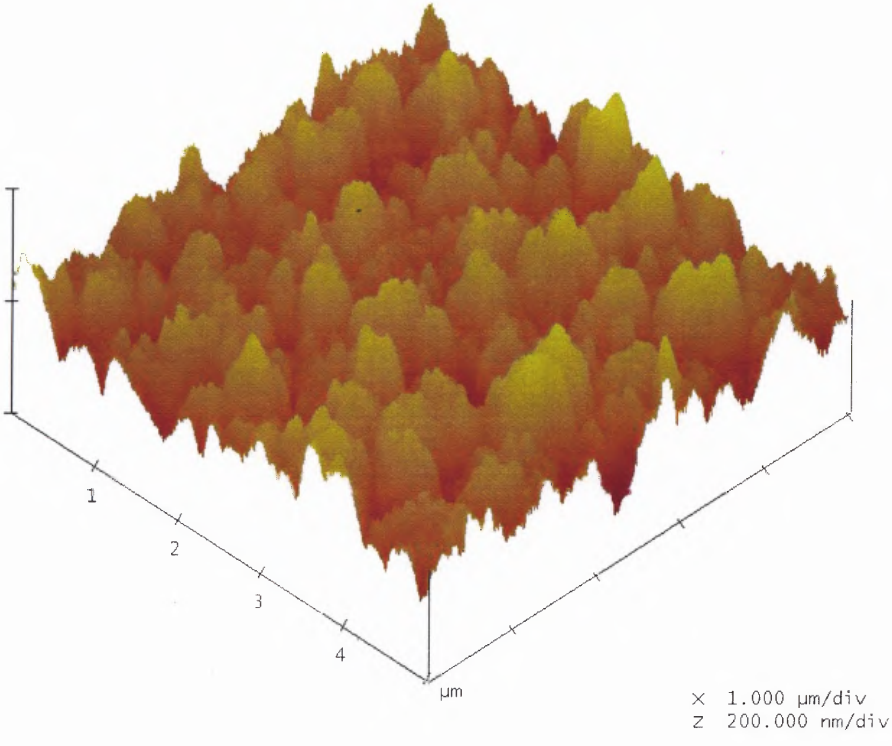

(b) *Ic/Ia* = 2.15, RMS = 34.8 nm

Figure 4.22 AFM morphologies of µc-Si:H solar cells with high micro-crystallinity.

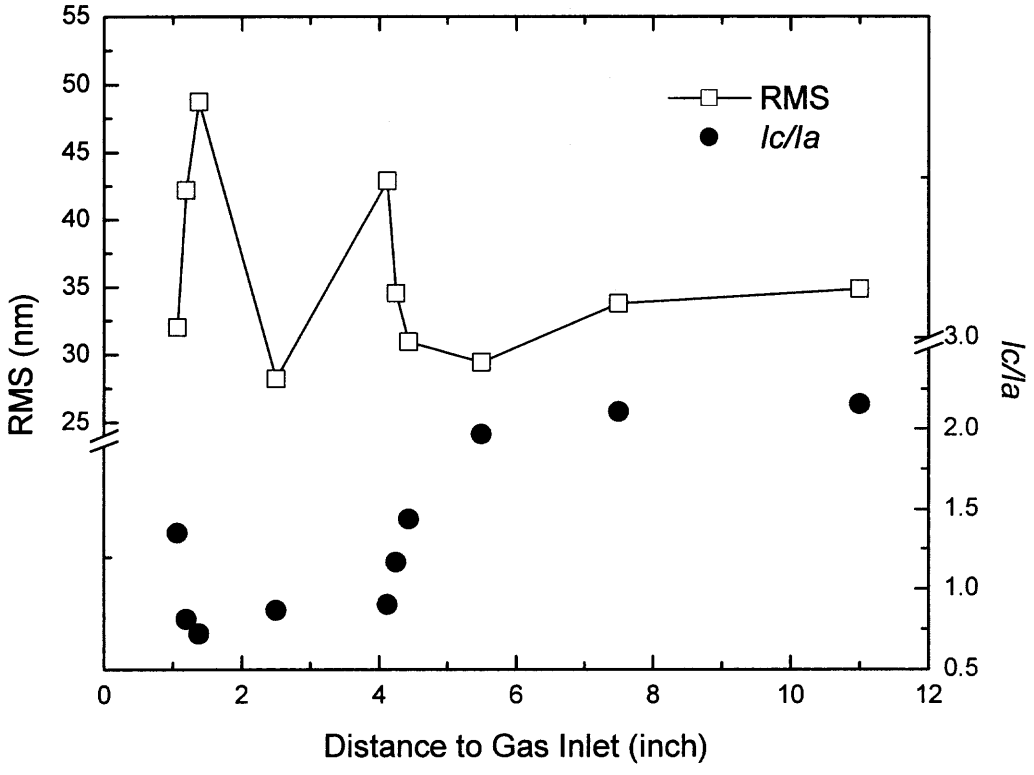

Figure 4.23 Micro-crystallinity and surface roughness of μc-Si:H solar cells as functions of position.

Figure 4.21 (b) shows the surface morphology of the optimum edge, and Figure 4.21 (a) shows the surface morphology of area between the optimum edge and non-uniformity patch, respectively. Figure 4.22 shows the surface morphologies of highly crystalline areas more towards the gas exhaust. All these surface morphologies show comparable RMS surface roughness and similar features, i.e., numerous small clusters with some large aggregates distributed among them. The major difference of surface morphologies between the area shown in Figure 4.21 (a), which shows low micro-crystallinity and worse device performance, and the other three highly crystalline areas is that the size of its small clusters is relatively larger. Among the optimum edge area and

more crystalline areas near gas exhaust, the major difference is that the amount of large aggregates increases with increasing micro-crystallinity (closer to gas exhaust).

In brief, compared to mixed-phase Si:H area, highly crystalline areas show less regular surface morphologies with smaller feature sizes. The optimum edge area, where the highest performance devices are made, shows smallest surface feature (cluster) sizes. The strong phase transition edges (edges of the non-uniformity patch) show highest RMS surface roughness which is mainly resulting from large and sharp surface clusters. Among highly crystalline areas, the optimum μc-Si:H to mixed-phase Si:H transition edge shows lowest surface roughness.

The non-uniform distribution of local SiHx concentration during *i*-layer deposition, probably during seeding process as well, is surely the major cause of the non-uniformity discussed above. If the columnar growth model by far proposed based on hydrogen dilution ratio [88, 96, 107] represents the real scenario, the AFM morphologies might imply, though highly speculative, some correlations between surface morphologies and processes of μc-Si:H nucleation and growth. In the areas sufficient Si precursors are supplied during *i*-layer deposition, e.g., the middle of the patch, surface morphology similar to that of α-Si:H samples is observed (Figure 4.20 (b)). In the highly crystalline area, competitive growth among μc-Si:H crystallites results in small crystal clusters and coalescence of some clusters forms large aggregates, which are possibly responsible for the preferential growth orientation as well. As proposed by the columnar growth models, higher silane depletion results in stronger grain coalescence, leading to more large aggregates at areas near gas exhaust where silane depletion is enhanced. The change of grain sizes against sample positions on the substrates obtained from XRD measurement,

shown in Figure 4.19, agrees to the above assumption as well. Stronger grain coalescence occurred near the gas exhaust area not only leads to larger grain sizes, but also leads to relatively higher RMS roughness as shown in Figure 4.23, which agrees to the surface roughness change deduced from real time spectroscopic ellipsometry [89].

However, no clues are obtained so far by direct structural characterization pertaining to what happens at the strong phase transition edges, how the crystallographic texture (preferential orientation) forms, how the grain sizes and crystallographic texture affect the device performance, etc. Though basic understandings on these questions are sorely needed, it is very difficult to get direct evidence in view of the complexity taken on by μc-Si:H materials deposited using complicated seeding processes and *i*-layer deposition conditions.

4.5 Stability of μc-Si:H Solar Cells Under Light Soaking

Both conventional and accelerated light soaking experiments are performed in this study. The accelerated light soaking, simulating 47 suns, needs only several minutes to produce similar light-induced degradation as that produced by conventional light soaking for over a month. Though accelerated light soaking has been used since 1980s, a widely accepted model has yet to be established to explain the mechanisms of light-induced degradation under intensive light exposure, and relationships between conventional and accelerated light soaking tests remain unclear [108-110]. Some of the light soaking experiments, therefore, are designed in a tightly related manner so that the results obtained from both methods can be compared and the suitability of accelerated light soaking in assessing the stability of μc-Si:H solar cells can be certified.

4.5.1 Conventional Light Soaking

Like other device performance parameters, stability of solar cells fabricated in this study is also highly dependent on *i*-layer micro-crystallinity and strong variations are observed. Conventional light soaking curves of solar cells deposited from different runs are compared in Figure 4.24 in terms of relative efficiency, i.e., efficiency after light soaking divided by initial efficiency. Very good stability, with less 3% degradation after light soaking for over 1000 hours, is observed in sample R140-1 which is made from the aforementioned optimum 'edge' materials. However, solar cell with mixed-phase Si:H *i*-layer, which may have relatively high initial efficiency, suffers from severe light-induced degradation (>50% degradation for R60-1), even worse than 'standard' α-Si:H solar cells. Solar cells with micro-crystallinity between mixed-phase Si:H and optimal μc-Si:H generally show light-induced degradation comparable with that of α-Si:H solar cells.

Seeding methods also play an important role as indicated by Figure 4.24. Though sample R140-1 and R60-1 exhibit similar overall micro-crystallinity as revealed by Raman scattering, R140-1, deposited by *p*-layer seeding, has much better stability than R60-1 which is deposited using *i*-layer seeding. Once again, such difference easily makes us speculate that the inferior stability of μc-Si:H solar cells deposited by *i*-layer seeding methods may be related to the damages inside *i*-layer created by *i*-layer seeding approach. More hydrogen may reside in the *i*-layer deposited by *i*-layer seeding due to thicker transition layer and consequently contribute to the light-induced degradation.

Efficiency of R69-3 increases slightly in the beginning of light soaking and such tendency also appears in some other μc-Si:H solar cells deposited using plasma

conditions prone to introducing more defects inside *i*-layers. Since the solar cells weren't annealed before light soaking, such efficiency change may result from low temperature annealing which cures some unstable defects created by *i*-layer seeding though other possibilities may also exist.

No general tendencies regarding the changes of performance parameters are found during conventional light soaking. Usually fill factor is the parameter dropping a lot but other parameters such as Jsc and Voc may play roles as well. Some times one of the three parameters may increase while the overall efficiency decreases significantly.

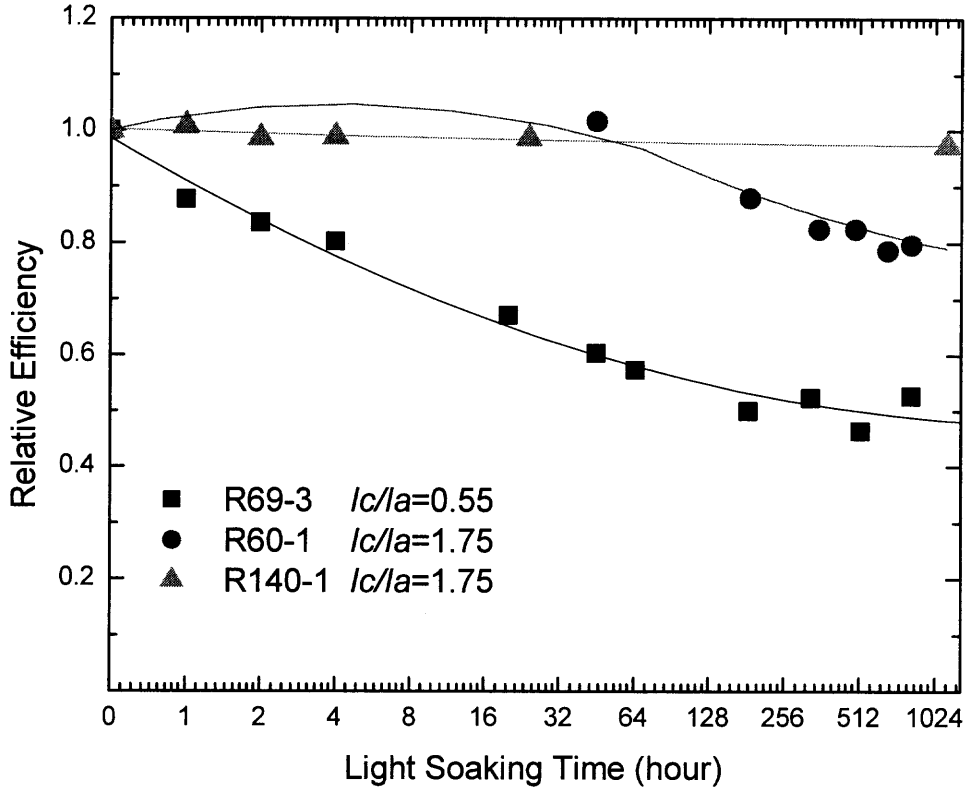

Figure 4.24 Relative efficiencies of μc-Si:H solar cells under conventional light soaking.

To more closely compare the stability of μc-Si:H solar cells with various *i*-layer micro-crystallinity, light-induced degradations of solar cells made from R140-1 are plotted in Figure 4.25 as a function of position and micro-crystallinity. Only solar cell with mixed-phase Si:H *i*-layer shows significant light-induced degradation. Very good stability, even slight efficiency increase during some test, is observed in solar cells with highly crystalline *i*-layers.

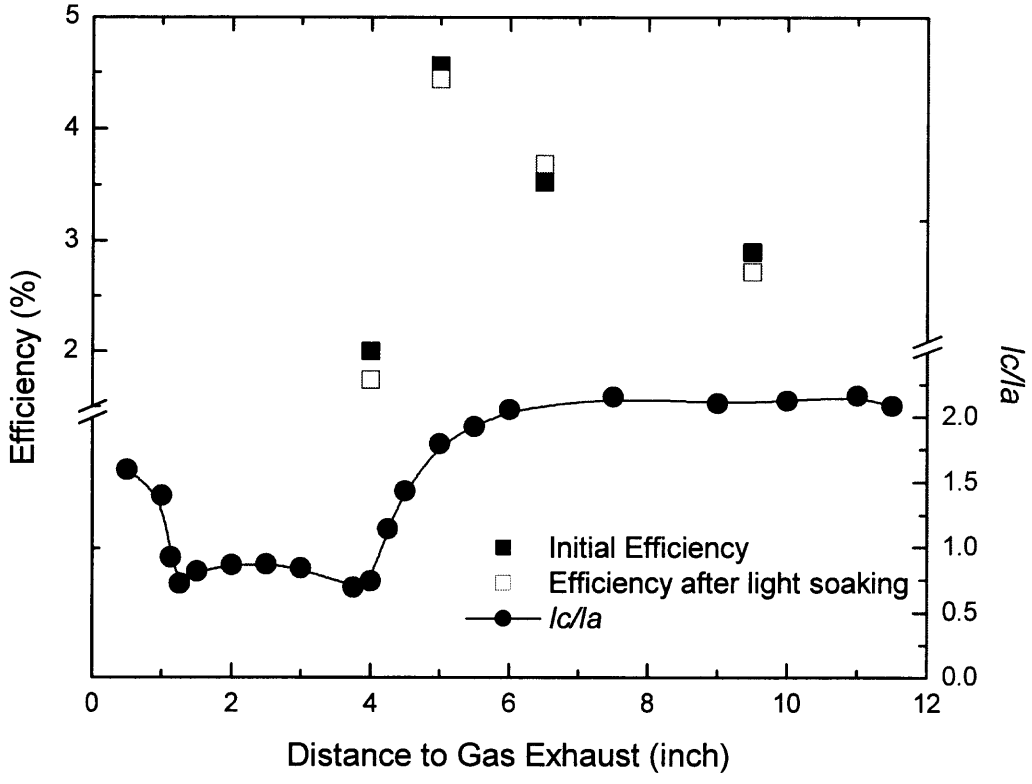

Figure 4.25 Stability of μc-Si:H solar cells made from R140-1 as a function of position and *i*-layer micro-crystallinity.

4.5.2 Accelerated Light Soaking

Three sets of samples are made from R140-1 at various positions corresponding to different micro-crystallinity, with 3 identical solar cells at each position. Two sets of them underwent annealing at 150 °C for 1 hour and then were light soaked under conventional and accelerated light soaking conditions, respectively. The un-annealed set was directly subject to accelerated light soaking. The total accelerated light soaking time is 300 seconds which has been confirmed using α-Si:H solar cells to be long enough to produce light-induced degradation as the saturated degradation produced by conventional light soaking for hundreds of hours.

Results of conventional light soaking of one of the annealed sets have been shown in Figure 4.25. Accelerated light soaking curves of the other annealed set are shown in Figure 4.26. In Figure 4.26, despite the initial efficiencies, same tendencies are observed as that obtained from conventional light soaking. Except the device with mixed-phase Si:H *i*-layer which shows ~21% light-induced degradation, all other three highly crystalline solar cells exhibit excellent stability against light soaking. The encouraging result is that the solar cell made from optimum 'edge' materials not only shows high initial efficiency, but also has excellent stability against light-induced degradation (~2%). Solar cells with *i*-layers showing higher micro-crystallinity than that of the 'edge' materials don't exhibit any light-induced degradation at all. Efficiency of the cell made near the gas exhaust even increases slightly after accelerated light soaking.

The slight efficiency increase observed in Figure 4.25 and Figure 4.26 is not atypical. Under accelerated light soaking, while the annealed solar cells with high micro-crystallinity are very stable, more efficiency increase is usually observed in un-annealed,

highly crystalline solar cells. Comparison between accelerated light soaking of the annealed and un-annealed sets is shown in Figure 4.27. It can be seen that, except for the mixed-phase Si:H cell, other annealed solar cells with truly μc-Si:H *i*-layers are all quite stable. However, un-annealed sample #5 and #6, which have higher micro-crystallinity than that of the 'edge' μc-Si:H solar cells, exhibit obvious efficiency increase during accelerated light soaking. In other words, annealing stabilizes solar cells. In the case of mixed-phase Si:H solar cells, such stabilization is indicated by the reduction of light-induced degradation when the mixed-phase Si:H solar cell is annealed before accelerated light soaking.

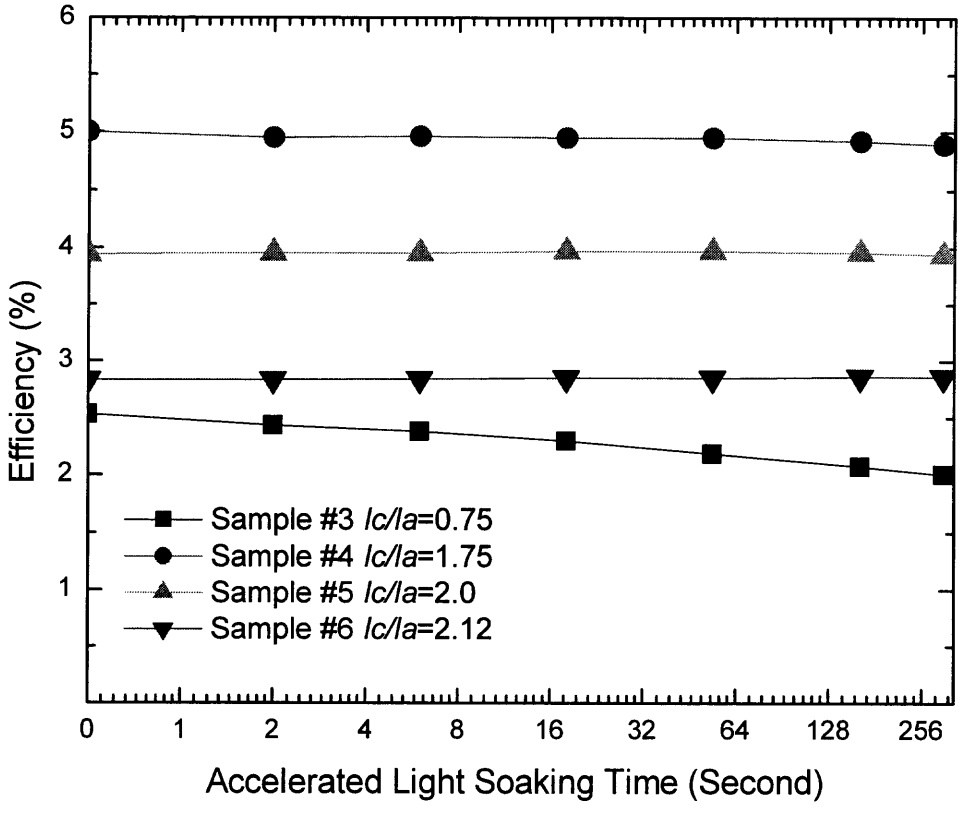

Figure 4.26 Accelerated light soaking of solar cells made from R140-1.

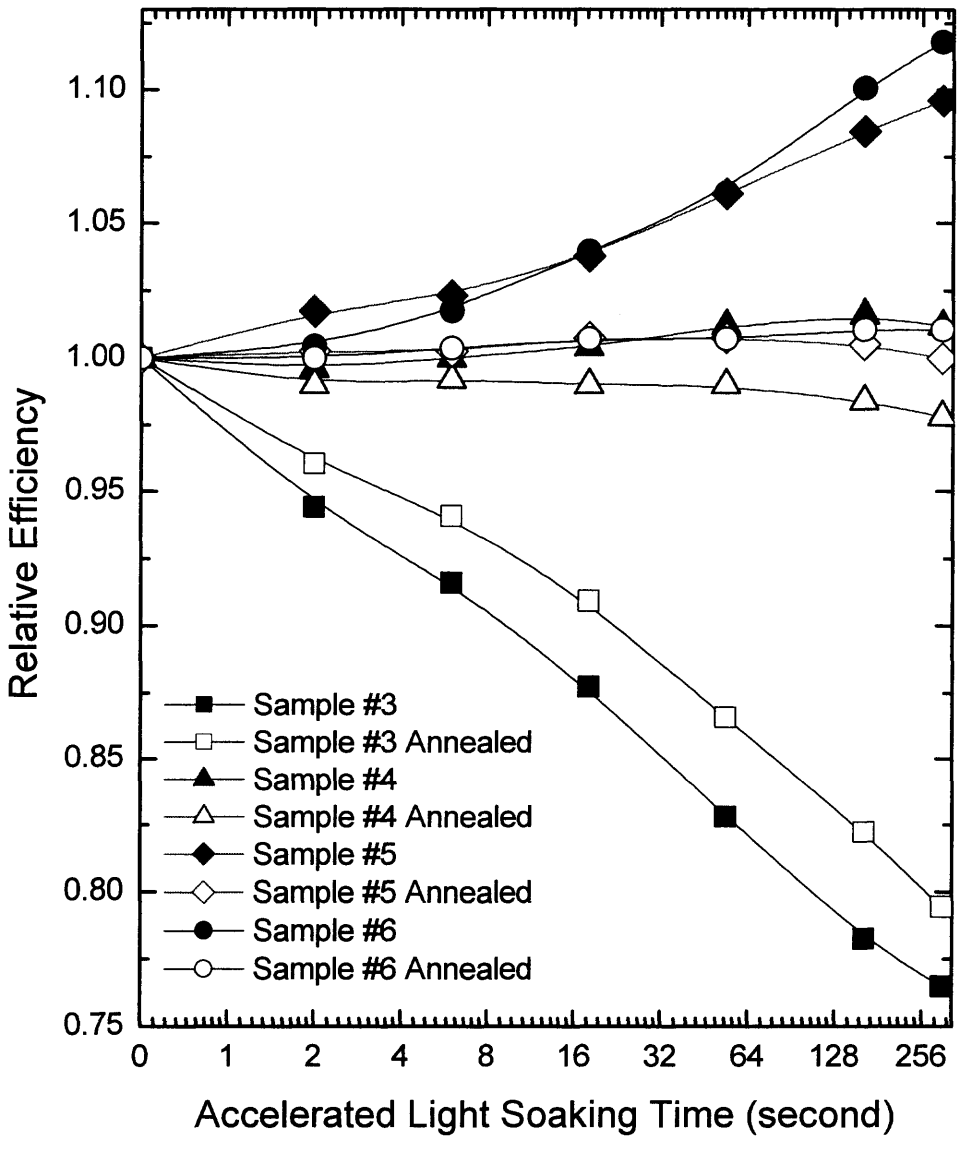

Figure 4.27 Comparison of accelerated light soaking of solar cells with and without annealing.

Coincidently, it is demonstrated in Table 4.5 that annealing alone results in similar effect as that of accelerated light soaking on the efficiency change of un-annealed solar cells. After annealing, efficiencies of solar cells with μc-Si:H *i*-layers increase and higher micro-crystallinity corresponds to higher efficiency increase. On the other hand, annealing results in efficiency decrease for mixed-phase Si:H solar cell. Carefully comparing Figure 4.27 and Table 4.5, it can be found that, in either mixed-phase Si:H or μc-Si:H solar cells, accelerated light soaking of un-annealed solar cells reaches, in terms of overall efficiency, similar effect as that of annealing plus accelerated light soaking of annealed solar cells though detailed performance parameter changes may not be the same. It is understandable if accelerated light soaking cures some unstable defects and thus results in the stabilization effect shown in Figure 4.27 and Table 4.5. Though the surface temperature of the sample undergoing accelerated light soaking is about 40 °C, the real temperature inside the devices may reach about 80 °C as revealed by Voc change measured during accelerated light soaking.

Table 4.5 Effect of Annealing on the Performance of μc-Si:H Solar Cells

Sample	*Ic/Ia*	Parameter Change (%)			
		Voc	Jsc	FF	Efficiency
#3	0.75	2.2	-5.7	-5.0	-8.5
#4	1.75	2.7	0.7	3.1	6.6
#5	2.0	6.2	3.2	5.9	16.1
#6	2.12	7.5	4.1	6.7	19.6

Detailed performance changes of un-annealed sample #3 (mixed-phase) and sample #6 (highly crystalline) under accelerated light soaking are shown in Figure 4.28 and Figure 4.29, respectively. In either case, FF is the most increased parameter after accelerated light soaking, which is consistent with the assumption that accelerated light soaking cures some unstable defects as FF is strongly affected by *i*-layer defects that weaken the internal electrical field and serve as recombination centers.

The light soaking experiment confirms that solar cells with truly μc-Si:H *i*-layers exhibit excellent stability against light-induced degradation. On the other hand, mixed-phase Si:H solar cells show much worse stability against light soaking. Though the microscopic mechanisms governing the light-induced degradation in α-Si:H are still not fully understood, most models proposed so far specify the involvement of hydrogen during the light-induced creation of mete-stable defects which reduce photo-conductivities of α-Si:H [111]. Thus, reasons responsible for the excellent stability of μc-Si:H solar cells might be relatively straightforward. It has been shown that hydrogen incorporation in μc-Si:H is significantly reduced compared to that in α-Si:H [112] and that might be responsible for the greatly improved stability of μc-Si:H solar cells. Such study also showed that hydrogen incorporation in materials in or near α-Si:H to μc-Si:H transition is enhanced even compared with that in α-Si:H. This could be one of the reasons responsible for the extremely inferior stability shown in solar cells with mixed-phase *i*-layers. The efficiency and fill factor decreases of mixed-phase Si:H solar cells after annealing could also be related to higher hydrogen content, i.e, hydrogen diffusion or interaction between hydrogen and other structural defects at relatively high temperature leave more dangling bonds which serve as recombination centers.

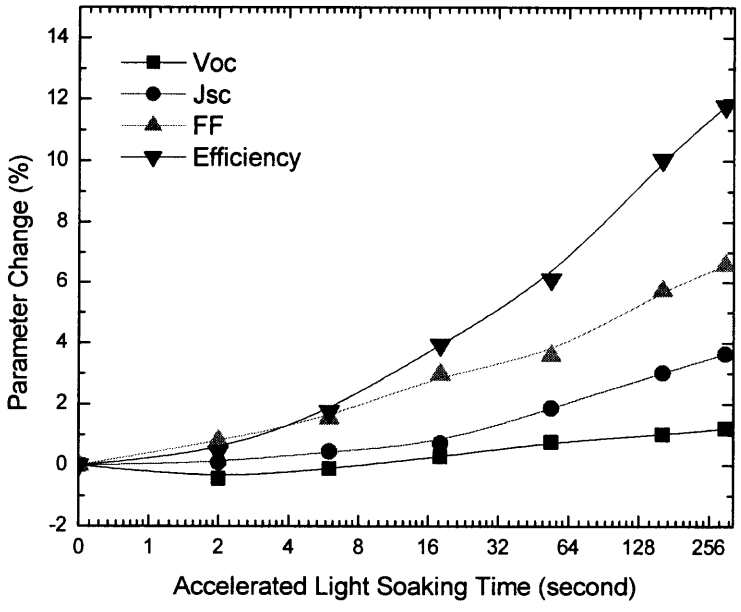

Figure 4.28 Performance change of un-annealed μc-Si:H solar cell during accelerated light soaking.

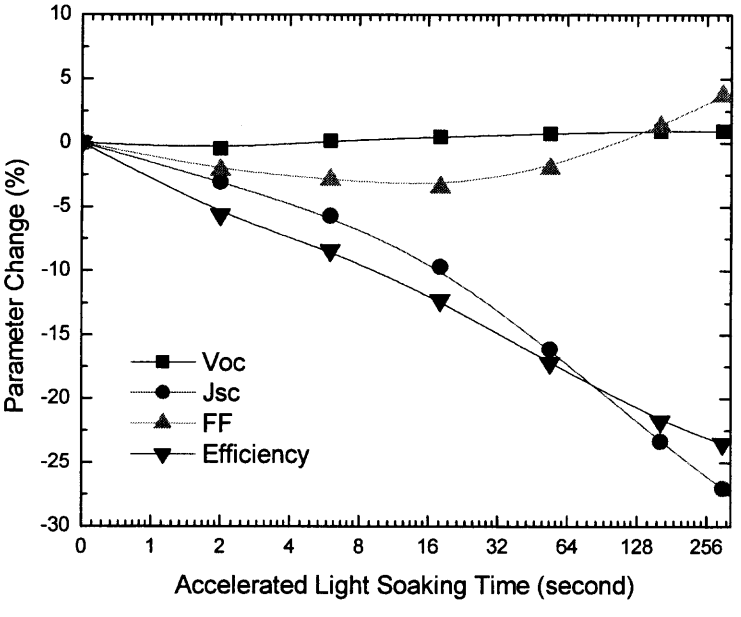

Figure 4.29 Performance change of un-annealed mixed-phase Si:H solar cell during accelerated light soaking.

Though all solar cells with high micro-crytallinity exhibit excellent stability under light soaking, only the optimum 'edge' solar cells, which also show the highest initial efficiencies, are stable before and after annealing as well as accelerated light soaking. Such solar cells also show highest fill factors which are comparable with that of standard α-Si:H solar cells, as shown in Figure 4.18. The efficiency increase for those highly microcrystalline solar cells upon annealing and accelerated light soaking implies that more defects exist within those materials than that in the 'edge' materials. The microscopic mechanisms for the inferior performance of solar cells made from such more crystalline materials, i.e., what defects they are, how they are created, and how they affect device performance, have yet to be understood. However, the optimum 'edge' revealed by structural characterization, combined with light soaking experiments, further confirm one of the most critical issues in depositing high quality μc-Si:H *i*-layers, i.e., extremely narrow processing window for high quality μc-Si:H. So far high efficiency, stable μc-Si:H solar cells can only be obtained from devices with *i*-layer being μc-Si:H and very close to the edge of μc-Si:H to mixed-phase Si:H transition.

In the final part of this section, light soaking results under conventional and accelerated light soaking are compared in Table 4.6. The initial efficiencies are also listed in Table 4.6 as a figure of merit. Though the changes of specific parameters may not be identical, consistent tendencies in light-induced degradation for annealed solar cells are obtained from both conventional and accelerated light soaking. The effect of annealing, i.e., stabilizing solar cells, can also be found in Table 4.7. For μc-Si:H solar cells, annealing reduces the light-induced efficiency increase. For mixed-phase Si:H solar cells, on the other hand, annealing reduces the light-induced degradation. This comparison

further confirms that accelerated light soaking is a reliable technique to quickly evaluate the stability of μc-Si:H solar cells.

Table 4.6 Comparison of Conventional and Accelerated Light Soaking

Sample	*Ic/Ia*	Anneal	Method	Parameter change (%)				Initial Efficiency (%)
				Voc	Jsc	FF	Efficiency	
#3	0.75	Yes	Normal	-1.6	-22.0	13.3	-13.0	2.0
		Yes	Accelerated	0.1	-16.4	7.8	-20.6	2.53
		No	Accelerated	0.9	-27.1	3.7	-23.5	2.85
#4	1.75	Yes	Normal	-3.3	6.9	-5.6	-2.6	4.56
		Yes	Accelerated	-0.2	-0.6	-1.5	-2.2	5.0
		No	Accelerated	0.5	-0.3	1.1	1.2	4.98
#5	2.0	Yes	Normal	0.5	3.9	0	4.5	3.52
		Yes	Accelerated	-0.7	-1.5	2.2	0	3.94
		No	Accelerated	1.4	0.1	7.9	9.6	3.44
#6	2.12	Yes	Normal	-2.0	-0.4	-4.0	-6.2	2.9
		Yes	Accelerated	-0.3	-0.5	1.8	1.1	2.83
		No	Accelerated	1.2	3.6	6.6	11.8	2.29

4.6 Correlations between Micro-Crystallinity and Device Performance

Strong correlations between device performance and *i*-layer micro-crystallinity (*Ic/Ia*) can be observed when the performance parameters of solar cells are plotted as functions of micro-crystallinity regardless of sample position and deposition conditions.

Relationships between *Ic/Ia* and Voc, as well as red-light response, are shown in Figure 4.30 and Figure 4.31, respectively. Generally, solar cells with mixed-phase Si:H *i*-layers exhibit high Voc and low red-light response while solar cells with μc-Si:H *i*-layers show low Voc and high red-light response. Though the red-light response measured without bias is rather scattered at high *Ic/Ia*, the tendency mentioned above is much enhanced when the QE are measured under -3 V bias, as shown in Figure 4.32. In either case, highest red-light response is found at a narrow optimum *Ic/Ia* range (around 1.8). Voc is found to be about 0.5 V or slightly lower at same optimum *Ic/Ia* range. Actually, this *Ic/Ia* range exactly corresponds to the optimum μc-Si:H to mixed-phase Si:H transition 'edge' identified by structural characterization. The relationships between *Ic/Ia* and efficiencies of solar cells with various *i*-layers can be found in Figure 4.33. Since the overall conversion efficiency, as well as Jsc and fill factor, are more severely affected by defects created by hydrogen rich plasma conditions than Voc and red-light response, the data in Figure 4.33 are rather scattered. However, the highest efficiencies are also obtained at the optimum *Ic/Ia* range identified in Figure 4.31 and Figure 4.32. Though very high initial efficiencies can also be obtained at very low *Ic/Ia* value, such mixed-phase Si:H solar cells suffer from severe light-induced degradation, even worse than typical α-Si:H solar cells, as confirmed by Figure 4.34 and Figure 4.35. Relationships between *Ic/Ia* and Jsc exhibit similar feature as that of efficiency vs. *Ic/Ia*

with highest Jsc found at the optimum *Ic/Ia* or very low *Ic/Ia* range. The FF data are also scattered as a function of *Ic/Ia*, however, highest FF are observed only at the optimum *Ic/Ia* range.

Excellent stability under both conventional and accelerated light soaking for μc-Si:H solar cells with optimum *Ic/Ia* value, i.e., *Ic/Ia* at around 1.8, is confirmed by Figure 4.34 and Figure 4.35, respectively. The effect of seeding methods on the stability against light-induced degradation, i.e., *p*-layer seeding results in more stable solar cells than *i*-layer seeding, can also be observed in Figure 4.34. In Figure 4.35 which illustrates the results of accelerated light soaking, light-induced efficiency increases are observed in un-annealed highly crystalline solar cells. However, such increases are significantly reduced once the solar cells are annealed before accelerated light soaking.

In brief, solar cells with mixed-phase Si:H *i*-layers, i.e., low *Ic/Ia*, usually exhibit high Voc, low fill factors, low efficiencies (though high initial efficiencies can also be observed for some samples), and severe light-induced degradation. Solar cells with higher *Ic/Ia*, on the other hand, show low Voc, high fill factors, high efficiencies, and excellent stability against light-induced degradation. However, μc-Si:H solar cells with both high initial and stabilized efficiencies can only be obtained at a very narrow optimum micro-crystallinity range, i.e., *Ic/Ia* at around 1.8. Such an optimum micro-crystallinity range precisely corresponds to the optimal μc-Si:H materials at the μc-Si:H to mixed-phase Si:H transition edge, as revealed by structural characterization. The optimum μc-Si:H solar cells are usually deposited using *p*-layer seeding methods and exhibit moderate Voc (~0.5 V), high fill factors, and high red-light response. Compared to μc-Si:H solar cells with higher *Ic/Ia*, the optimum 'edge' μc-Si:H solar cells also show

smaller grain sizes. However, reasons responsible for the deteriorated performance of solar cells with higher micro-crystallinity remain unclear. The possible causes may mostly relate to the grain boundaries such as efficient contamination (contaminant precipitation), higher defect density, and less effective hydrogen passivation of dangling bonds in or near grain boundaries.

From these figures, in particular Figure 4.32 and Figure 4.33, a very narrow optimum processing window for high quality μc-Si:H *i*-layers is identified, i.e., μc-Si:H solar cells with high initial and stabilized efficiencies can only be obtained under deposition conditions which can produce μc-Si:H *i*-layers with the optimum micro-crystallinity. This issue, joined by the critical importance of seeding methods in μc-Si:H *i*-layer growth and device performance, as well as the spatial non-uniformity of *i*-layer microstructure and device performance revealed by structural characterization, present the major challenges in depositing high performance μc-Si:H solar cells in a low-cost, large-scale RF-PECVD system. While the seeding methods can be systematically investigated and the non-uniformity can be improved by modify reactor geometries and gas flow patterns, the narrow optimum processing window, mainly affected by the local SiHx concentrations under high plasma power and high silane depletion conditions, must be addressed with extensive efforts in the future to develop low-cost, high efficiency μc-Si:H solar cells.

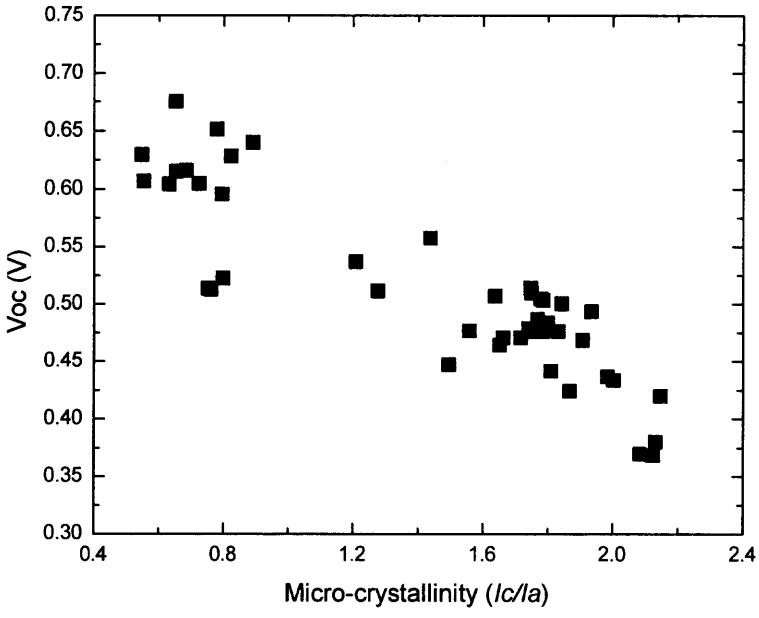

Figure 4.30 Voc as a function of micro-crystallinity.

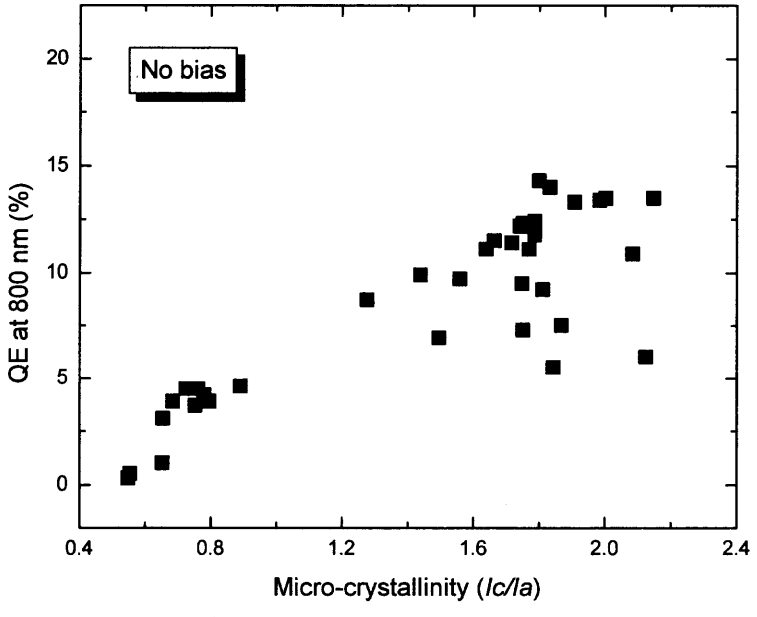

Figure 4.31 Red-light response without bias as a function of micro-crystallinity.

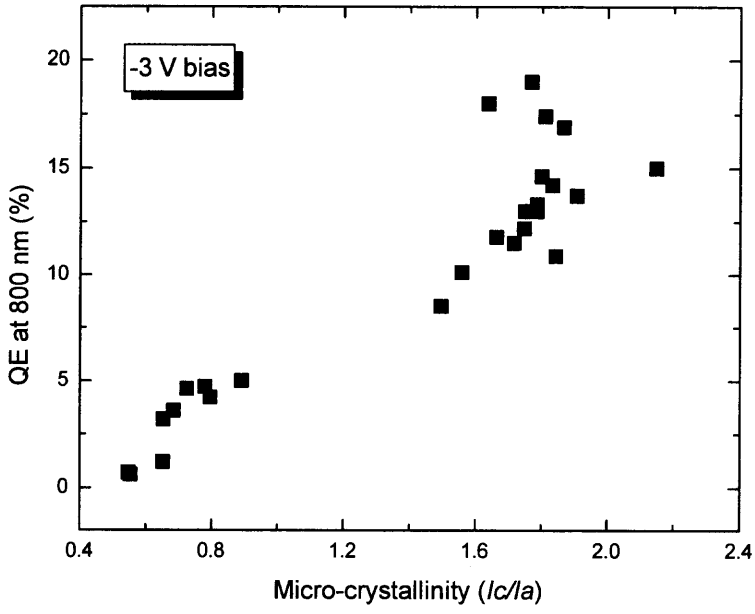

Figure 4.32 Red-light response under -3 V bias as a function of micro-crystallinity.

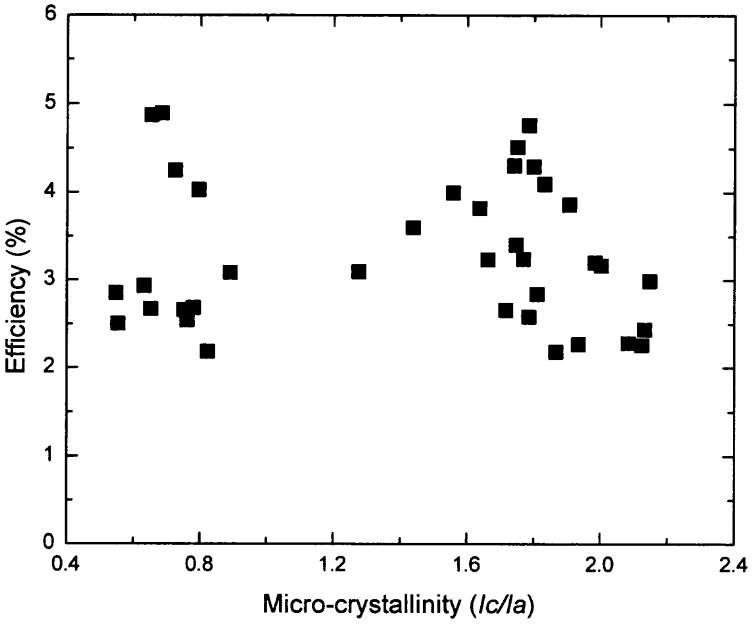

Figure 4.33 Efficiency as a function of micro-crystallinity.

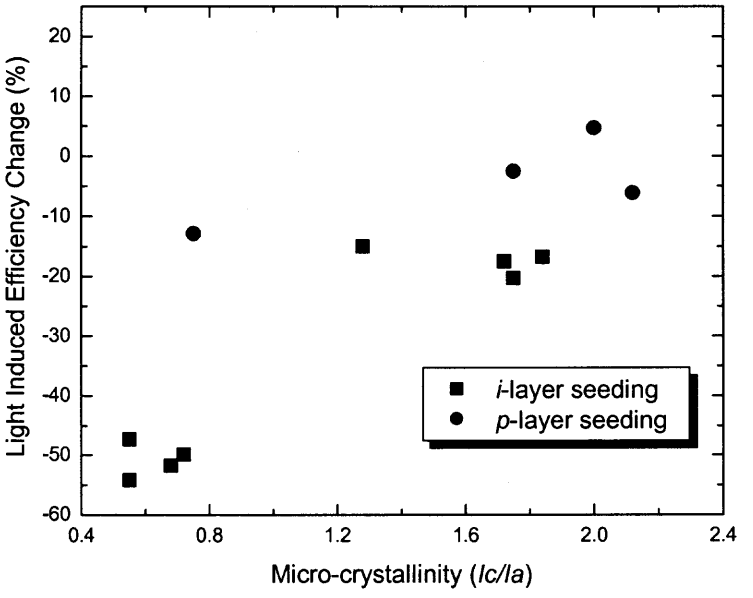

Figure 4.34 Light-induced efficiency change under conventional light soaking as a function of micro-crystallinity

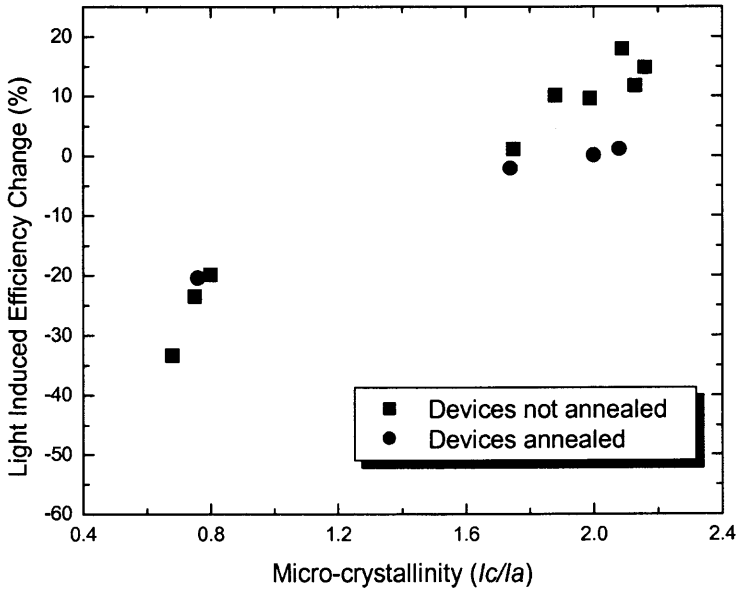

Figure 4.35 Light-induced efficiency change under accelerated light soaking as a function of micro-crystallinity.

CHAPTER 5

CONCLUSIONS

In this study, single junction *p-i-n* μc-Si:H solar cells, without any back reflectors or other light trapping enhancement, were prepared on commercial grade SnO_2/Soda-lime glass superstrates using plasma of silane diluted by hydrogen in a low-cost, single chamber, non-load-locked RF-PECVD system. Direct structural characterization of μc-Si:H solar cells, rather than stand-alone films, was conducted using Raman scattering, XRD, and AFM. Strong correlations among device deposition processes, *i*-layer structural properties, and device performance have been established. With such correlations, critical issues in fabricating low-cost, high performance μc-Si:H solar cells were identified.

The critical importance of seeding processes in determining the microstructure of μc-Si:H *i*-layers and performance of μc-Si:H solar cells has been demonstrated. Both *i*-layer and *p*-layer seeding methods were widely explored in this study. Without effective seeding, *i*-layers may stay amorphous even though very high hydrogen dilution is used. Inappropriate seeding procedure can damage *i*-layer and significantly reduce device performance. It was shown that performance of μc-Si:H solar cells produced by *i*-layer seeding methods is usually limited by very low fill factors. Using *p*-layer seeding methods, which take the advantage of limiting damages associated with hydrogen rich plasma within photovoltaic non-active *p*-layer, stable conversion efficiencies of 5% have been achieved using the simple device configuration employed in this study.

Micro-crystallinity obtained from Raman scattering, presented as *Ic/Ia*, has proven to be sensitive to the microstructure of μc-Si:H *i*-layers and used as a major parameter to study the correlations between device performance and structural properties of μc-Si:H solar cells. Strong spatial non-uniformity of *i*-layer microstructure and device performance was identified as another critical issue severely hindering the fabrication of low-cost, large-scale μc-Si:H solar cells. A wide variety of *i*-layer microstructures, from mixed-phase Si:H to highly crystalline μc-Si:H, were revealed by Raman scattering. Generally, solar cells with mixed-phase Si:H *i*-layers, i.e., low *Ic/Ia*, exhibit high open circuit voltages, low fill factors, low efficiencies, and severe light-induced degradation. Solar cells with truly μc-Si:H *i*-layers, on the other hand, show low open circuit voltages, high fill factors, high efficiencies, and excellent stability against light-induced degradation. It was shown by XRD experiment that high performance, optimum μc-Si:H solar cells exhibit smaller grain sizes compared to solar cells with *i*-layers showing higher micro-crystallinity. Correlations among non-uniformity pattern, *i*-layer micro-crystallinity, and AFM surface morphologies were also observed.

Both conventional and accelerated light soaking experiments were performed in this study. Accelerated light soaking was confirmed to be a reliable technique capable of quickly evaluating the stability of μc-Si:H solar cells. A wide variety of light soaking behaviors were observed for solar cells with various *i*-layers. Solar cells with truly μc-Si:H *i*-layers exhibit excellent stability under both conventional and accelerated light soaking. However, mixed-phase Si:H solar cells show much worse stability against light exposure. Efficiency increase is usually observed for highly crystalline μc-Si:H solar

cells under accelerated light soaking, which is probably resulting from annealing of some unstable defects inside μc-Si:H *i*-layers.

It has been demonstrated that stable, high performance μc-Si:H solar cells can only be obtained with *i*-layers being μc-Si:H, yet close to the μc-Si:H to mixed-phase Si:H transition edge where an optimum micro-crystallinity range (*Ic/Ia* at around 1.8) was identified. Such optimum μc-Si:H solar cells exhibit moderate open circuit voltages at ~ 0.5 V, high fill factors, high efficiencies, and excellent stability against light-induced degradation. However, such optimum μc-Si:H *i*-layers demand a very narrow optimum processing window, which is probably the most critical challenge in developing low-cost, large-scale μc-Si:H photovoltaic technology.

Those critical issues identified by this study, i.e., critical importance of seeding methods, spatial non-uniformity, and narrow optimum processing window for high quality μc-Si:H, need to be further addressed in the future. To further exploit the advantages associated with μc-Si:H *i*-layers, optical engineering is also needed to enhance the absorption of long wavelength light.

REFERENCES

1. A. Shah, J. Meier, E. Vallat-Sauvain, C. Droz, U. Kroll, N. Wyrsch, J. Guillet, and U. Graf, *Thin Solid Films* **403-404**, 179 (2002).

2. S. K. Deb, *Curr. Opinion in Solid State & Mater. Sci.* **3**, 51 (1998).

3. M. A. Green, *Sol. Energy* **74**, 181 (2003).

4. D. E. Carlson and C. R. Wronski, *Appl. Phys. Lett.* **28**, 671 (1976).

5. A. Goetzberger, C. Hebling, and H. Schock, *Mater. Sci. & Eng.* **R 40**, 1 (2003).

6. D. L. Staebler and C. R. Wronski, *Appl. Phys. Lett.* **31**, 292 (1977).

7. C. R. Wronski, *Conf. Record. 28th IEEE PVSC* (2000), p. 1.

8. M. Wolf, *Proc. 25th Power Sources Symp.* (1972), p. 120.

9. D. M. Chapin, C. S. Fuller, and G. L. Pearson, *J. Appl. Phys.* **25**, 676 (1954).

10. B. G. Streetman and S. Banerjee, *Solid State Electronic Devices, 5th Edition*, Prentice Hall, 2000.

11. J. Szlufcik, S. Sivoththaman, J. F. Nijs, R. P. Mertens, and R. Van Overstaeten, *Proc. IEEE* **85**, 711 (1997).

12. H. F. Sterling, and C. G. Swann, *Solid-State Electron.* **8**, 653 (1965).

13. H. Fritzsche, *Mater. Res. Soc. Symp. Proc.* **609,** A17.1.1 (2000).

14. W. E. Spear, P. G. Le Comber, *Solid State Commun.* **17**, 1193 (1975).

15. M. H. Brodsky, M. A. Frisch, J. F. Ziegler, and W. A. Lanfard, *Appl. Phys. Lett.* **31**, 561 (1977).

16. T. Kanaka, E. Maruyama, T. Shimada, and H. Okamoto, *Amorphous Silicon*, John Wily & Sons, New York, 1999.

17. M. Hirose, *Hydrogenated Amorphous Silicon, Part A: Semiconductors and Semimetals, Vol. 21*, Academic Press, New York, 1984.

18. M. H. Brodsky, M. Cardona, J. J. Cuomo, *Phys. Rev.* **B 16**, 3556 (1977).

19. E. C. Freeman, W. Paul, *Phys. Rev.* **B 18**, 4288 (1978).

20. G. Lucovsky, R. J. Nemanich, J. C. Knights, *Phys. Rev.* **B 19**, 2064 (1979).

21. R. E.I. Schropp and M. Zeman, *Amorphous and Microcrystalline Silicon Solar Cells: Modeling, Materials and Device Technology*, Kluwer Academic Publishers, Boston, 1998.

22. A. A. Langford, M. L. Fleet, B. P. Nelson, W. A. Langford, and N. Maley, *Phys. Rev.* **B 45**, 13367 (1992).

23. K. Takahashi and M. Konagai, *Amorphous Silicon Solar Cells*, John Wiley & Sons, New York, 1986.

24. Y. Tawada, K. Tsuge, M. Kondo, H. Okamoto, and Y. Hamakawa, *J. Appl. Phys.* **53**, 5273 (1982).

25. S. Guha, J. Yang, P. Nath, and M. Hack, *Appl. Phys. Lett.* **49**, 218 (1986).

26. B. Rech, and H. Wagner, *Appl. Phys.* **A 69**, 155 (1999).

27. R. R. Arya, A. Catalano, and R. S. Oswald, *Appl. Phys. Lett.* **49**, 1089 (1986).

28. D. L. Staebler, R. S. Crandall, and R. Williams, *Appl. Phys. Lett.* **39**, 733 (1981).

29. G. Gangly, S. Ray, and A. Barua, *Philos. Mag.* **B 54**, 301 (1986).

30. M. Bennett, K. Rajan, and K. Krittikson, *Conf. Record. 23rd IEEE PVSC* (1993), p. 845.

31. S. Guha, J. Yang, A. banerjee, B. Yan, and K. Lord, *Sol. Energy Mater. & Sol. Cells* **78**, 329 (2003).

32. D. E. Carlson, K. Rajan, R. R. Arya, F. Willing, and L. Yang, *J. Mater. Res.* **13**, 2754 (1998).

33. S. Guha, J. Yang, A. Pawlikiewicz, T. Glatfelter, R. Ross, and S. R. Ovshinsky, *Appl. Phys. Lett.* **54**, 2330 (1989).

34. J. Yang and S. Guha, *Appl. Phys. Lett.* **61**, 2917 (1992).

35. J. Yang, A. Banerjee, and S. Guha, *Appl. Phys. Lett.* **70**, 2975 (1997).

36. A. E. Delahoy, Y-M. Li, J. A. Anna Selvan, L. Chen, T. Varvar, and H. Volltrauer, "*PV in Europe*" *Conf.*, Rome, (2002), p. 444.

37. D. E. Carlson, *Sol. Energy Mater. & Sol. Cells* **78**, 627 (2003).

38. J. Yang, A. Banerjee, S. Guha, *Sol. Energy Mater. & Sol. Cells* **78**, 597 (2003).

39. M. Izu, T. Ellison, *Sol. Energy Mater. & Sol. Cells* **78**, 613 (2003).

40. S. Veprek and V. Marecek, *Solid-State Electron.* **11**, 683 (1968).

41. W. E. Spear, G. Willeke, and P. G. LeComber, *Physica* **117 B & 118 B**, 908 (1983).

42. M. Faraji, S. Gokhale, S. M. Choudhari, and M. G. Takwale, *Appl. Phys. Lett.* **60**, 3289 (1992).

43. J. Meier, R. Fluckiger, H. Keppner, and A. Shah, *Appl. Phys. Lett.* **65**, 860 (1994).

44. J. Meier, S. Dubail, R. Fluckiger, D. Fischer, H. Keppner, and A. Shah, *Proc. 1st WCPEC* (1994), p. 409.

45. S. Dubail, J. A. Anna Selvan, N. Pellaton Vaucher, R. Platz, Ch. Hof, U. Kroll, J. Meier, P. Torres, H. Keppner, N. Wyrsch, M. Goetz, A. Shah, and K. D. Ufert, *Conf. Record. 25th IEEE PVSC* (1996), p. 1053.

46. H. Keppner, J. Meier, P. Torres, D. Fischer, and A. Shah, *Appl. Phys.* **A 69**, 169 (1999).

47. R.E.I. Schropp, *Thin Solid Films* **403-404**, 17 (2002).

48. P.A.T.T. van Veenendaal and R.E.I. Schropp, *Curr. Opinion in Solid State & Mater. Sci.* **6**, 465 (2002).

49. R. S. Crandall, X. Liu, and E. Iwaniczko, *J. Non-Cryst. Solids* **227-230**, 23 (1998).

50. B. Rech, T. Roschek, T. Repmann, J. Muller, R. Schmitz, and W. Appenzeller, *Thin Solid Films* **427**, 157 (2003).

51. L. Guo, M. Kondo, M. Fukawa, K. Saitou, and A. Matsuda, *Jpn. J. Appl. Phys.* **37**, L1116 (1998).

52. Y.-M. Li, J. A. Anna Selvan, L. Li, R. A. Levy, and A. E. Delahoy, *Proc. 3rd WCPEC*, Osaka, Japan, May 2003.

53. B. Yan, G. Yue, J. Yang, A. Banerjee, and S. Guha, *Mater. Res. Soc. Symp. Proc.* **762**, A4.1.1 (2003).

54. M. Kondo, *Sol. Energy Mater. & Sol. Cells* **78**, 543 (2003).

55. O. Vetterl, F. Finger, R. Carius, P. Hapke, L. Houben, O. Kluth, A. Lambertz, A. Muck, B. Rech, and H. Wagner, *Sol. Energy Mater. & Sol. Cells* **62**, 97 (2000).

56. A. V. Shah, J. Meier, E. Vallat-Sauvain, N. Wyrsch, U. Kroll, C. Droz, and U. Graf, *Sol. Energy Mater. & Sol. Cells* **78**, 469 (2003).

57. K. Yamamoto, A. Nakajima, M. Yoshimi, T. Sawada, S. Fukuda, K. Hayashi, T. Suezaki, M. Ichikawa, Y. Koi, M. Goto, H. Takata, and Y. Tawada, *Conf. Record. 29th IEEE PVSC* (2002), p. 1110.

58. J. perrin, O. Leroy, and M.C. Bordage, *Contrib. Plasma Phys.* **36**, 3 (1996).

59. M. Kondo, A. Matsuda, *Curr. Opinion in Solid State & Mater. Sci.* **6**, 445 (2002).

60. R. W. Collins, A. S. Ferlauto, *Curr. Opinion in Solid State & Mater. Sci.* **6**, 425 (2002).

61. A. Matsuda, M. Takai, T. Nishimoto, and M. Kondo, *Sol. Energy Mater. & Sol. Cells* **78**, 3 (2003).

62. T. Takagi, R. Hayashi, G. Ganguly, M. Kondo, and A. Matsuda, *Thin Solid Films* **345**, 75 (1999).

63. M. Takai, T. Nishimoto, T. Takagi, M. Kondo, and A. Matsuda, *J. Non-Cryst. Solids* **266-269**, 90 (2000).

64. M. Takai, T. Nishimoto, M. Kondo, and A. Matsuda, *Appl. Phys. Lett.* **77**, 2828 (2000).

65. M. Kondo, M. Fukawa, L. Guo, and A. Matsuda, *J. Non-Cryst. Solids* **266-269**, 84 (2000).

66. M. Fukawa, S. Suzuki, L. Guo, M. Kondo, and A. Matsuda, *Sol. Energy Mater. & Sol. Cells* **66**, 217 (2001).

67. J. Perrin, Y. Takeda, N. Hirano, Y. Takeuchi, and A. Matsuda, *Surf. Sci.* **210**, 114 (1989).

68. J. L. Guizot, K. Nomoto, and A. Matsuda, *Surf. Sci.* **244**, 22 (1991).

69. J. Robertson, *J. Appl. Phys.* **87**, 2608 (2000).

70. V. Dalal, *Curr. Opinion in Solid State & Mater. Sci.* **6**, 455 (2002).

71. J. Robertson, *J. Non-Cryst. Solids* **226-229**, 79 (2000).

72. H. Shirai, D. Das, J. Hanna, and I. Shimizu, *Appl. Phys. Lett.* **59**, 1096 (1991).

73. K. Nakamura, K. Yoshino, S. Takepka, I. Shimizu, *Jpn. J. Appl. Phys.* **34**, 442 (1995).

74. A. Matsuda, *Thin Solid Films* **337**, 1 (1999).

75. K. Saitoh, M. Kondo, M. Fukawa, T. Nishimiya, A. Matsuda, W. Futako, I. Shimizu, *Appl. Phys. Lett.* **71**, 3403 (1997).

76. O. Vetterl, P. Hapke, L. Houben, F. Finger, R. Carius, H. Wagner, *J. Appl. Phys.* **85**, 2991 (1999).

77. H. Fujiwara, M. Kondo, and A. Matsuda, *Surf. Sci.* **497**, 333 (2002).

78. H. Fujiwara, M. Kondo, and A. Matsuda, *J. Appl. Phys.* **91**, 4181 (2002).

79. H. Fujiwara, M. Kondo, and A. Matsuda, *Jpn. J. Appl. Phys.* **41**, 2821 (2002).

80. P. Danish and B. Pantchev, *Semicond. Sci Technol.* **15**, 971 (2000).

81. P. Danish, B. Pantchev, D. Grambole, and B. Schmidt, *J. Appl. Phys.* **90**, 3065 (2001).

82. D. V. Tsu, B. S. Chao, S. R. Ovshinsky, S. Guha, and J. Yang, *Appl. Phys. Lett.* **71**, 1317 (1997).

83. . Koh, Y. Lee, H. Fujiwara, C. R. Wronski, and R. W. Collins, *Appl. Phys. Lett.* **73**, 1526 (1998).

84. S. Guha, J. Yang, D. L. Williamson, Y. Lubianiker, J. D. Cohen, and A. H. Mahan, *Appl. Phys. Lett.* **74**, 1860 (1999).

85. L. Li, Y.-M. Li, J. A. Anna Selvan, A. E. Delahoy, R. A. Levy, *Mater. Res. Soc. Symp. Proc.* **762**, A5.15.1 (2003).

86. O. Vetterl, R. Carius, L. Houben, C. Scholten, M. Luysberg, A. Lambertz, F. Finger, and H. Wagner, *Mater. Res. Soc. Symp. Proc.* **609**, A15.2.1 (2000).

87. R. W. Collins, A. S. Ferlauto, G. M. Ferreira, C. Chen, J. Koh, R. J. Koval, Y. Lee, J. M. Pearce, and C. R. Wronski, *Sol. Energy Mater. & Sol. Cells* **78**, 143 (2003).

88. R. W. Collins, A. S. Ferlauto, G. M. Ferreira, J. Koh, C. Chen, R. J. Koval, J. M. Pearce, C. R. Wronski, M. M. Al-Jassim, and K. M. Jones, *Mater. Res. Soc. Symp. Proc.* **762**, A10.1.1 (2003).

89. A. S. Ferlauto, R. J. Koval, C. R. Wronski, and R. W. Collins, *Appl. Phys. Lett.* **80**, 2666 (2002).

90. J. Koh, A. S. Ferlauto, P. I. Rovira, C. R. Wronski, and R. W. Collins, *Appl. Phys. Lett.* **75**, 2286 (1999).

91. E. Vallat-Sauvain, U. Kroll, J. Meier, A. Shah, and J. Pohl, *J. Appl. Phys.* **87**, 3137 (2000).

92. C. Ross, J. Herion, and H. Wagner, *J. Non-Cryst. Solids* **266-269**, 69 (2000).

93. K. Mori, T. Yasuda, M. Nishizawa, S. Yamasaki, and K. Tanaka, *Jpn. J. Appl. Phys.* **39**, 6647 (2000).

94. Y. Nasuno, M. Kondo, and A. Matsuda, *Jpn. J. Appl. Phys.* **40**, L303 (2001).

95. J. Bailat, E. Vallat-Sauvain, L. Feitknecht, C. Droz, and A. Shah, *J. Non-Cryst. Solids* **299-302**, 1219 (2002).

96. E. Edelman, A. Chack, R. Weil, R. Beserman, Yu. L. Khait, P. Werner, B. Bech, T. Roschek, R. Carius, H. Wagner, and W. Beyer, *Sol. Energy Mater. & Sol. Cells* **77**, 125 (2003).

97. R. Tsu, J. Gonzalez-Hernandez, S. S. Chao, S. C. Lee, and K. Tanaka, *Appl. Phys. Lett.* **40**, 534 (1982).

98. E. Bustarret, M. A. Hachinia, and M. Brunel, *Appl. Phys. Lett.* **52**, 1675 (1988).

99. S. Sumiya, Y. Mizutani, R. Yoshida, M. Hori, T. Goto, M. Ito, T. Tsukada, and S. Samukawa, *J. Appl. Phys.* **88**, 576 (2000).

100. L. Houben, M. Luysberg, P. Hapke, R. Carius, F. finger, and H. wagner, *Philos. Mag.* **A 77**, 1447 (1998).

101. S. Veprek, F.-A. Sarott, and Z. Iqbal, *Phys. Rev.* **B 36**, 3344 (1987).

102. Ch. Ossadnik, S. Veprek, and I. Gregora, *Thin Solid Films* **337**, 148 (1999).

103. B. D. Cullity, *Elements of X-Ray Diffraction*, Addisn-Wesley, 1978.

104. A. Matsuda, K. Kumagai, and K. Tanaka, *Jpn. J. Appl. Phys.* **22**, L34 (1982).

105. S. Veprek, Z. Iqbal, O. Kuhne, P. Capezzuto, F. A. Sarott, and J. K. Gimzewski, *J. Phys.* **C 16**, 6241 (1983).

106. K. Nakahata, A. Miida, T. Kamiya, Y. Maeda, C. M. Fortmann, and I. Shimizu, *Jpn. J. Appl. Phys.* **37**, L1026 (1998).

107. M. Luysberg, C. Scholten, L. Houben, R. Carius, F. Finger, and O. Vetterl, *Mat. Res. Soc. Symp. Proc.* Vol. **664**, A 15.2.1 (2001).

108. A. E. Delahoy, *Sol. Cells* **21**, 153 (1987).

109. L. Yang, L. Chen, and A. Catalano, *Appl. Phys. Lett.* **59**, 840 (1991).

110. D. E. Carlson and K. Rajan, *Appl. Phys. Lett.* **70**, 2168 (1997).

111. P. Stradins, *Sol. Energy Mater. & Sol. Cells* **78**, 349 (2003).

112. U. Kroll, J. Meier, A. Shah, S. Mikhailov, and J. Weber, *J. Appl. Phys.* **80**, 4971 (1996).